

<sup>1</sup> STANDARD MODEL IS BEST MODEL (WORKING TITLE)

<sup>2</sup> William Kennedy DiClemente

<sup>3</sup> A DISSERTATION  
<sup>4</sup> in  
<sup>5</sup> Physics and Astronomy

<sup>6</sup> Presented to the Faculties of The University of Pennsylvania  
<sup>7</sup> in Partial Fulfillment of the Requirements for the Degree of Doctor of Philosophy  
<sup>8</sup> 2019 Last compiled: January 23, 2019

---

<sup>9</sup>  
<sup>10</sup> I. Joseph Kroll, Professor, Physics  
<sup>11</sup> Supervisor of Dissertation

---

<sup>12</sup>  
<sup>13</sup> Joshua Klein, Professor, Physics  
<sup>14</sup> Graduate Group Chairperson

<sup>15</sup> Dissertation Committee  
<sup>16</sup> (Committee Prof. 1), Professor, Physics  
<sup>17</sup> (Committee Prof. 2), Associate Professor, Physics  
<sup>18</sup> (Committee Prof. 3), Professor, Physics  
<sup>19</sup> (Committee Prof. 4), Professor, Physics  
<sup>20</sup> I. Joseph Kroll, Professor, Physics

21

S T A N D A R D   M O D E L   I S   B E S T   M O D E L   ( W O R K I N G   T I T L E )

22  
23  
24

C O P Y R I G H T  
2019  
William Kennedy DiClemente

25

All rights reserved.

---

## Acknowledgements

---

27 I'd like to thanks the Ghosts of Penn Students Past for providing me with such an amazing thesis  
28 template.

29

## ABSTRACT

30

STANDARD MODEL IS BEST MODEL (WORKING TITLE)

31

William Kennedy DiClemente

32

J. Kroll

33

This is the abstract text.

---

# Contents

---

35	<b>Acknowledgements</b>	iii
36	<b>Abstract</b>	iv
37	<b>Contents</b>	v
38	<b>List of Tables</b>	ix
39	<b>List of Figures</b>	xii
40	<b>Preface</b>	xvi
41	<b>1 Introduction</b>	1
42	<b>2 Theoretical Framework</b>	2
43	2.1 Introduction to the Standard Model . . . . .	2
44	2.2 Electroweak Mixing and the Higgs Field . . . . .	2
45	<b>3 LHC and the ATLAS Detector</b>	3
46	3.1 The Large Hadron Collider . . . . .	3
47	3.2 The ATLAS Detector . . . . .	3
48	3.2.1 The Inner Detector . . . . .	3
49	3.2.1.1 Pixel Detector . . . . .	3
50	3.2.1.2 Semiconductor Tracker . . . . .	3
51	3.2.1.3 Transition Radiation Tracker . . . . .	3
52	3.2.2 The Calorimeters . . . . .	4

53	3.2.2.1	Liquid Argon Calorimeters . . . . .	4
54	3.2.2.2	Tile Calorimeters . . . . .	4
55	3.2.3	The Muon Spectrometer . . . . .	4
56	3.2.4	Particle reconstruction . . . . .	5
57	3.2.4.1	Track reconstruction . . . . .	5
58	3.2.4.2	Muon reconstruction . . . . .	5
59	3.2.4.3	Electron reconstruction . . . . .	5
60	3.2.4.4	Jet reconstruction . . . . .	5
61	<b>4</b>	<b>Alignment of the ATLAS Inner Detector</b>	<b>6</b>
62	4.1	The Alignment Method . . . . .	7
63	4.1.1	Alignment levels . . . . .	10
64	4.2	Early 2015 alignment of the ATLAS detector . . . . .	12
65	4.2.1	Alignment of the IBL . . . . .	12
66	4.3	Momentum Bias Corrections . . . . .	12
67	4.4	Alignment Monitoring . . . . .	12
68	<b>5</b>	<b>Measurement of same-sign <math>WW</math> production at <math>\sqrt{s} = 13</math> TeV with ATLAS</b>	<b>13</b>
69	5.0.1	Theoretical overview of vector boson scattering . . . . .	13
70	5.0.2	Same-sign $W^\pm W^\pm$ scattering . . . . .	15
71	5.0.3	Overview of backgrounds . . . . .	17
72	5.1	Data and Monte Carlo samples . . . . .	19
73	5.1.1	Monte Carlo samples . . . . .	19
74	5.2	Object and event selection . . . . .	20
75	5.2.1	Object selection . . . . .	20
76	5.2.1.1	Muon candidate selection . . . . .	21
77	5.2.1.2	Electron candidate selection . . . . .	23
78	5.2.1.3	Jet candidate selection . . . . .	23
79	5.2.1.4	Treatment of overlapping objects . . . . .	23
80	5.2.2	Signal event selection . . . . .	25
81	5.3	Background estimations . . . . .	27
82	5.3.1	Estimation of the $WZ$ background . . . . .	27
83	5.3.2	Estimation of the $V\gamma$ background . . . . .	28

84	5.3.3	Estimation of backgrounds from charge misidentification . . . . .	30
85	5.3.3.1	Validation of the charge misidentification estimate . . . . .	33
86	5.3.4	Estimation of non-prompt backgrounds with the fake factor method . . . . .	34
87	5.3.4.1	Overview of the default fake factor method . . . . .	34
88	5.3.4.2	The fake factor with $p_T^{\text{cone}}$ . . . . .	35
89	5.3.4.3	Application of the fake factor . . . . .	37
90	5.3.4.4	Systematic uncertainties . . . . .	42
91	5.3.4.5	Results of the fake factor . . . . .	42
92	5.3.4.6	Validation of the fake factor . . . . .	44
93	5.3.5	Reduction of $WZ$ background using custom overlap removal . . . . .	47
94	5.4	Cross section measurement . . . . .	50
95	5.4.1	Maximum likelihood fit . . . . .	51
96	5.4.2	Definition of the fiducial volume . . . . .	53
97	5.4.3	Cross section extraction . . . . .	54
98	5.5	Summary of uncertainties . . . . .	55
99	5.5.1	Experimental uncertainties . . . . .	56
100	5.5.2	Theoretical uncertainties . . . . .	57
101	5.5.2.1	Uncertainties from EWK-QCD interference . . . . .	57
102	5.6	Results . . . . .	58
103	<b>6</b>	<b>Prospects for same-sign <math>WW</math> at the High Luminosity LHC</b>	<b>63</b>
104	6.0.1	Analysis Overview . . . . .	64
105	6.1	Theoretical motivation . . . . .	64
106	6.1.1	Experimental sensitivity to longitudinal polarization . . . . .	65
107	6.2	Monte Carlo samples . . . . .	65
108	6.3	Background estimations . . . . .	67
109	6.3.1	Truth-based isolation . . . . .	68
110	6.4	Object and event selection . . . . .	69
111	6.4.1	Object selection . . . . .	69
112	6.4.2	Event selection . . . . .	69
113	6.5	Selection optimization . . . . .	70
114	6.5.1	Random grid search algorithm . . . . .	70
115	6.5.2	Inputs to the optimization . . . . .	72

116	6.5.3 Results of the optimization . . . . .	73
117	6.6 Results . . . . .	74
118	6.6.1 Event yields . . . . .	74
119	6.6.2 Uncertainties . . . . .	80
120	6.6.3 Cross section measurement . . . . .	80
121	6.6.4 Longitudinal scattering significance . . . . .	81
122	<b>7 Conclusion</b>	85
123	<b>A Additional material on truth isolation</b>	86
124	<b>B Additional material on <math>W^\pm W^\pm jj</math> measurement at <math>\sqrt{s} = 13\text{TeV}</math></b>	87
125	B.1 Impact of experimental uncertainty on MC background estimations . . . . .	87
126	<b>Bibliography</b>	89

---

## List of Tables

---

128	4.1	The four alignment levels for each of the detector subsystems. The total number of alignable structures and degrees of freedom (DoF) to be aligned are given for each level.	11
130	5.1	Predicted cross sections for EQK and QCD production of diboson processes relevant to VBS at $\sqrt{s} = 8\text{TeV}$ using the <b>SHERPA</b> MC generator. Loose generator level cuts are applied on lepton $p_T > 5\text{ GeV}$ , dilepton invariant mass $m_{ll} > 4\text{ GeV}$ , and at least two jets with $m_{jj} > 10\text{ GeV}$ .	16
134	5.2	Summary of MC samples used in the analysis.	21
135	5.3	Muon selection criteria. All muons are required to pass the preselection (top), and then either the signal (middle) or loose (bottom) criteria is applied to the preselected electrons.	22
137	5.4	Electron selection criteria. All electrons are required to pass the preselection (top), and then either the signal (middle) or loose (bottom) criteria is applied to the preselected electrons.	24
140	5.5	Jet selection criteria. All jets are required to pass the above selection in order to be used in the analysis.	24
142	5.6	Summary of the overlap removal procedure used in the analysis. If the criteria in the “check” column is met, in the “result” column, the object on the left of the arrow is removed in favor of the object on the right.	25
145	5.7	Summary of trigger requirements for electrons and muons for $\sqrt{s} = 13\text{TeV}$ data collected in 2015 and 2016. At least one of the triggers must be satisfied.	26
147	5.8	The signal event selection.	27
148	5.9	Event yields in the $WZ$ control region before normalization. All lepton flavor channels are combined.	28
150	5.10	Selection criteria for the $V\gamma$ control region.	29
151	5.11	Event yields in the $V\gamma$ control region. The $V\gamma$ scale factor of 1.77 is calculated by scaling up the $Z\gamma$ and $Z+\text{jets}$ backgrounds to account for the difference between the data and predicted total background.	30
154	5.12	Selection criteria for the same-sign inclusive validation region.	33
155	5.13	Event selection for the dijet region used for calculating the fake factor. The selected lepton can pass either the nominal (signal) or loose selections. In the case of the nominal leptons, the $p_T > 27\text{ GeV}$ requirement is replaced with $p_T > 15\text{ GeV}$ .	39
158	5.14	Values of the fake factor in each $p_T$ bin and for each individual systematic source.	43

---

159	5.15	Estimated yields for the fake lepton background. The estimated yield is shown in the first column together with the statistical uncertainty followed by the systematic uncertainties from variations of the the fake factors within their statistical (stat.) and systematic (syst.) uncertainties. The labels $f_e$ and $f_\mu$ indicate the fake factors for electrons and muons, respectively. . . . .	43
160			
161			
162			
163			
164	5.16	Selection criteria for the same-sign top fakes validation region. . . . .	44
165	5.17	Custom OR definition. Leptons must pass this selection in order to be counted for the trilepton veto. . . . .	50
166			
167	5.18	Definition of the fiducial volume. . . . .	53
168	5.19	Impact of various systematic effects on the fiducial cross section measurement. The impact of a given source of uncertainty is computed by performing the fit with the corresponding nuisance parameter varied up or down by one standard deviation from its nominal value. . . . .	55
169			
170			
171			
172	5.20	List of sources of experimental uncertainties on the reconstruction of physics objects. . . . .	56
173	5.21	Impact of experimental uncertainties for the $W^\pm W^\pm jj$ EWK processes in all channels. . . . .	57
174	5.22	Impact of experimental uncertainties for the $WZ$ process in all channels. . . . .	57
175	5.23	The set of generator level cuts used for generating the interference samples with <code>MadGraph</code> . . . . .	58
176	5.24	Cross sections for each different $W^\pm W^\pm jj$ production mode (inclusive, EWK only, QCD only, and interference only) generated using <code>MadGraph</code> . The cross sections are calculated using a minimal set of generator level cuts from events where the $W$ decays to a muon. . . . .	58
177			
178			
179	5.25	Table of the data and prediction event yields in the signal region before the fit. Numbers are shown for the six lepton flavor and charge channels and for all channels combined. Here the $WZ$ background yields are normalized to the data in the $WZ$ control region. The background estimations from the fake factor are included in the “Non-prompt” category, and backgrounds from $V\gamma$ production and electron charge misidentification are combined in the “ $e/\gamma$ conversions” category. Finally, $ZZ$ , $VVV$ , and $t\bar{t}V$ backgrounds are combined in the “Other prompt” category. . . . .	59
180			
181			
182			
183			
184			
185			
186	5.26	Table of the data and prediction event yields in the signal region after the fit. Numbers are shown for the six lepton flavor and charge channels and for all channels combined. The background estimations from the fake factor are included in the “Non-prompt” category, and backgrounds from $V\gamma$ production and electron charge misidentification are combined in the “ $e/\gamma$ conversions” category. Finally, $ZZ$ , $VVV$ , and $t\bar{t}V$ backgrounds are combined in the “Other prompt” category. . . . .	60
187			
188			
189			
190			
191			
192	6.1	Summary of MC samples used in the analysis. . . . .	67
193	6.2	Truth-based isolation requirements for electrons and muons. . . . .	68
194	6.3	Summary of the signal event selection. . . . .	70
195	6.4	Updates to the $W^\pm W^\pm jj$ event selection criteria after optimization. Cuts not listed remain unchanged from the default selection in Table 6.3. . . . .	74
196			
197	6.5	Signal and background event yields using the default event selection for an integrated luminosity of $\mathcal{L} = 3000 \text{ fb}^{-1}$ . Events containing a fake or charge-flipped electron are removed from their respective sources and combined into a single entry each. . . . .	78
198			
199			
200	6.6	Signal and background event yields using the optimized event selection for an integrated luminosity of $\mathcal{L} = 3000 \text{ fb}^{-1}$ . Events containing a fake or charge-flipped electron are removed from their respective sources and combined into a single entry each. . . . .	78
201			
202			
203	6.7	Summary of estimated experimental and rate uncertainties. . . . .	80
204	A.1	Event yields prior to applying any form of truth-based isolation criteria. . . . .	86
205	A.2	Event yields after applying a test version of the truth-based isolation. . . . .	86

206	B.1	Experimental systematics uncertainties for the $W^\pm W^\pm jj$ QCD processes in all channels.	87
207	B.2	Experimental systematics uncertainties for triboson process in all channels. . . . .	87
208	B.3	Experimental systematics uncertainties for $t\bar{t}V$ processes in all channels. . . . .	88
209	B.4	Experimental systematics uncertainties for the $W\gamma$ process in all channels. . . . .	88
210	B.5	Experimental systematics uncertainties for the $Z\gamma$ process in all channels. . . . .	88
211	B.6	Experimental systematics uncertainties for the $ZZ$ process in all channels. . . . .	88

---

## List of Figures

---

213	3.1	General cut-away view of the ATLAS detector.	4
214	4.1	Graphical representation of the effect of a misaligned detector element. The reconstructed particle track (dashed arrow) differs from the actual trajectory of the particle (solid arrow) due to the shift in one of the detector elements. The cyan lines represent the track-to-hit residuals.	7
215	4.2	Graphical representation of the ID alignment chain.	10
216			
217			
218	5.1	Cross sections in nanobarns for five different scattering processes of longitudinally polarized vector bosons as a function of center of mass energy $\sqrt{s}$ . Without a SM Higgs boson (left), the cross sections grow unbounded with $\sqrt{s}$ ; however with a 120 GeV Higgs boson (right), the cross sections no longer diverge.	14
219	5.2	Tree-level Feynman diagrams for VBS EWK $VVjj$ production including triple gauge couplings involving $W$ and/or $Z$ bosons (top left and top middle), quartic gauge coupling (top right), or the exchange of a Higgs boson ( $s$ -channel bottom left and $t$ -channel bottom right). The labels are quarks ( $q$ ), fermions ( $f$ ), and gauge bosons ( $V = W, Z$ ).	15
220	5.3	Tree-level Feynman diagrams for non-VBS EWK $VVjj$ production. The labels are quarks ( $q$ ), fermions ( $f$ ), and gauge bosons ( $V = W, Z$ ).	15
221	5.4	Tree-level Feynman diagrams for QCD $VVjj$ production. The labels are quarks ( $q$ ), fermions ( $f$ ), and gauge bosons ( $V = W, Z$ ).	16
222	5.5	Feynman diagrams for VBS EWK production of $W^\pm W^\pm jj$ events. The leftmost diagram contains a quartic gauge coupling vertex, and the rightmost diagram contains an exchange of a Higgs boson. <b>TODO: Make diagrams consistent with others</b>	17
223	5.6	$W^\pm W^\pm jj$ VBS event topology containing two leptons (1 and 2) with the same electric charge, two neutrinos, and two forward tagging jets (3 and 4) with large rapidity separation $\Delta y$ .	17
224	5.7	Generator level comparisons at $\sqrt{s} = 8\text{TeV}$ of dijet invariant mass ( $m_{jj}$ , left) and dijet rapidity ( $\Delta y_{jj}$ , right) in EWK (red) and QCD (blue) $W^\pm W^\pm jj$ events. Both data sets have been normalized to the same area.	18
225			
226			
227			
228			
229			
230			
231			
232			
233			
234			
235			
236			
237			
238			
239			

240	5.8 ATLAS event display of a $pp \rightarrow W^+W^+ \rightarrow \mu^+\nu_\mu\mu^+\nu_\mu jj$ event. The muons are represented by the red lines travelling from the ID through the MS, and the forward jets are represented by the blue cones with yellow energy deposits in the calorimeters. The direction of the $E_T^{\text{miss}}$ in the transverse plane is indicated by the gray dashed line in the inset image. Event display taken from [1]. . . . .	18
245	5.9 Leading lepton $p_T$ (left) and $\eta$ (right) distributions in the $WZ$ control region before normalization. All lepton channels are combined. . . . .	29
247	5.10 Trilepton invariant mass $m_{lll}$ distribution in the $WZ$ control region before normalization. All lepton channels are combined. . . . .	29
249	5.11 Charge misidentification rates for electrons as a function of $ \eta $ and $p_T$ . Rates are calculated from $Z \rightarrow e^+e^-$ MC after applying scale factors to approximate the charge mis-ID rates in data. . . . .	31
252	5.12 Dilepton invariant mass distribution $m_{ll}$ for the $ee$ channel in the same-sign inclusive VR. . . . .	33
253	5.13 $p_T$ distributions for the leading (left) and subleading (right) electron for the $ee$ channel in the same-sign inclusive VR. In these plots, the cut requiring $m_{ee}$ to fall within the $Z$ mass window has been inverted in order to test the modelling away from the $Z$ peak. . . . .	34
256	5.14 $\Delta p_T$ distributions for nominal (blue) and loose (red) muons in simulated $t\bar{t}$ events. Each muon has been matched to a truth-level jet. Both distributions are normalized to unit area. . . . .	36
259	5.15 $\Delta p_T$ distributions for muons (top) and electrons (bottom) in simulated $t\bar{t}$ events. Each lepton has been matched to a truth-level jet, and that truth jet has had its $p_T$ corrected to include all truth muons within a cone of $\Delta R < 0.4$ . The nominal leptons are in black. $\Delta p_T$ is calculated for the loose leptons using $p_T$ (red) and $p_T + p_T^{\text{cone}}$ (blue). . . . .	38
263	5.16 Distributions of $p_T^{\text{cone}}/p_T$ for nominal (black) and loose (red) muons in simulated $t\bar{t}$ events. . . . .	39
264	5.17 The measured fake factor as a function of muon $p_T + p_T^{\text{cone}}$ . The error bars represent the statistical uncertainty only. . . . .	40
266	5.18 The measured fake factor as a function of electron $p_T + p_T^{\text{cone}}$ in the central ( $ \eta  < 1.37$ , blue) and forward ( $ \eta  > 1.37$ , red) regions of the detector. The error bars represent the statistical uncertainty only. . . . .	40
269	5.19 Graphical representation of the fake factor application using $p_T + p_T^{\text{cone}}$ . The value of $p_T + p_T^{\text{cone}}$ for the loose lepton is used to “look up” the fake factor weight which is then applied to the event. The loose lepton’s $p_T$ becomes $p_T + p_T^{\text{cone}}$ for the purpose of the fake background estimation. . . . .	41
273	5.20 Systematic variations in the fake factor as a function of muon $p_T + p_T^{\text{cone}}$ . The individual fake factors obtained for each systematic variation are displayed with their statistical uncertainties. . . . .	44
276	5.21 Systematic variations in the fake factor as a function of electron $p_T + p_T^{\text{cone}}$ in the central ( $ \eta  < 1.37$ , top) and forward ( $ \eta  > 1.37$ , bottom) regions of the detector. The individual fake factors obtained for each systematic variation are displayed with their statistical uncertainties. . . . .	45
280	5.22 Distributions of the subleading lepton $p_T$ in the same-sign top fakes VR for $\mu^\pm\mu^\pm$ events (top right), $e^\pm e^\pm$ events (top left), $\mu^\pm e^\pm$ events (bottom left), and all events combined (bottom right). All errors are statistical only. . . . .	46
283	5.23 Pseudorapidity ( $\eta$ ) distributions of truth muons (top) and electrons (bottom) for Sherpa $W^\pm W^\pm jj$ and $WZ$ MC samples. The blue vertical lines represent the allowed $\eta$ range for each lepton flavor. The numbers correspond to the number of raw MC events that fall within and outside of the allowed $\eta$ range for each MC sample. . . . .	48

287	5.24 Distributions of $p_{T,\text{ratio}}(\mu, j)$ for EWK and QCD $W^\pm W^\pm jj$ signal (black) and $WZ$ background (teal) for truth-matched third muons in events that pass the trilepton veto. Both distributions are normalized to unit area. The associated efficiency curves are on the right where efficiency is defined as the percentage of total events that would pass a cut on $p_{T,\text{ratio}}(\mu, j)$ at a given value on the $x$ -axis. . . . .	48
292	5.25 Distributions of $\Delta R(\mu, j)$ for EWK and QCD $W^\pm W^\pm jj$ signal (black) and $WZ$ background (teal) for truth-matched third muons in events that pass the trilepton veto. Both distributions are normalized to unit area. The associated efficiency curves are on the right where efficiency is defined as the percentage of total events that would pass a cut on $\Delta R(\mu, j)$ at a given value on the $x$ -axis. . . . .	49
297	5.26 Distributions of $p_{T,\text{ratio}}(e, j)$ for EWK and QCD $W^\pm W^\pm jj$ signal (black) and $WZ$ background (teal) for truth-matched third electrons in events that pass the trilepton veto. Both distributions are normalized to unit area. The associated efficiency curves are on the right where efficiency is defined as the percentage of total events that would pass a cut on $p_{T,\text{ratio}}(e, j)$ at a given value on the $x$ -axis. . . . .	49
302	5.27 Two-dimensional plots of $p_{T,\text{ratio}}(\mu, j)$ vs $\Delta R(\mu, j)$ for truth-matched third muons in events that pass the trilepton veto for EWK and QCD $W^\pm W^\pm jj$ signal (left) and $WZ$ background (right). The blue overlay indicates the area in which the third leptons will pass the custom OR and result in the event failing the trilepton veto. . . . .	50
306	5.28 Visual representation of the different kinematic regions relevant to the cross section measurement. The acceptance factor $\mathcal{A}$ converts from the truth level total phase space to the truth level fiducial region, and the efficiency correction $\mathcal{C}$ translates the fiducial region into the reconstruction level signal region. . . . .	54
310	5.29 The dijet invariant mass $m_{jj}$ distributions for data and predicted signal and background in the signal region after the fit. The shaded band represents the statistical and systematic uncertainties added in quadrature. Note that the bins have been scaled such that they represent the number of events per 100 GeV in $m_{jj}$ . The background estimations from the fake factor are included in the “Non-prompt” category, and backgrounds from $V\gamma$ production and electron charge misidentification are combined in the “ $e/\gamma$ conversions” category. Finally, $ZZ$ , $VVV$ , and $t\bar{t}V$ backgrounds are combined in the “Other prompt” category. . . . .	60
318	5.30 The event yields for data and predicted signal and background in the $WZ$ and low- $m_{jj}$ control regions after the fit. The shaded band represents the statistical and systematic uncertainties added in quadrature. The background estimations from the fake factor are included in the “Non-prompt” category, and backgrounds from $V\gamma$ production and electron charge misidentification are combined in the “ $e/\gamma$ conversions” category. Finally, $ZZ$ , $VVV$ , and $t\bar{t}V$ backgrounds are combined in the “Other prompt” category. . . . .	61
324	5.31 Comparison of the measured $W^\pm W^\pm jj$ EWK fiducial cross section with theoretical calculations from <b>SHERPA v2.2.2</b> and <b>POWHEG-BOX v2</b> . The light orange band represents the total experimental uncertainty on the measured value, and the dark orange hashed band is the statistical uncertainty. For the simulations, the light blue band represents the total theoretical uncertainty, and the dark blue hashed band are the scale uncertainties. The theory predictions do not include the interference between the EWK and QCD production. . . . .	62
331	6.1 Comparison of the leading (top) and subleading (bottom) lepton $p_T$ distributions for purely longitudinal (LL, black) and mixed polarization (LT+TT, cyan) $W^\pm W^\pm jj$ events. . . . .	66
333	6.2 Comparison of the azimuthal dijet separation ( $ \Delta\phi_{jj} $ ) for purely longitudinal (LL, black) and mixed polarization (LT+TT, cyan) $W^\pm W^\pm jj$ events. . . . .	67

335	6.3	A visual representation of a rectangular grid search algorithm. The signal events are the blue triangles, and the red circles are the background events. <b>TODO: replace with own figure</b>	71
338	6.4	A visual representation of a random grid search algorithm. The signal events are the blue triangles, and the red circles are the background events. <b>TODO: replace with own figure</b>	72
341	6.5	Leading lepton $p_T$ distribution. The default and optimized cuts are represented by the red and green dashed lines, respectively. The $W^\pm W^\pm jj$ EWK signal (black points) is normalized to the same area as the sum of the backgrounds (colored histogram). <b>TODO: Move to appendix or omit</b>	75
345	6.6	Dilepton invariant mass distribution. The default and optimized cuts are represented by the red and green dashed lines, respectively. The $W^\pm W^\pm jj$ EWK signal (black points) is normalized to the same area as the sum of the backgrounds (colored histogram). <b>TODO: Move to appendix or omit</b>	75
349	6.7	Leading (top) and subleading (bottom) jet $p_T$ distributions. The default and optimized cuts are represented by the red and green dashed lines, respectively. The $W^\pm W^\pm jj$ EWK signal (black points) is normalized to the same area as the sum of the backgrounds (colored histogram).	76
353	6.8	Dijet invariant mass distribution. The default and optimized cuts are represented by the red and green dashed lines, respectively. The $W^\pm W^\pm jj$ EWK signal (black points) is normalized to the same area as the sum of the backgrounds (colored histogram). <b>TODO: Move to appendix or omit</b>	77
357	6.9	Lepton-jet centrality distribution. The default and optimized cuts are represented by the red and green dashed lines, respectively. The $W^\pm W^\pm jj$ EWK signal (black points) is normalized to the same area as the sum of the backgrounds (colored histogram).	77
360	6.10	$p_T$ distributions for the leading jet using the default (left) and optimized (right) event selections for all channels combined.	79
362	6.11	$p_T$ distributions for the subleading jet using the default (left) and optimized (right) event selections for all channels combined.	79
364	6.12	$p_T$ distributions for lepton-jet centrality $\zeta$ using the default (left) and optimized (right) event selections for all channels combined.	79
366	6.13	Projections of the statistical (black), theoretical (blue), systematic (yellow), and total (red) uncertainties on the measured cross section as a function of integrated luminosity using the optimized event selection.	81
369	6.14	Dijet azimuthal separation ( $ \Delta\phi_{jj} $ ) for the low $m_{jj}$ region ( $520 < m_{jj} < 1100$ GeV, top) and the high $m_{jj}$ region ( $m_{jj} > 1100$ GeV, bottom). The purely longitudinal (LL, gray) is plotted separately from the mixed and transverse (LT+TT, cyan) polarizations.	83
372	6.15	Projections of the expected longitudinal scattering significance as a function of integrated luminosity when considering all sources of uncertainties (black) or only statistical uncertainties (red).	84

---

## Preface

---

<sup>376</sup> This is the preface. It's optional, but it's nice to give some context for the reader and stuff.

Will K. DiClemente

Philadelphia, February 2019

378

## CHAPTER 1

---

379

### Introduction

---

380 The Standard Model (SM)<sup>1</sup> has been remarkably successful...

---

<sup>1</sup>Here's a footnote.

381

## CHAPTER 2

---

382

# Theoretical Framework

---

383 (Some example introductory text for this chapter)...

## 384 2.1 Introduction to the Standard Model

385 Modern particle physics is generally interpreted in terms of the Standard Model (SM). This is a  
386 quantum field theory which encapsulates our understanding of the electromagnetic, weak, and strong  
387 interactions...

## 388 2.2 Electroweak Mixing and the Higgs Field

389 When the theory of the electroweak interaction was first developed [2, 3], the  $W$  and  $Z$  bosons were  
390 predicted to be massless (a typical mass term in the Lagrangian would violate the  $SU(2)$  symmetry).  
391 However, these were experimentally observed to have masses...

392

## CHAPTER 3

393

# LHC and the ATLAS Detector

394 **3.1 The Large Hadron Collider**

395 The Large Hadron Collider (LHC) [4] is...

396 **3.2 The ATLAS Detector**

397 ATLAS is a general-purpose particle detector...

398 **3.2.1 The Inner Detector**

399 The Inner Detector serves the primary purpose of measuring the trajectories of charged particles...

400 **3.2.1.1 Pixel Detector**

401 The Pixel detector consists of four cylindrical barrel layers and three disk-shaped endcap layers...

402 **3.2.1.2 Semiconductor Tracker**

403 The Semiconductor Tracker uses the same basic technology as the Pixels, but the fundamental unit  
404 of silicon is a larger “strip”...

405 **3.2.1.3 Transition Radiation Tracker**

406 The Transition Radiation Tracker is the outermost component of the ID...

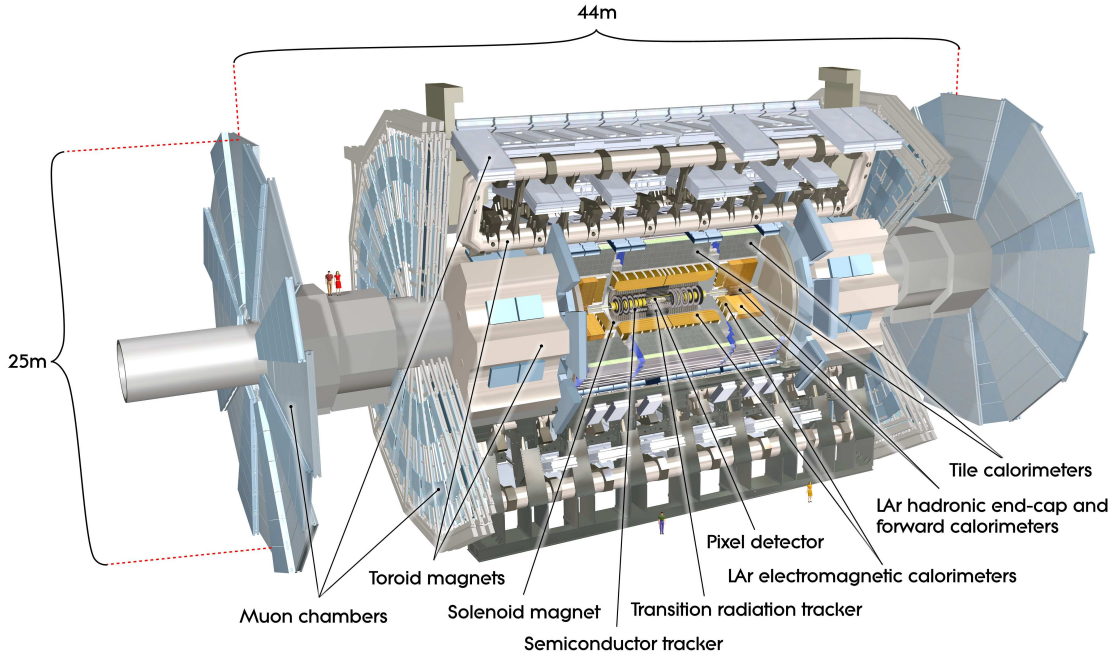


Figure 3.1: General cut-away view of the ATLAS detector [5].

### 407 3.2.2 The Calorimeters

408 ATLAS includes two types of calorimeter system for measuring electromagnetic and hadronic show-  
 409 ers. These are the Liquid Argon (LAr) calorimeters and the Tile calorimeters. Together, these cover  
 410 the region with  $|\eta| < 4.9\dots$

#### 411 3.2.2.1 Liquid Argon Calorimeters

412 The Liquid Argon system consists of...

#### 413 3.2.2.2 Tile Calorimeters

414 The Tile calorimeter provides coverage for hadronic showers...

### 415 3.2.3 The Muon Spectrometer

416 Muon spectrometer stuff.

<sup>417</sup> **3.2.4 Particle reconstruction**

<sup>418</sup> Particle reconstruction algorithms

<sup>419</sup> **3.2.4.1 Track reconstruction**

<sup>420</sup> **3.2.4.2 Muon reconstruction**

<sup>421</sup> **3.2.4.3 Electron reconstruction**

<sup>422</sup> **3.2.4.4 Jet reconstruction**

## CHAPTER 4

---

# 424 Alignment of the ATLAS Inner Detector

---

425 When a charged particle passes through the ATLAS ID, it leaves hits in the sensors along its path.  
426 In order to accurately measure the track of the particle, it is necessary to know where these hits  
427 occurred as precisely as possible, which in turn requires knowledge of the physical location of the  
428 element that registered the hit. If one of these elements is *misaligned*, or displaced relative to  
429 its position in the known detector geometry, the assumed location of the corresponding hit will  
430 not match its actual location, resulting in an incorrect track fit. These misalignments can occur for  
431 any number of reasons, including but not limited to elements shifting during maintenance periods or  
432 cycles in ATLAS's magnetic field, or small movements during normal detector operations. The effect  
433 of a misaligned detector element on the track reconstruction and the resulting track-hit residuals is  
434 shown in Figure 4.1. **TODO: there has to be a better way to introduce this figure – i haven't talked**  
435 **about residuals yet**

436 In order to correct the misalignments, the ID alignment procedure is applied to accurately  
437 determine the physical position and orientation of each detector element. The baseline accuracy of  
438 the alignment is required to be such that the track parameter resolutions are not degraded by more  
439 than 20% with respect to those derived from a perfect detector geometry<sup>2</sup>. This corresponds to a  
440 precision of better than  $10\mu\text{m}$  in the positioning of the elements of the silicon detectors [6]. This  
441 chapter outlines the ID alignment procedure, the alignment of the detector during the 2015 data  
442 taking period, and the steps taken to monitor the performance of the alignment.

---

<sup>2</sup>The so-called *perfect geometry* refers to the description of the ATLAS detector in which every sensor precisely matches its design specifications. The perfect geometry contains no misalignments, and the position of each sensor is known exactly.

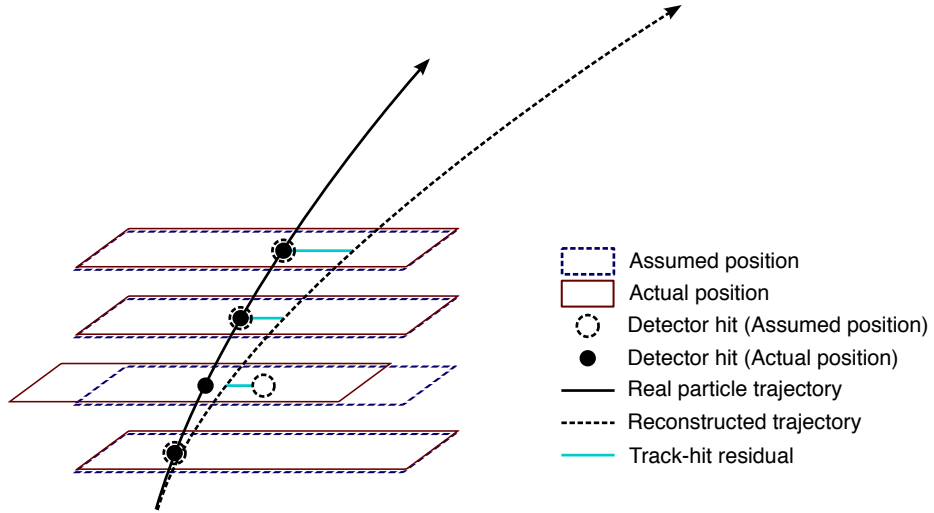


Figure 4.1: Graphical representation of the effect of a misaligned detector element. The reconstructed particle track (dashed arrow) differs from the actual trajectory of the particle (solid arrow) due to the shift in one of the detector elements. The cyan lines represent the track-to-hit residuals.

#### 443 4.1 The Alignment Method

444 The alignment procedure uses track-based algorithm that updates the locations of detector elements  
 445 in order to minimize the set of track-hit *residuals*. These residuals are defined as the distance between  
 446 the fitted track position in a given detector element to the position of the hit recorded by the same  
 447 element. Tracks in ATLAS are parameterized as five-dimensional vectors [7]:

$$\vec{r} = (d_0, z_0, \phi_0, \theta, q/p) \quad (4.1)$$

448 where  $d_0$  and  $z_0$  are the transverse and longitudinal impact parameters with respect to the origin,  
 449 respectively,  $\phi_0$  is the azimuthal angle of the track at the point of closest approach to the origin,  $\theta$   
 450 is the polar angle, and  $q/p$  is the charge of the track divided by its momentum. The residual for the  
 451  $i^{\text{th}}$  hit of a given track can then be written in terms of the track parameters  $\vec{r}$  and a set of alignment  
 452 parameters  $\vec{a}$  that describe the hit location [8]:

$$r_i(\vec{r}, \vec{a}) = (\vec{m}_i - \vec{e}_i(\vec{r}, \vec{a})) \cdot \hat{k} \quad (4.2)$$

453 where  $\vec{e}_i$  is the intersection point of the extrapolated track with the sensor,  $\vec{m}_i$  is the position of the  
 454 associated hit within the sensor, and  $\hat{k}$  is the unit vector defining the direction of the measurement  
 455 within the sensor.  $\vec{r}$  is then the vector of residuals for the given track.

456 A  $\chi^2$  function can be built from the residuals of all collected tracks:

$$\chi^2 = \sum_{\text{tracks}} \vec{r}^T V^{-1} \vec{r} \quad (4.3)$$

457 where  $V$  is the covariance matrix of the hit measurements. The  $\chi^2$  function is then minimized with  
 458 respect to the alignment parameters  $\vec{a}$ , which contain all degrees of freedom being aligned. The  
 459 minimization condition with respect to  $\vec{a}$  is:

$$\frac{d\chi^2}{d\vec{a}} = 0 \rightarrow 2 \sum_{\text{tracks}} \left( \frac{d\vec{r}}{d\vec{a}} \right)^T V^{-1} \vec{r} = 0 \quad (4.4)$$

460 This equation can be difficult to solve exactly, so the residual is rewritten as a first order Taylor  
 461 expansion:

$$\vec{r} = \vec{r}_0 + \frac{d\vec{r}}{d\vec{a}} \delta\vec{a} \quad (4.5)$$

462 where  $\vec{r}_0$  is dependent on an initial set of track and alignment parameters  $\vec{r}_0$  and  $\vec{a}_0$ , respectively;  
 463 the track parameter dependence has also been folded into the total derivative  $\frac{d\vec{r}}{d\vec{a}}$ . Equation 4.5 can  
 464 then be inserted into the minimization condition from Equation 4.4 to give:

$$\left[ \sum_{\text{tracks}} \left( \frac{d\vec{r}}{d\vec{a}} \right)^T V^{-1} \left( \frac{d\vec{r}}{d\vec{a}} \right) \right] \delta\vec{a} + \sum_{\text{tracks}} \left( \frac{d\vec{r}}{d\vec{a}} \right)^T V^{-1} \vec{r}_0 = 0 \quad (4.6)$$

465 From this equation, the alignment matrix  $\mathcal{M}_a$  and alignment vector  $\vec{\nu}_a$  can be defined:

$$\mathcal{M}_a = \sum_{\text{tracks}} \left( \frac{d\vec{r}}{d\vec{a}} \right)^T V^{-1} \left( \frac{d\vec{r}}{d\vec{a}} \right) \quad (4.7)$$

466

$$\vec{\nu}_a = \sum_{\text{tracks}} \left( \frac{d\vec{r}}{d\vec{a}} \right)^T V^{-1} \vec{r}_0 \quad (4.8)$$

467 Finally, the alignment corrections  $\delta\vec{a}$  can be solved for by inverting the alignment matrix:

$$\delta\vec{a} = -\mathcal{M}_a^{-1} \vec{\nu}_a \quad (4.9)$$

468 which is a linear system of equations with a number of equations equal to the number of alignment  
 469 degrees of freedom [9].

470 Inverting the matrix and solving this system of equations is referred to as *Global  $\chi^2$  alignment* [8].  
 471 This can be useful, as  $\mathcal{M}_a$  contains all the correlations between the alignable structures. However,  
 472 inverting the matrix becomes difficult when the number of degrees of freedom becomes large, and  
 473 as the number of alignable structures increases, so too does the size of the matrix  $\mathcal{M}_a$ . Eventually  
 474 inverting the matrix becomes too computationally intensive to be practical.

475 This problem is solved by the *Local*  $\chi^2$  algorithm [10]. In this case, the alignment matrix is  
 476 constructed to be block-diagonal, allowing for it to be inverted even for large numbers of degrees of  
 477 freedom. This is achieved by replacing the full derivative in Equation 4.6 with the partial derivative  
 478  $\frac{\partial \vec{r}}{\partial \vec{a}}$ . The new alignment matrix  $\mathcal{M}'_a$  and alignment vector  $\vec{\nu}'_a$  become:

$$\mathcal{M}_a = \sum_{\text{tracks}} \left( \frac{\partial \vec{r}}{\partial \vec{a}} \right)^T V^{-1} \left( \frac{\partial \vec{r}}{\partial \vec{a}} \right) \quad (4.10)$$

$$\vec{\nu}_a = \sum_{\text{tracks}} \left( \frac{\partial \vec{r}}{\partial \vec{a}} \right)^T V^{-1} \vec{r}_0 \quad (4.11)$$

480 Inverting  $\mathcal{M}'_a$  is considerably faster and less intensive even for large numbers of degrees of freedom;  
 481 however, the correlations between the alignable structures is lost.

482 Due to the Taylor expansion used in Equation 4.6, several iterations of the alignment algorithm  
 483 may be necessary to converge on a final set of alignment constants. The Local  $\chi^2$  alignment typically  
 484 requires more iterations due to the loss of the correlation information [11]. In practice, the ATLAS  
 485 reconstruction is run over a set of events, and the resulting tracks are fed to the alignment algorithm.  
 486 The residuals are calculated, the alignment matrix is built and inverted, and a new set of alignment  
 487 constants is obtained. The convergence of the alignment can be checked by:

- 488 1. Measure the  $\Delta\chi^2$  with the previous iteration. If it is near zero, then the  $\chi^2$  is approaching its  
 489 minimum.
- 490 2. Looking at the residual distributions for different alignable structures. A well aligned detector  
 491 will have a mean residual of zero.

492 If the above checks are satisfied, the process is finished and the final alignment constants are read  
 493 out; if not, another iteration is performed. A visual representation of the alignment chain is shown  
 494 in Figure 4.2.

495 Since a  $\chi^2$  minimization is used to align the detector, if there is a systematic misalignments in  
 496 the detector that does not adversely affect the  $\chi^2$ , the algorithm will be insensitive to it. These  
 497 misalignments are referred to as *weak modes*, and special care is taken to remove them [12]. One  
 498 potential impact of weak modes is a bias in the track momentum of reconstructed particles. This  
 499 particular effect is the subject of Section 4.3.

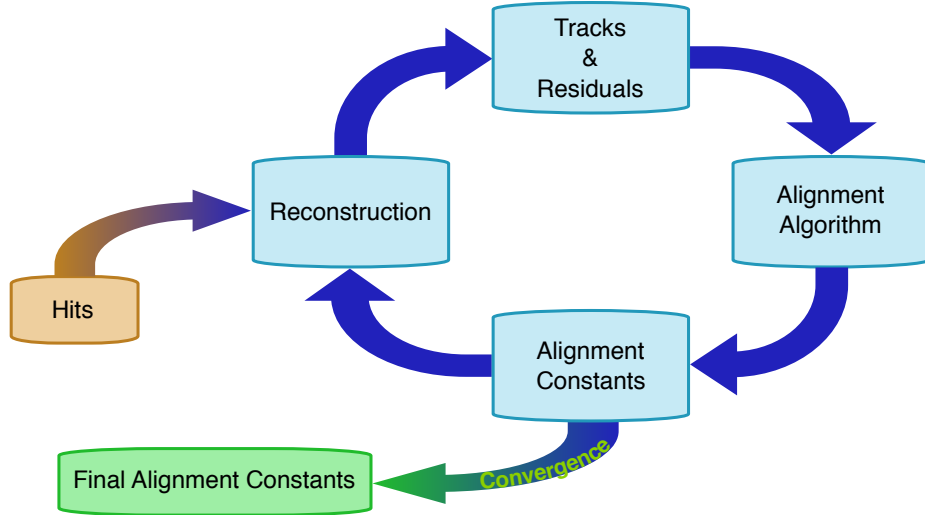


Figure 4.2: Graphical representation of the ID alignment chain.

#### 500 4.1.1 Alignment levels

501 The alignment of the detector is performed at several levels of increasing granularity. This adds  
 502 flexibility in being able to align only as finely as needed, and it also allows for global, detector-level  
 503 misalignments to be corrected first before dealing with finer adjustments.

- 504 • Level 1 (L1) alignment involves moving entire subdetector components as a single unit, such  
 505 as the entire Pixel detector, or the SCT barrel. These often have the largest misalignments,  
 506 but they are easily corrected and do not require large volumes of data to do so.
- 507 • Level 2 (L2) alignment treats individual layers in the silicon detectors (modules in the TRT)  
 508 and end cap disks as individual alignable objects.
- 509 • Level 2.7 (L27) alignment was introduced with the addition of the IBL to the ID in Run 2. It  
 510 involves the stave-by-stave alignment of the IBL and Pixel barrel<sup>3</sup>.
- 511 • Level 3 (L3) alignment treats each sensor in the silicon detectors and each straw in the TRT  
 512 as an individual alignable object. It is the finest grained alignment available but also the most  
 513 computationally intensive due to the large number of degrees of freedom. The large number  
 514 of individual detector sensors being aligned also requires the largest amount of statistics.

---

<sup>3</sup>For the purposes of this Chapter, the term “Pixel” will refer to the original three layers of the Pixel detector, and the IBL will be referenced separately.

515 The different alignment levels are listed in more detail in Table 4.1, including the number of alignable  
 516 structures and associated degrees of freedom for each detector component.

517 The implementation of the alignment algorithm in the software is flexible enough to allow each  
 518 subsystem to be aligned individually at a specified level. Each alignable structure has six degrees of  
 519 freedom: 3 translations ( $T_x, T_y, T_z$ ) and 3 rotations ( $R_x, R_y, R_z$ )<sup>4</sup>; however individual degrees of  
 520 freedom may be turned on and off as required. In a typical alignment job, L1 and L2 contain few  
 521 enough degrees of freedom that the Global  $\chi^2$  algorithm can be used, but L3 alignments (which can  
 522 contain over 36,000 degrees of freedom in the silicon detectors alone) require the Local  $\chi^2$  algorithm.

Level	Description of alignable structure	Structures	DoF
1	IBL detector	1	6
	Whole Pixel detector	1	6
	SCT barrel and 2 end-caps	3	18
	TRT barrel and 2 end-caps ( $T_z$ fixed)	3	17
Total:		8	47
2	IBL detector	1	6
	Pixel barrel layers	3	18
	Pixel end-cap disks	$2 \times 3$	36
	SCT barrel layers	4	24
	SCT end-cap disks	$2 \times 9$	108
	TRT barrel 32 modules ( $T_z$ fixed)	$3 \times 32$	480
	TRT end-cap wheels	$2 \times 40$	480
Total:		208	792
2.7	IBL staves	14	84
	Pixel barrel staves	$22+38+52$	672
	Pixel end-cap disks	$2 \times 3$	18
	Total:		132
3	IBL modules	280	1,680
	Pixel modules	1,744	10,464
	SCT modules	4,088	24,528
	TRT barrel wires ( $T_\phi, R_r$ only)	105,088	210,176
	TRT end-cap wires ( $T_\phi, R_Z$ only)	245,760	491,520
	Total silicon sensors:		6,112
Total TRT wires:		350,848	701,696

Table 4.1: The four alignment levels for each of the detector subsystems. The total number of alignable structures and degrees of freedom (DoF) to be aligned are given for each level.

<sup>4</sup>The TRT is an exception, as the subdetector does not have any resolution along the length of the straw. Therefore, for the barrel,  $T_z$  is omitted. Similarly for the straws themselves, only two parameters are defined: translation with respect to the radial direction ( $T_\phi$ ) and rotation with respect to the radial axis ( $R_r$  for the barrel and  $R_z$  for the end-caps) [13].

523 **4.2 Early 2015 alignment of the ATLAS detector**

524 List and cite previous major alignment efforts

525 brief blurb on 2015 cosmic alignment to set stage for this paper

526 **4.2.1 Alignment of the IBL**

527 thinking this should probably be a section not a subsection since it's not directly related to the 2015

528 paper i'm basing the previous section on... idk.

529 **4.3 Momentum Bias Corrections**

530 Hello world!

531 **4.4 Alignment Monitoring**

532 Hello world!

## CHAPTER 5

---

# Measurement of same-sign $WW$ production at $\sqrt{s} = 13$ TeV with ATLAS

---

536 Production of same-sign  $W$  boson pairs is a particularly interesting SM process. When produced  
 537 via vector boson scattering (VBS),  $W^\pm W^\pm jj$  is particularly sensitive to the electroweak symmetry  
 538 breaking (EWSB) mechanism as well as potential “beyond the Standard Model” (BSM) physics.  
 539  $W^\pm W^\pm jj$  events can be produced via electroweak-mediated (EWK) diagrams, of which VBS is a  
 540 subset, or QCD-mediated diagrams. The biggest advantage of same-sign  $W^\pm W^\pm jj$  lies in its ratio  
 541 of electroweak (EWK) to QCD production cross sections. Despite the opposite-sign  $W^\pm W^\mp$  having  
 542 a considerably larger total cross section, its EWK-mediated diagrams are considerably smaller than  
 543 its QCD-mediated diagrams, while for same-sign  $W^\pm W^\pm$  the ratio is approximately one to one.  
 544 This makes  $W^\pm W^\pm jj$  one of the best channels for studying VBS at the LHC.

545 The first evidence of electroweak (EWK)  $W^\pm W^\pm jj$  production was seen by the ATLAS and  
 546 CMS experiments at  $\sqrt{s} = 8$  TeV with excesses of  $3.6\sigma$  [14] and  $2.0\sigma$  [15] over backgrounds, respec-  
 547 tively. More recently, ATLAS and CMS have both observed the EWK process at  $\sqrt{s} = 13$  TeV  
 548 with significances of  $6.9\sigma$  [1] and  $5.5\sigma$  [16], respectively. The analysis presented in this chapter  
 549 is based off of the ATLAS  $\sqrt{s} = 13$  TeV observation and cross section measurement of EWK  
 550  $W^\pm W^\pm jj$  production [1, 17].

551 **5.0.1 Theoretical overview of vector boson scattering**

552 VBS processes are very important to understand due to their sensitivity to the EWSB mechanism.  
 553 The scattering amplitude of longitudinally polarized vector bosons grows with center-of-mass energy  
 554 and ultimately violates unitarity above  $\sqrt{s} = 1$  TeV in the absence of a light SM Higgs boson [18, 19].

555 However, once the Higgs is introduced, the divergences cancel and the cross section no longer grows  
 556 unbounded, as can be seen in Figure 5.1, which consists of plots from [20].

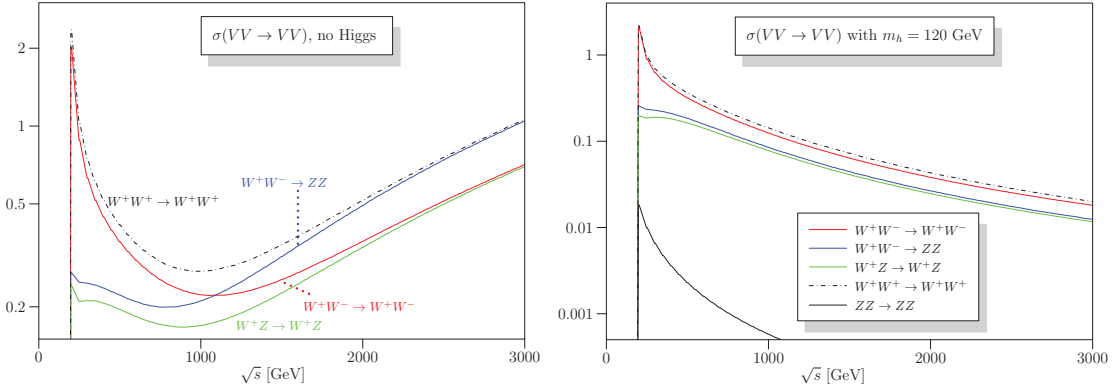


Figure 5.1: Cross sections in nanobarns for five different scattering processes of longitudinally polarized vector bosons as a function of center of mass energy  $\sqrt{s}$ . Without a SM Higgs boson (left), the cross sections grow unbounded with  $\sqrt{s}$ ; however with a 120 GeV Higgs boson (right), the cross sections no longer diverge. Plots taken from [20].

557 With the discovery of the Higgs boson in 2012 [21, 22], the EWSB mechanism can now be directly  
 558 studied. Due to the exchange of a Higgs in the  $s$ - and  $t$ -channel VBS diagrams ( $W^\pm W^\pm jj$  itself only  
 559 contains the  $t$ -channel diagram), VBS processes are directly sensitive to properties of the Higgs. For  
 560 example, the high-mass tail in the  $VV$  scattering system allows an approximation of the effective  
 561 coupling strength of the Higgs to vector bosons that is independent of any assumptions on the Higgs  
 562 width [23]. Additionally, the center of mass energy dependence of the  $VV$  scattering can reveal  
 563 whether the Higgs boson unitarizes the longitudinal scattering amplitude fully or only partially [24].

564 VBS events are characterized by two quarks from the colliding protons each radiating a massive  
 565 vector boson which then scatter and decay in the detector. The incoming quarks carry a large  
 566 amount of momentum and only deflect a small amount upon radiating the vector boson; as a result,  
 567 they often travel very close to the beam line. Ignoring the decay products of the bosons, these VBS  
 568 events result in a final state of two vector bosons ( $V$ ) and two jets ( $j$ ) at high pseudorapidities  
 569 (called *forward jets*) from the outgoing quarks. The shorthand  $VVjj$  is used to represent this final  
 570 state.

571  $VVjj$  events can be produced via two different physical processes. The first involves purely  
 572 electroweak interactions in the tree-level diagrams, with  $\mathcal{O}(\alpha_{EWK}) = 6$  and will be referred to as  
 573 *EWK production*. This can be further broken down into VBS and non-VBS production. In the  
 574 VBS EWK production, the scattering occurs via triple or quartic gauge couplings, as well as the

575  $s$ - or  $t$ -channel exchange of a Higgs boson. The non-VBS EWK production contains the same final  
 576 state of two vector bosons and two outgoing quarks, but the bosons do not scatter. Due to gauge  
 577 invariance, it is not possible to separate the VBS from the non-VBS productions [25]; therefore,  
 578 both are included in the signal generation and are indistinguishable from one another. The second  
 579 process involves a mix of the EWK and strong interactions, of order  $\mathcal{O}(\alpha_s) = 2 \otimes \mathcal{O}(\alpha_{\text{EWK}}) = 4$  and  
 580 will be referred to as *QCD production*. The tree-level Feynman diagrams for VBS EWK, non-VBS  
 581 EWK, and QCD  $VVjj$  production are found in Figures 5.2, 5.3, and 5.4, respectively.

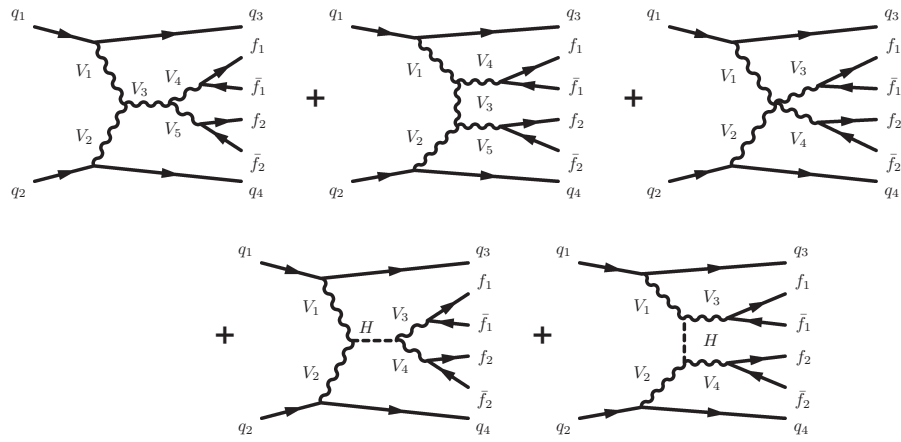


Figure 5.2: Tree-level Feynman diagrams for VBS EWK  $VVjj$  production including triple gauge couplings involving  $W$  and/or  $Z$  bosons (top left and top middle), quartic gauge coupling (top right), or the exchange of a Higgs boson ( $s$ -channel bottom left and  $t$ -channel bottom right). The labels are quarks ( $q$ ), fermions ( $f$ ), and gauge bosons ( $V = W, Z$ ).

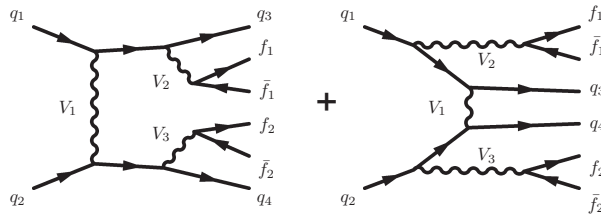


Figure 5.3: Tree-level Feynman diagrams for non-VBS EWK  $VVjj$  production. The labels are quarks ( $q$ ), fermions ( $f$ ), and gauge bosons ( $V = W, Z$ ).

### 582 5.0.2 Same-sign $W^\pm W^\pm$ scattering

583 Same-sign  $W^\pm W^\pm jj$  scattering is considered to be one of the best channels for studying VBS at the  
 584 LHC [23]. This is due primarily to the ratio of the EWK to the QCD production, which matters

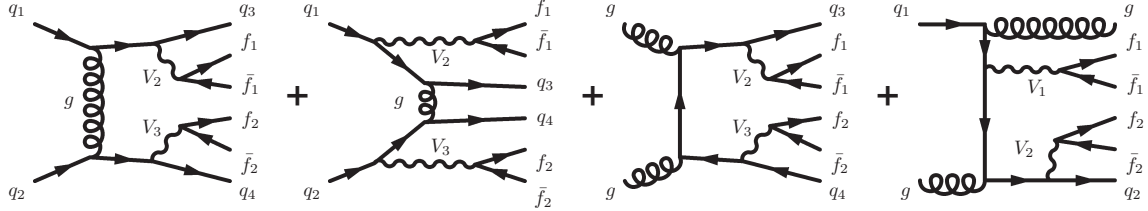


Figure 5.4: Tree-level Feynman diagrams for QCD  $VVjj$  production. The labels are quarks ( $q$ ), fermions ( $f$ ), and gauge bosons ( $V = W, Z$ ).

585 a great deal due to the VBS events being a subset of the total EWK production. In an analysis  
 586 the EWK production would be considered the signal and the QCD production a background, so a  
 587 favorable ratio of the two helps greatly when comparing the size of the signal to the backgrounds.  
 588 A study at  $\sqrt{s} = 8$  TeV [26] was done using the **SHERPA** Monte Carlo (MC) generator to calculate  
 589 EWK and QCD production cross sections at leading order for a variety of  $VVjj$  processes decaying  
 590 to leptons and can be found in Table 5.1. Despite its lower cross section compared to other  $VVjj$   
 591 processes, the EWK to QCD ratio for  $W^\pm W^\pm jj$  is approximately one-to-one, whereas for opposite-  
 592 sign  $W^\pm W^\mp jj$  the ratio is closer to 3%.

Process	Final state	$\sigma_{\text{EWK}}$	$\sigma_{\text{QCD}}$
$W^\pm W^\pm$	$l^\pm l^\pm \nu\nu jj$	19.5 fb	18.8 fb
$W^\pm W^\mp$	$l^\pm l^\mp \nu\nu jj$	91.3 fb	3030 fb
$W^\pm Z$	$l^\pm l^\pm l^\mp \nu jj$	30.2 fb	687 fb
$ZZ$	$l^+ l^- \nu\nu jj$	2.4 fb	162 fb
$ZZ$	$l^+ l^- l^+ l^- jj$	1.5 fb	106 fb

Table 5.1: Predicted cross sections for EQK and QCD production of diboson processes relevant to VBS at  $\sqrt{s} = 8$  TeV using the **SHERPA** MC generator. Loose generator level cuts are applied on lepton  $p_T > 5$  GeV, dilepton invariant mass  $m_{ll} > 4$  GeV, and at least two jets with  $m_{jj} > 10$  GeV. Numbers taken from [26].

593 This analysis studies  $W^\pm W^\pm jj$  scattering where both  $W$  bosons decay leptonically to  $e\nu$  or  $\mu\nu$ <sup>5</sup>.  
 594 The  $W^\pm W^\pm jj$  VBS final state consists of two leptons with the same electric charge, two neutrinos,  
 595 and two high energy forward jets with a large invariant mass. Tree-level Feynman diagrams of VBS  
 596  $W^\pm W^\pm jj$  production can be found in Figure 5.5 and a visual representation of the VBS topology  
 597 can be found in Figure 5.6. The two forward jets also serve as a powerful tool to suppress the  
 598 QCD production mode. In EWK events, the two jets tend to have much higher separation and a  
 599 larger combined invariant mass than the two leading jets in a QCD event. The two plots shown in

<sup>5</sup>Throughout the rest of this chapter,  $l$  denotes either electrons ( $e$ ) or muons ( $\mu$ ) unless stated otherwise. Additionally,  $e$ ,  $\mu$ , and  $\nu$  (neutrino) with no charge or anti-particle designation refer interchangeably to either the particle or anti-particle.

600 Figure 5.7 highlight the differences in these dijet quantities between the two production modes. An  
 601 ATLAS event display of a real  $W^\pm W^\pm jj$  candidate event is shown in Figure 5.8.

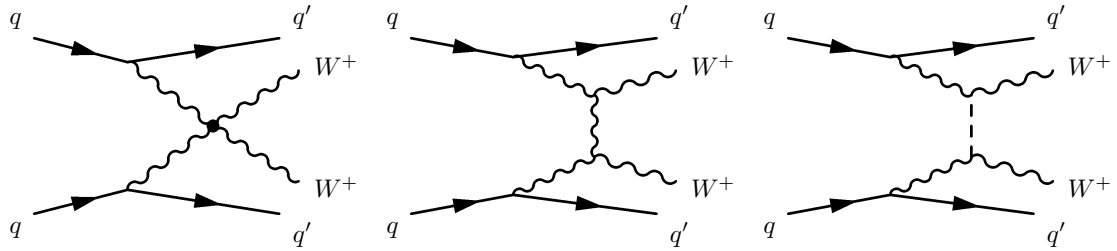


Figure 5.5: Feynman diagrams for VBS EWK production of  $W^\pm W^\pm jj$  events. The leftmost diagram contains a quartic gauge coupling vertex, and the rightmost diagram contains an exchange of a Higgs boson. **TODO: Make diagrams consistent with others**

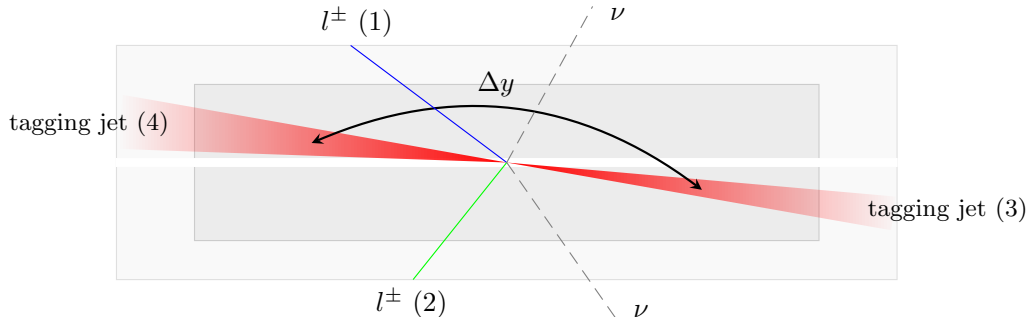


Figure 5.6:  $W^\pm W^\pm jj$  VBS event topology containing two leptons (1 and 2) with the same electric charge, two neutrinos, and two forward tagging jets (3 and 4) with large rapidity separation  $\Delta y$ .

### 602 5.0.3 Overview of backgrounds

603 In addition to QCD production of  $W^\pm W^\pm jj$  events, there are several other processes that can end  
 604 up with a final state of two same-sign leptons, two neutrinos, and two jets. However, due to the  $\pm 2$   
 605 final state charge, there is a considerable reduction in SM backgrounds (such as  $Z$  boson events)  
 606 when compared to an analysis like opposite-sign  $W^\pm W^\mp jj$ .

607 One of the largest sources of background involves processes with prompt leptons<sup>6</sup>. These are  
 608 events that contain two leptons with the same electric charge and one or more additional leptons

<sup>6</sup>Prompt leptons are those that are produced in the primary collision and are a direct decay product of the process of interest. Non-prompt leptons originate from some secondary process, such as a  $b$ -hadron decay, or are jets that get mis-reconstructed as a lepton.

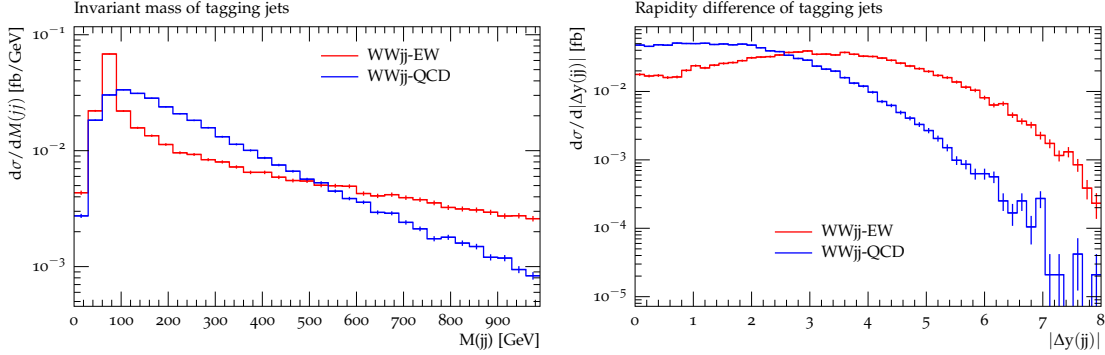


Figure 5.7: Generator level comparisons at  $\sqrt{s} = 8$  TeV of dijet invariant mass ( $m_{jj}$ , left) and dijet rapidity ( $\Delta y_{jj}$ , right) in EWK (red) and QCD (blue)  $W^\pm W^\pm jj$  events. Both data sets have been normalized to the same area. Plots taken from [26].

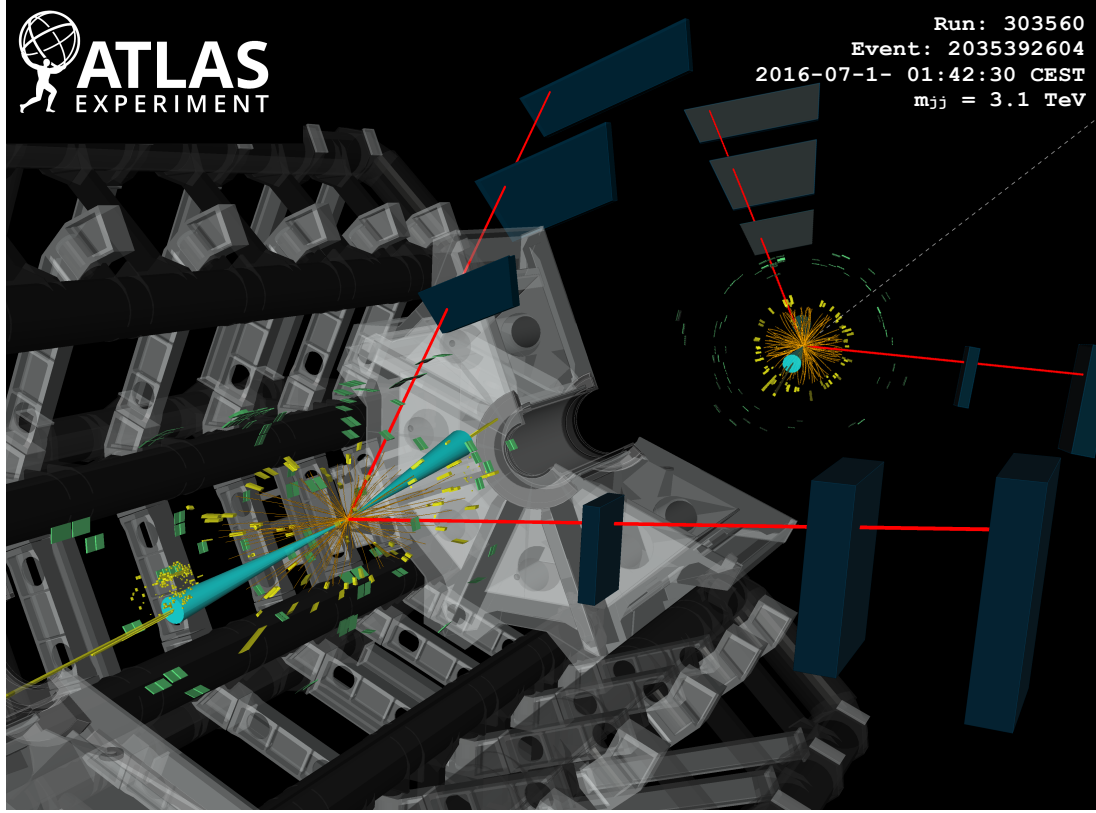


Figure 5.8: ATLAS event display of a  $pp \rightarrow W^\pm W^\pm \rightarrow \mu^\pm \nu_\mu \mu^\pm \nu_\mu jj$  event. The muons are represented by the red lines travelling from the ID through the MS, and the forward jets are represented by the blue cones with yellow energy deposits in the calorimeters. The direction of the  $E_T^{\text{miss}}$  in the transverse plane is indicated by the gray dashed line in the inset image. Event display taken from [1].

609 that are “lost”, either by failing the selection criteria or falling outside of the detector’s acceptance.  
 610 The number of processes that can contribute is limited by the requirement of same-sign leptons, and  
 611 as a result this background is dominated by processes involving two or more vector bosons, with the  
 612 largest contribution coming from  $WZ$  events and smaller contributions from  $ZZ$  and  $t\bar{t}V$  events.  
 613 Triboson events where one boson decays hadronically also contribute to this background; however,  
 614 the jets are generally softer and more central than in a typical VBS event, and the cuts applied on  
 615 the forward jets suppress these contributions.

616 The other dominant background comes from non-prompt, or “fake”, leptons. Here one or more  
 617 leptons originate from the decay of another particle unrelated to the signal process, such as a  
 618 heavy-flavor decay or photon conversion, or come from a jet that is misidentified as a lepton. This  
 619 background is mostly made up of events from  $t\bar{t}$  and  $W+\text{jets}$  processes, with a much smaller contribu-  
 620 tion from  $V\gamma$  events. **TODO: check whether  $V\gamma$  really qualifies as non-prompt, we lump  $Z\gamma$  in**  
**621 with the charge flip background in the paper...**

622 Finally, opposite-sign lepton pairs can enter the signal region if one of the leptons is reconstructed  
 623 with the wrong charge (called *charge misidentification*<sup>7</sup>). In practice, this only affects events with  
 624 electrons, as the charge misidentification rate for muons is negligible [27]. This is a major background  
 625 in events with two electrons, but is a much smaller contribution for events with one electron and  
 626 one muon.

## 627 5.1 Data and Monte Carlo samples

628 This analysis uses  $36.1 \text{ fb}^{-1}$  of  $\sqrt{s} = 13$  TeV proton-proton collision data recorded by ATLAS  
 629 during 2015 and 2016. The uncertainty in the combined integrated luminosity is 2.1%. It is derived  
 630 following a methodology similar to that detailed in [28] and using the LUCID-2 detector for the  
 631 baseline luminosity measurements [29] from calibration of the luminosity scale using  $x$ - $y$  beam-  
 632 separation scans.

### 633 5.1.1 Monte Carlo samples

634 A number of Monte Carlo (MC) simulations are employed to model signal and background pro-  
 635 cesses. In order to model the real collision data as closely as possible, each MC has been run through  
 636 a full simulation of the ATLAS detector [30] in GEANT4 [31], and events have been reconstructed

---

<sup>7</sup>Charge misidentification is also referred to interchangeably as *charge mis-ID* and *charge flip*.

637 using the same algorithms as the data. The simulation reproduces as closely as possible the momentum  
 638 resolutions and calorimeter responses of the detector, and also includes the effects of pileup by  
 639 including soft QCD interactions using PYTHIA v8.1 [32]. The MC samples used in this analysis are  
 640 detailed in this section and summarized in Table 5.2.

641 The  $W^\pm W^\pm jj$  samples are modeled using SHERPA v2.2.2 [33, 34, 35] with the NNPDF3.0 PDF  
 642 set [36]. The EWK signal samples are generated by fixing the electroweak coupling constant to  
 643  $\mathcal{O}(\alpha_W) = 6$ , and a QCD background sample was also generated with  $\mathcal{O}(\alpha_W) = 4$ . SHERPA includes  
 644 up to one parton at next-to-leading order (NLO) and up to three at leading order (LO) in the  
 645 strong coupling constant  $\alpha_s$ . A second  $W^\pm W^\pm jj$  EWK sample is generated using POWHEG-BOX  
 646 v2 [37] with the NNPDF3.0 PDF set and at NLO accuracy. This sample is only used for systematic  
 647 studies, as POWHEG-BOX does not include resonant triboson contributions in its matrix element, which  
 648 are non-negligible at NLO [38].

649 Diboson processes ( $VV$  where  $V = W, Z$ ) are simulated with SHERPA v2.2.2 for mixed hadronic  
 650 and leptonic decays and SHERPA v2.2.1 for fully leptonic decays of the bosons. Similarly, triboson  
 651 ( $VVV$ ) and  $V\gamma$  processes are simulated using SHERPA v2.1.1 with up to one parton at NLO and up  
 652 to three at LO.  $W+jets$  processes are simulated with SHERPA2.2.1 with up to two partons at NLO  
 653 and four at LO. All the above SHERPA samples use the NNPDF3.0 PDF set and SHERPA's own parton  
 654 showering. The  $Z+jets$  events are generated with Madgraph5\_aMC@NLO [39] at LO and interfaced  
 655 with PYTHIA v8.1 for parton showering.

656  $t\bar{t}$  events are generated using POWHEG-BOX v2 with the CT10 PDF set [40].  $t\bar{t}V$  samples are  
 657 generated at NLO with Madgraph5\_aMC@NLO and the NNPDF3.0 PDF set interfaced with PYTHIA v8  
 658 for parton showering. Finally, single top events are generated with POWHEG-BOX v1 and the CT10f4  
 659 PDF set interfaced with PYTHIA v6 [41] for parton showering.

## 660 5.2 Object and event selection

661 This section details the selection criteria for objects used in the analysis as well as the selection for  
 662 signal events.

### 663 5.2.1 Object selection

664 Muons, electrons, and jets all must pass strict selection requirements to ensure that only high quality,  
 665 well measured objects are used. For leptons, a baseline selection is defined (called the *preselection*),  
 666 which all leptons must pass in order to be considered for the analysis. This preselection is an

Process	Generator	Comments
$W^\pm W^\pm jj$ (EWK)	SHERPA v2.2.2	Signal sample
$W^\pm W^\pm jj$ (EWK)	POWHEG-BOX v2	Systematics sample
$W^\pm W^\pm jj$ (QCD)	SHERPA v2.2.2	
Diboson	SHERPA v2.2.2	Both bosons decay leptonically ( $llll$ , $lll\nu$ , $ll\nu\nu$ )
Triboson	SHERPA v2.2.1	One boson decays leptonically, the other hadronically
$W + \text{jets}$	SHERPA v2.2.1	
$Z + \text{jets}$	Madgraph5_aMC@NLO	
$V\gamma$	SHERPA v2.1.1	
$V\gamma jj$ (EWK)	SHERPA v2.2.4	
$t\bar{t}V$	Madgraph5_aMC@NLO	
$t\bar{t}$	POWHEG-BOX v2	
Single top	POWHEG-BOX v1	EWK $t$ -, $s$ -, & $Wt$ -channels

Table 5.2: Summary of MC samples used in the analysis.

intentionally loose set of criteria in order to have high acceptance for rejecting backgrounds with additional leptons (i.e.  $WZ \rightarrow 3l\nu jj$ ). Signal leptons are then required to satisfy a much tighter *signal selection* aimed at suppressing backgrounds from non-prompt or fake leptons. A third set of lepton selection criteria, the *loose selection*, defines a sample enriched in non-prompt leptons, and it is used in the fake factor method for estimating the non-prompt background, discussed in detail in Section 5.3.4. Jets are only required to pass one set of selection criteria. These selections are detailed in the following sections and summarized in Table 5.3 for muons, Table 5.4 for electrons, and Table 5.5 for jets.

### 5.2.1.1 Muon candidate selection

Cuts on muon  $p_T$  serve to reject low momentum leptons from background processes and additional collisions from pileup events. Preselected muons must have  $p_T > 6$  GeV and signal muons  $p_T > 27$  GeV. The  $p_T$  requirement for loose muons is lower than for signal muons,  $p_T > 15$  GeV, for reasons that are discussed in Section 5.3.4. **TODO:** reference proper subsection when it's done

Muons are required to fall within the detector's  $\eta$  acceptance:  $|\eta| < 2.7$  for preselected muons, which is tightened to  $|\eta| < 2.5$  for the signal muons.

Cuts on the transverse and longitudinal impact parameters are applied to ensure that the candidate muon originated from the primary particle interaction and not some other source, such as a heavy flavor decay. The preselection and the loose selection both have looser requirements on the transverse impact parameter significance ( $d_0/\sigma_{d_0}$ ) than the signal selection; all three have the same requirement on the transverse impact parameter ( $|z_0 \times \sin \theta|$ ).

Finally, the muon candidates are required to pass a particle identification and an isolation criteria as defined in [42]. The methods used in constructing the identification and isolation workingpoints are described in more detail in Section 3.2.4.2. The muon identification serves to select prompt muons with high efficiency and well measured momenta. This analysis uses two different workingpoints, **Loose** for preselected muons and **Medium** for loose and signal muons, where **Medium** muons are a tighter subset of those that pass the **Loose** requirement. Muon isolation is a measurement of detector activity around the muon candidate, and it is measured with both track-based and calorimeter-based variables. The isolation workingpoint used for the signal muons, **Gradient**, is defined such that there is 90% or better background rejection efficiency for 25 GeV muons, and 99% efficiency at 60 GeV. There is no minimum isolation requirement for preselected or loose muons. Loose muons are additionally required to fail one or both of the signal transverse impact parameter cut and signal isolation requirement.

Muon preselection	
Momentum cut	$p_T > 6$ GeV
Angular acceptance	$ \eta  < 2.7$
Longitudinal impact parameter	$ z_0 \times \sin \theta  < 0.5$ mm
Transverse impact parameter	$d_0/\sigma_{d_0} < 10$
Particle identification	<b>Loose</b>

Muon signal selection	
Momentum cut	$p_T > 27$ GeV
Angular acceptance	$ \eta  < 2.5$
Longitudinal impact parameter	$ z_0 \times \sin \theta  < 0.5$ mm
Transverse impact parameter	$d_0/\sigma_{d_0} < 3$
Particle identification	<b>Medium</b>
Particle isolation	<b>Gradient</b>

Muon loose selection	
Momentum cut	$p_T > 15$ GeV
Angular acceptance	$ \eta  < 2.5$
Longitudinal impact parameter	$ z_0 \times \sin \theta  < 0.5$ mm
Transverse impact parameter	$d_0/\sigma_{d_0} < 10$
Particle identification	<b>Medium</b>
Fail signal transverse impact parameter and/or isolation cuts	

Table 5.3: Muon selection criteria. All muons are required to pass the preselection (top), and then either the signal (middle) or loose (bottom) criteria is applied to the preselected electrons.

---

<sup>699</sup> **5.2.1.2 Electron candidate selection**

<sup>700</sup> The electron candidate selections are very similar to those for muons. The  $p_T$  cut starts at  $p_T >$   
<sup>701</sup> 6 GeV for the preselection, increases to  $p_T > 20$  GeV for loose electrons, and finally to  $p_T > 27$  GeV  
<sup>702</sup> for signal electrons. The  $|\eta|$  cut for electrons requires  $|\eta| < 2.47$  for all electrons, with the region  
<sup>703</sup>  $1.37 \leq |\eta| \leq 1.52$  removed from loose and signal electrons. This region is where the electromagnetic  
<sup>704</sup> calorimeter transitions from the barrel to the endcaps and is not fully instrumented. Both the  
<sup>705</sup> transverse and longitudinal impact parameter cuts are the same for all electron selections.

<sup>706</sup> The electron particle identification uses a multivariate likelihood technique (LH) [43] detailed  
<sup>707</sup> in Section 3.2.4.3. Preselected electrons must pass the loosest LH workingpoint `LooseLH` with  
<sup>708</sup> an additional requirement that there be a reconstructed track hit in the first layer of the pixel  
<sup>709</sup> detector (a so-called  $B$ -layer hit). The LH requirement for the loose and signal electrons the tightness  
<sup>710</sup> of the identification using `MediumLH` and `TightLH`, respectively. As for isolation, the `Gradient`  
<sup>711</sup> workingpoint is required for signal electrons only. The loose electrons must fail one or both of the  
<sup>712</sup> signal identification and isolation requirements.

<sup>713</sup> **5.2.1.3 Jet candidate selection**

<sup>714</sup> The final objects that need to pass selection are jets. Jets are clustered using the anti- $k_t$  algo-  
<sup>715</sup> rithm [44] within a radius of  $\Delta R = 0.4$ . The jets are then calibrated using  $E_T$ - and  $\eta$ -dependent  
<sup>716</sup> correction factors that are trained using MC simulations [45]. These calibrated jets are then re-  
<sup>717</sup> quired to have  $p_T > 30$  GeV if they lie in the forward regions of the detector ( $2.4 < |\eta| < 4.5$ ) and  
<sup>718</sup>  $p_T > 25$  GeV in the central region ( $|\eta| \leq 2.4$ ). In order to suppress pileup jets, the so-called jet-  
<sup>719</sup> vertex-tagger (JVT) discriminant associates a jet with the primary interaction vertex [46]; central  
<sup>720</sup> jets with  $p_T > 60$  GeV are required to pass the `Medium` JVT workingpoint, which corresponds to  
<sup>721</sup> an average efficiency of over 92%. Finally, the jets are required to be separated by selected prompt  
<sup>722</sup> leptons by at least  $\Delta R(j, l) > 0.3$ .

<sup>723</sup> **5.2.1.4 Treatment of overlapping objects**

<sup>724</sup> In the event that one or more objects are reconstructed very close to each other, there is the  
<sup>725</sup> possibility for double-counting if both originated from the same object. The procedure by which  
<sup>726</sup> this ambiguity is resolved is called *overlap removal* (OR). The standard ATLAS recommendation  
<sup>727</sup> for OR is implemented in this analysis [47, 48] and is summarized in Table 5.6.

Electron preselection	
Momentum cut	$p_T > 6$ GeV
Angular acceptance	$ \eta  < 2.47$
Longitudinal impact parameter	$ z_0 \times \sin \theta  < 0.5$ mm
Transverse impact parameter	$d_0/\sigma_{d_0} < 5$
Particle identification	<b>LooseLH + <math>B</math>-layer hit</b>

Electron signal selection	
Momentum cut	$p_T > 27$ GeV
Angular acceptance	$ \eta  < 2.47$ , excluding $1.37 \leq  \eta  \leq 1.52$
Longitudinal impact parameter	$ z_0 \times \sin \theta  < 0.5$ mm
Transverse impact parameter	$d_0/\sigma_{d_0} < 5$
Particle identification	<b>TightLH</b>
Particle isolation	<b>Gradient</b>

Electron loose selection	
Momentum cut	$p_T > 20$ GeV
Angular acceptance	$ \eta  < 2.47$ , excluding $1.37 \leq  \eta  \leq 1.52$
Longitudinal impact parameter	$ z_0 \times \sin \theta  < 0.5$ mm
Transverse impact parameter	$d_0/\sigma_{d_0} < 5$
Particle identification	<b>MediumLH</b>
Fail signal identification and/or isolation cuts	

Table 5.4: Electron selection criteria. All electrons are required to pass the preselection (top), and then either the signal (middle) or loose (bottom) criteria is applied to the preselected electrons.

Jet selection	
Momentum cut	$p_T > 30$ GeV for $2.4 <  \eta  < 4.5$ $p_T > 60$ GeV for $ \eta  < 2.4$
JVT cut	<b>Medium</b>
Jet-lepton separation	$\Delta R(j, l) > 0.3$

Table 5.5: Jet selection criteria. All jets are required to pass the above selection in order to be used in the analysis.

728 Since electrons leave a shower in the EM calorimeter, every electron has a jet associated with  
 729 it. Therefore, any jets close to an electron (within  $\Delta R(e, j) < 0.2$ ) are rejected due to the high  
 730 probability that they are the same object. On the other hand, when jets and electrons overlap  
 731 within a large radius of  $0.2 < \Delta R(e, j) < 0.4$ , it is likely that the electron and jet both are part of  
 732 a heavy-flavor decay, and the electron is rejected.

733 High energy muons can produce photons via bremsstrahlung radiation or collinear final state  
 734 radiation which results in a nearby energy deposit in the calorimeters. Non-prompt muons from  
 735 hadronic decays produce a similar signature; however, in this case the jet has a higher track multiplicity  
 736 in the ID. It is possible to address both cases by rejecting the jet when the ID track multiplicity  
 737 is less than three and otherwise rejecting the muon for jets and muons within  $\Delta R(\mu, j) < 0.4$ .

738 In addition to the case above where muon bremsstrahlung results in a nearby reconstructed jet,  
 739 the ID track from the muon and the calorimeter energy deposit can lead to it being reconstructed  
 740 as an electron. In this case, if both a muon and an electron share a track in the ID, the muon is  
 741 kept and the electron is rejected, unless the muon is calorimeter-tagged<sup>8</sup>, in which case the muon is  
 742 removed in favor of the electron.

Overlap	Check	Result (remove → keep)
Electron & Jet	$\Delta R(e, j) < 0.2$	Jet → electron
	$0.2 < \Delta R(e, j) < 0.4$	Electron → jet
Muon & Jet	$\Delta R(\mu, j) < 0.4$ and Jet $N_{ID}$ tracks $< 3$	Jet → muon
	$\Delta R(\mu, j) < 0.4$ and Jet $N_{ID}$ tracks $\geq 3$	Muon → jet
Electron & Muon	Shared ID track	Electron → muon
	Shared ID track & muon is calo-tagged	Muon → electron

Table 5.6: Summary of the overlap removal procedure used in the analysis. If the criteria in the “check” column is met, in the “result” column, the object on the left of the arrow is removed in favor of the object on the right.

### 743 5.2.2 Signal event selection

744 After the objects have been selected, cuts are applied on a per-event level to select  $W^\pm W^\pm jj$  signal  
 745 events. The event selection is summarized in Table 5.8 and is detailed in this section. It includes  
 746 the results of an optimization performed using a multidimensional grid scan.

747 The initial event selection begins by choosing events that pass one or more of the trigger re-  
 748 quirements listed in Table 5.7. At least one signal lepton is “matched” to a passed trigger in order

<sup>8</sup>A calorimeter-tagged (CT) muon is a muon that is identified by matching an ID track to a calorimeter energy deposit. CT muons have relatively low reconstruction efficiency compared to those measured by the MS, but can be used to recover acceptance in regions of the detector where the MS does not have full coverage [42].

749 to ensure that it was indeed a signal lepton that fired the trigger. A collection of *event cleaning*  
 750 cuts must also be passed in order to remove events collected during periods in which one or more  
 751 components of the detector was not operating optimally. Finally, the events are required to contain  
 752 at least one interaction vertex. An event can have multiple reconstructed vertices from additional  
 753 proton-proton collisions that occurred in the same bunch crossing. In this case, the *primary vertex*  
 754 is determined by choosing the vertex with the largest sum of the  $p_T^2$  of its associated tracks.

	2015 data	2016 data
Electrons	$p_T > 24$ GeV and Medium ID	$p_T > 26$ GeV and Tight ID and Loose isolation
	$p_T > 60$ GeV and Medium ID	$p_T > 60$ GeV and Medium ID
	$p_T > 120$ GeV and Loose ID	$p_T > 140$ GeV and Loose ID
Muons	$p_T > 20$ GeV and Loose isolation $p_T > 50$ GeV	$p_T > 26$ GeV and Medium isolation $p_T > 50$ GeV

Table 5.7: Summary of trigger requirements for electrons and muons for  $\sqrt{s} = 13$  TeV data collected in 2015 and 2016. At least one of the triggers must be satisfied.

755 Events are then required to contain exactly two signal leptons with the same electric charge.  
 756 The dilepton pair must have a combined invariant mass of  $m_{ll} \geq 20$  GeV in order to suppress low  
 757 mass Drell-Yan backgrounds. Two additional selections are applied to events in the  $ee$ -channel:  
 758 both electrons are required to have  $|\eta| < 1.37$  with an invariant mass at least 15 GeV away from  
 759 the  $Z$ -boson mass to reduce events where one electron is reconstructed with the wrong charge (this  
 760 background will be discussed in more detail in Section 5.3 TODO: Replace with proper subsection  
 761 once it's written). To suppress backgrounds from events with more than two leptons, events with  
 762 more than two leptons passing the preselection are vetoed.

763 Missing transverse energy ( $E_T^{\text{miss}}$ ) represents any particles that escape the detector without  
 764 being measured, such as neutrinos, and is defined as the magnitude of the vector sum of transverse  
 765 momenta of all reconstructed objects. It can be difficult to calculate accurately, as it involves  
 766 measurements from all subsystems within the detector, and it is sensitive to any corrections that  
 767 may be applied to the reconstructed physics objects [49]. These corrections, including the momentum  
 768 smearing for muons, energy scale and smearing for electrons, and jet calibrations, are propagated  
 769 to the  $E_T^{\text{miss}}$  calculation. Events are required to contain  $E_T^{\text{miss}} > 30$  GeV in order to account for the  
 770 two neutrinos from the  $W$  boson decays.

771 At least two jets are required. The leading and subleading jets must have  $p_T > 65$  GeV and  
 772  $p_T > 35$  GeV, respectively, and are referred to as the *tagging jets*. Events are vetoed if they contain  
 773 one or more jets that have been tagged as a  $b$ -jet to suppress backgrounds from heavy flavor decays

774 (especially top quark events). The  $b$ -tagging algorithm used by ATLAS is a boosted decision tree  
775 (BDT) called MV2c10, and this analysis uses a workingpoint with 85% efficiency [50].

776 Finally, cuts are applied on the VBS signature outlined in Section 5.0.2. The tagging jets are  
777 required to have a dijet invariant mass  $m_{jj} > 200$  GeV and be separated in rapidity by  $|\Delta y_{jj}| > 2.0$ .  
778 This preferentially selects the VBS EWK events over the QCD-produced  $W^\pm W^\pm jj$  events.

Event selection	
Event preselection	Pass at least one trigger with a matched lepton Pass event cleaning At least one reconstructed vertex
Lepton selection	Exactly two leptons passing signal selection Both signal leptons with the same electric charge $ \eta  < 1.37$ and $ M_{ee} - M_Z  > 15$ GeV ( $ee$ -channel only) Veto events with more than two preselected leptons
Missing transverse energy	$E_T^{\text{miss}} \geq 30$ GeV
Jet selection	At least two jets Leading jet $p_T > 65$ GeV Subleading jet $p_T > 35$ GeV $m_{jj} > 200$ GeV $N_{b\text{-jet}} = 0$ $ \Delta y_{jj}  > 2.0$

Table 5.8: The signal event selection.

### 779 5.3 Background estimations

780 The major sources of background events are summarized in Section 5.0.3, and the methods used to  
781 estimate them are detailed in this section. Prompt backgrounds from  $ZZ$  and  $t\bar{t}V$  are estimated  
782 directly from MC simulations. The shape of the  $WZ$  and  $V\gamma$  backgrounds are taken from MC, and  
783 the predicted yeilds are normalized to the data predictions in dedicated control regions, as outlined  
784 in Sections 5.3.1 and 5.3.2, respectively. Opposite sign events with a charge misidentified electron  
785 are estimated by a data-driven background method which is summarized in Section 5.3.3. Finally, a  
786 *fake factor* method is used to estimate the contributions from non-prompt backgrounds and is the  
787 subject of Section 5.3.4.

#### 788 5.3.1 Estimation of the $WZ$ background

789 The dominant background involving prompt leptons comes from  $WZ + \text{jets}$  events. The contribution  
790 is estimated from MC simulation and normalized to data in a control region enriched in  $WZ$  events

defined by the same event selection as Table 5.8 for the signal region, with the following changes applied to increase the purity of the  $WZ$  process:

- The third lepton veto is inverted, requiring a third lepton with  $p_T > 15$  GeV
- Two of the leptons must make a same-flavor opposite-sign pair. If more than one pair exists, the one with  $m_{ll}$  closest to the  $Z$  boson mass is chosen.
- The trilepton invariant mass is required to be  $m_{lll} > 106$  GeV to reduce contributions from  $Z\gamma$  and  $Z+jets$

Once the event yields in the control region are calculated, they are propagated to the final signal region fit, detailed in Section 5.4.1, in a single bin combining all the lepton channels. The systematic uncertainties of the  $WZ$  background are also calculated at this time. The event yields for the  $WZ$  control region are listed in Table 5.9, and distributions of the leading lepton  $p_T$  and  $\eta$  as well as trilepton invariant mass  $m_{lll}$  are found in Figures 5.10 and 5.9, respectively.

Event yields in the $WZ$ control region	
$WZ$	$197.9 \pm 1.4$
$ZZ$	$14.1 \pm 0.3$
Triboson	$1.26 \pm 0.1$
top	$10.8 \pm 1.1$
$Z\gamma$	$3.1 \pm 1.1$
$Z+jets$	$2.5 \pm 1.4$
Total prediction	$229.7 \pm 2.5$
Data	$201 \pm 14.2$

Table 5.9: Event yields in the  $WZ$  control region before normalization. All lepton flavor channels are combined.

### 5.3.2 Estimation of the $V\gamma$ background

Events from  $V\gamma$  processes can pass selection if the photon converts into an  $e^+e^-$  pair and one of the electrons passes the selection criteria. The background is estimated from MC simulations which are then scaled by a normalization factor calculated from a control region enriched in  $Z(\mu^+\mu^-)\gamma$  events. This control region selects two opposite-sign muons and an additional electron that is assumed to come from the photon conversion. The full event selection is detailed in Table 5.10.

The  $Z\gamma$  MC samples available do not cover the full range of  $p_T^\gamma$  and  $\Delta R(\gamma, l)$ ; thus, additional Drell-Yan samples ( $Z+jets$ ) are used to fill out the phase space. Overlap between the two samples

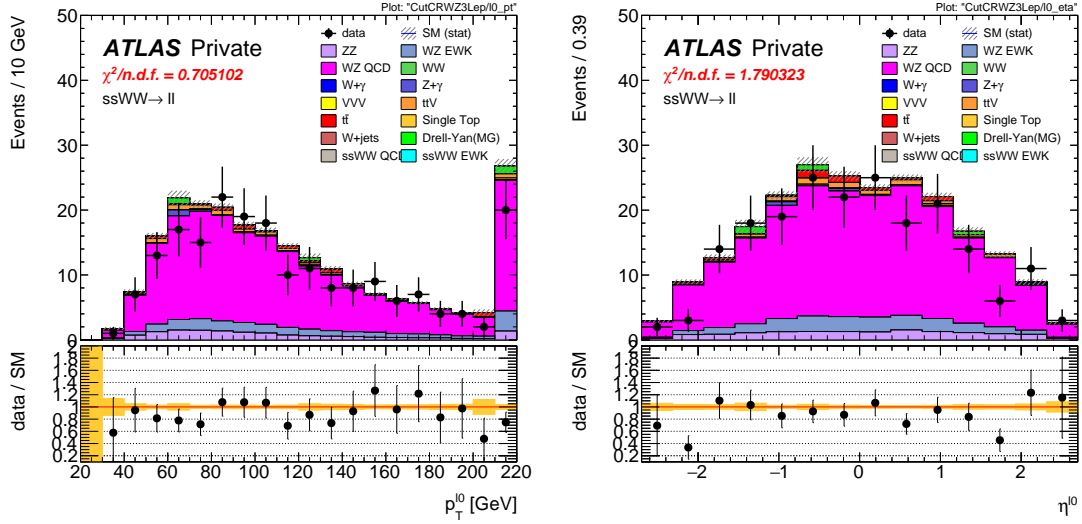


Figure 5.9: Leading lepton  $p_T$  (left) and  $\eta$  (right) distributions in the  $WZ$  control region before normalization. All lepton channels are combined.

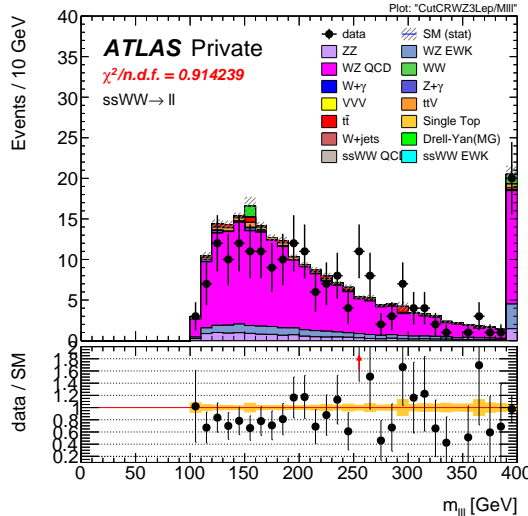


Figure 5.10: Trilepton invariant mass  $m_{lll}$  distribution in the  $WZ$  control region before normalization. All lepton channels are combined.

$V\gamma$ control region
Exactly two muons with $p_T > 27$ GeV and $p_T > 20$ GeV
Exactly one additional electron with $p_T > 15$ GeV
Remove overlap between $Z+jets$ and $Z\gamma$
Di-muon + photon invariant mass $75 < M_{\mu\mu\gamma} < 100$ GeV
$E_T^{\text{miss}} < 30$ GeV

Table 5.10: Selection criteria for the  $V\gamma$  control region.

811 are removed based to avoid double counting. Events with final state photons at truth level are  
 812 checked to ensure that the photon did not originate from a hadronic decay. Cuts on  $p_T^\gamma > 10$  GeV  
 813 and  $\Delta R(\gamma, l) > 0.1$  are then applied at generator level, and  $Z\gamma$  events that fail and  $Z+jets$  events  
 814 that pass this additional selection are removed.

815 The normalization factor is calculated directly from the event yields in the  $V\gamma$  control region  
 816 rather than in the signal fit, as is done for the  $WZ$  background. The event yields are listed in  
 817 Table 5.11, and the normalization factor is determined to be 1.77. No MC events from  $Z\gamma$  processes  
 818 survive the full event selection; thus, the scaling is only applied to the  $W\gamma$  background in the signal  
 819 region. A systematic uncertainty of 44% is assigned to the background based off of the uncertainties  
 820 in the calculation of the normalization factor.

Event yields in the $V\gamma$ control region	
$Z\gamma$	$24.6 \pm 3.3$
$Z+jets$	$3.0 \pm 1.5$
diboson + triboson	$6.7 \pm 0.3$
top	$1.5 \pm 0.5$
Total prediction	$35.8 \pm 3.7$
Data	$57 \pm 7.6$

Table 5.11: Event yields in the  $V\gamma$  control region. The  $V\gamma$  scale factor of 1.77 is calculated by scaling up the  $Z\gamma$  and  $Z+jets$  backgrounds to account for the difference between the data and predicted total background.

### 821 5.3.3 Estimation of backgrounds from charge misidentification

822 If an electron's charge is mis-reconstructed, it can lead to a real, opposite-sign lepton pair passing  
 823 the same-sign requirement in the event selection. There are two primary reasons this can occur:

- 824 1. An electron emits a photon via bremsstrahlung which then converts into an electron-positron  
 825 pair, and the conversion track with the wrong electric charge is matched to the original electron.  
 826 This is the dominant process leading to charge flip, and it is highly dependent on the electron  
 827  $\eta$  due to the different amount of detector material the electron passes through.
- 828 2. The curvature of the electron's track is mismeasured, resulting in the wrong charge being  
 829 assigned. This process is dependent on the momentum of the electron, as its track becomes  
 830 more straight as the momentum of the electron increases.

831 In order to estimate this background, the rate at which an electron's charge is misidentified is  
 832 calculated from  $Z \rightarrow e^+e^-$  MC simulation. It is known that the MC does not perfectly model

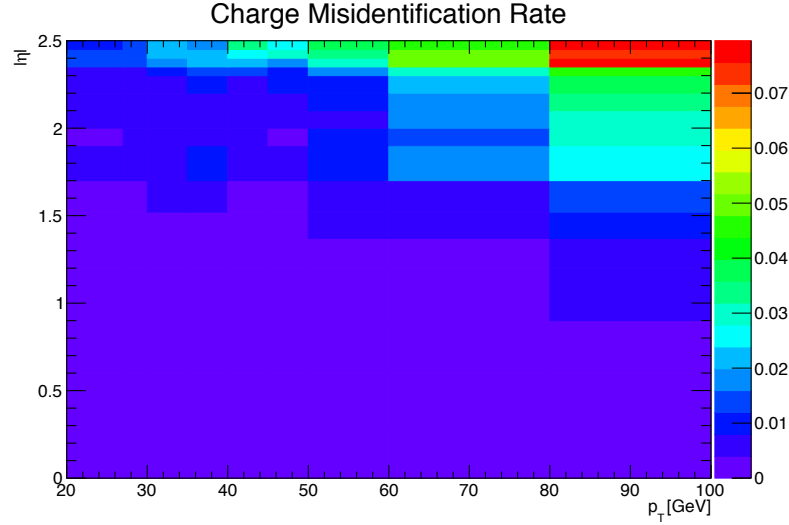


Figure 5.11: Charge misidentification rates for electrons as a function of  $|\eta|$  and  $p_T$ . Rates are calculated from  $Z \rightarrow e^+e^-$  MC after applying scale factors to approximate the charge mis-ID rates in data.

the material effects leading to charge flip; as a result, scale factors are applied to the MC in order for it to better reflect the real performance. These scale factors are obtained from the ratio of charge mis-ID rates in data and uncorrected MC in [17] following the method outlined in [51]. Once the scale factors are applied, the charge misidentification rate  $\varepsilon$  can be extracted by comparing the electron’s reconstructed charge with the charge of its truth particle:

$$\varepsilon(\eta, p_T) = \frac{N_{\text{wrong charge}}}{N_{\text{prompt electrons}}} \quad (5.1)$$

The charge mis-ID rate is calculated in bins of electron  $|\eta|$  and  $p_T$  and varies from below 0.1% in the

central region of the detector up to 8% in the forward regions for high  $p_T$  (above 90 GeV) electrons.

A two-dimensional plot of  $\varepsilon$  can be found in Figure 5.11.

Given the charge flip rate  $\varepsilon(\eta, p_T)$ , the rate at which an electron has its charge correctly reconstructed is  $(1 - \varepsilon)$ . Thus there are three possible combinations of charge identification, assuming a two-electron event:

- 844 1. Both electrons are reconstructed correctly:  $(1 - \varepsilon)^2$
- 845 2. Both electrons are mis-reconstructed:  $\varepsilon^2$
- 846 3. Only one electron is mis-reconstructed:  $2\varepsilon(1 - \varepsilon)$

847 In order to estimate the size of the background from charge misidentification, opposite-sign events  
 848 are selected using the default event selection for a given signal or control region with the same-sign  
 849 requirement inverted. These events are then weighted by the probability for one of the electrons to  
 850 be reconstructed with the wrong charge:

$$\omega = \frac{\varepsilon_1(1 - \varepsilon_2) + \varepsilon_2(1 - \varepsilon_1)}{(1 - \varepsilon_1)(1 - \varepsilon_2) + \varepsilon_1\varepsilon_2} \quad (5.2)$$

851 where the subscripts 1 and 2 refer to the leading and subleading electrons, respectively, and  $\varepsilon_i$  is a  
 852 function of the  $\eta$  and  $p_T$  of the  $i^{\text{th}}$  electron. In the case of an event with only one electron and one  
 853 muon, Equation 5.2 simplifies:

$$\omega = \frac{\varepsilon}{1 - \varepsilon} \quad (5.3)$$

854 This method assumes that there is little contamination from fake electrons in the opposite-sign  
 855 sample, and this has been verified with MC simulation.

856 Additionally, charge-flipped electrons tend to be reconstructed with lower energy when compared  
 857 to electrons with the correct charge. This is due to energy loss from the material interactions that  
 858 can cause the charge to be misidentified. A correction factor is calculated from MC simulations,  
 859 comparing the  $p_T$  of the truth electron to its reconstructed counterpart:

$$\alpha = \frac{\left(\frac{p_T^{\text{reco}}}{p_T^{\text{truth}}} - 1\right)_{\text{correct charge}}}{\left(\frac{p_T^{\text{reco}}}{p_T^{\text{truth}}} - 1\right)_{\text{wrong charge}}} \quad (5.4)$$

860 The correction is then applied to the  $p_T$  of the charge-flipped electron via

$$p_T = p_T^0 / (1 + \alpha) + dE \quad (5.5)$$

861 where  $p_T^0$  is the uncorrected  $p_T$  of the electron and  $dE$  is a gaussian smearing factor centered at  
 862 zero with a width related to the energy resolution. Since which electron is misreconstructed is never  
 863 determined in this method, in the case of a two-electron event, the energy correction is applied  
 864 randomly to one of the two electrons based on the probabilities for them to be charge-flipped. This  
 865 also determines the overall sign of the event; the charge of the electron that does not receive the  
 866 correction is taken to be the charge for both.

867 Systematic uncertainties on the charge mis-ID rates are calculated by generating two additional  
 868 sets of rates with the uncertainties on the scale factors varied up and down. The size of the esti-  
 869 mated charge flip background without the energy correction applied is also taken as a systematic  
 870 uncertainty. These systematic uncertainties are estimated to be approximately  $\pm 15\%$ .

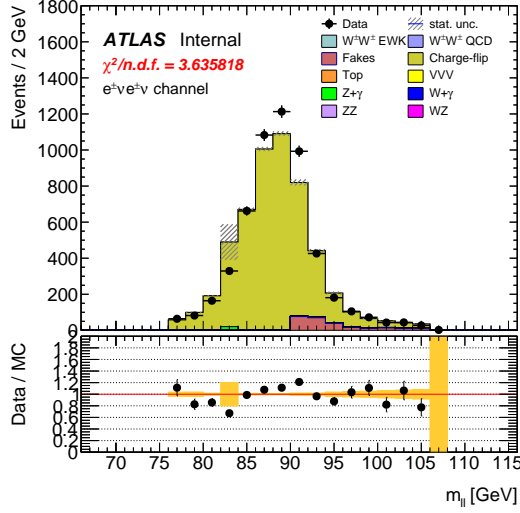


Figure 5.12: Dilepton invariant mass distribution  $m_{ll}$  for the  $ee$  channel in the same-sign inclusive VR.

### 871 5.3.3.1 Validation of the charge misidentification estimate

872 The performance of the charge misidentification estimation is tested in the same-sign inclusive  
 873 validation region (VR), defined in Table 5.12. For  $ee$  events, the mass of the dilepton pair is required  
 874 to lie within 15 GeV of the  $Z$  boson mass to increase the purity of the charge flip background.  
 875  $t\bar{t}$  production, which can contribute to both the charge mis-ID and fake lepton backgrounds, is  
 876 suppressed by the  $b$ -jet veto. The di-electron invariant mass is shown in Figure 5.12, and distributions  
 877 of the leading and subleading electron  $p_T$  in the  $ee$ -channel are shown in Figure 5.13 with the  $Z$   
 878 mass cut inverted. Agreement between data and prediction is seen within the total statistical and  
 879 systematic uncertainties in the VR.

Same-sign inclusive VR
Exactly 2 same-sign signal leptons
$p_T > 27$ GeV for both leptons
$m_{ll} > 20$ GeV
$ m_{ee} - m_Z  > 15$ GeV ( $e^\pm e^\pm$ -channel only)
$N_{b\text{-jet}} = 0$

Table 5.12: Selection criteria for the same-sign inclusive validation region.

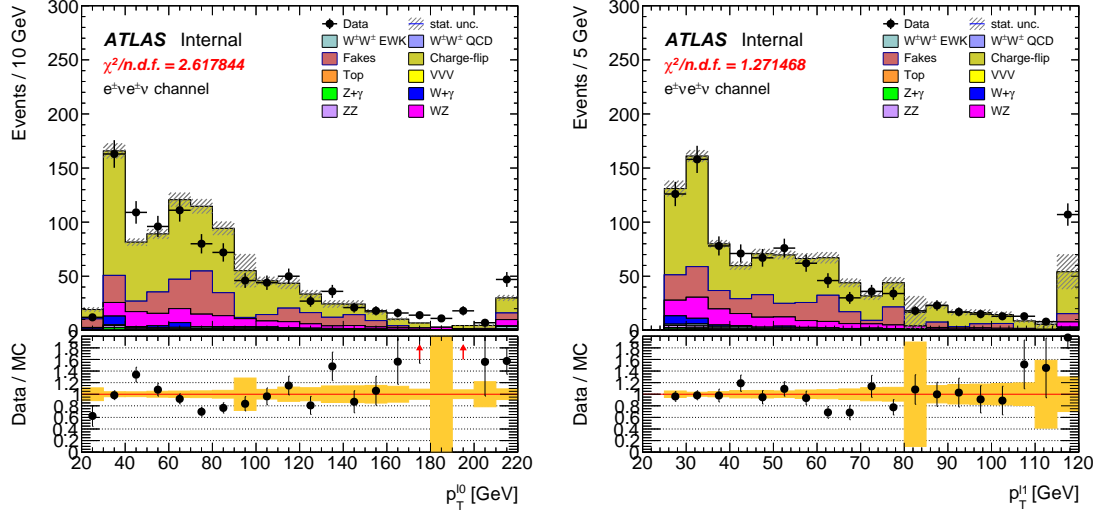


Figure 5.13:  $p_T$  distributions for the leading (left) and subleading (right) electron for the  $ee$  channel in the same-sign inclusive VR. In these plots, the cut requiring  $m_{ee}$  to fall within the  $Z$  mass window has been inverted in order to test the modelling away from the  $Z$  peak.

#### 880 5.3.4 Estimation of non-prompt backgrounds with the fake factor method

881 Events with one prompt lepton produced in association with hadronic jets can pass the event selection  
 882 if a jet is misidentified as a charged lepton or if a non-prompt lepton from the decay of a heavy  
 883 flavor particle (such as  $b$ - and  $c$ -hadrons) passes the signal lepton criteria. These misidentified jets  
 884 and non-prompt leptons are collectively referred to as *fake leptons*, or simply *fakes*. The rate at  
 885 which a fake lepton is misidentified is generally not modelled well enough by the MC to accurately  
 886 estimate their contributions directly from simulation. Therefore, a data-driven technique called the  
 887 *fake factor* is used to estimate the size and shape of background processes from fake leptons. In this  
 888 analysis, a new modification to the fake factor is used involving the particle isolation variables; the  
 889 method is outlined in the context of the *default* fake factor in Section 5.3.4.1, and the modified fake  
 890 factor is outlined in Section 5.3.4.2.

##### 891 5.3.4.1 Overview of the default fake factor method

892 The goal of the fake factor method is to measure the fake rate from real collision events in a region  
 893 enriched in fake leptons and use it to estimate the size of the fake lepton background in a chosen  
 894 signal or control region. This is done by creating two samples using different lepton definitions:

- 895 1. The *nominal* sample is made up of leptons passing the signal selection.

896     2. The *loose* sample is made up of leptons that fail the signal selection while still passing a  
 897        loosened set of criteria. This sample is enriched in fake leptons and is orthogonal to the set of  
 898        signal leptons.

899     Using the sets of nominal and loose leptons, a fake factor  $f$  can be calculated in a region enriched  
 900        in processes that are prone to producing fake leptons:

$$f = \frac{N_{\text{nominal}}}{N_{\text{loose}}} \quad (5.6)$$

901     Since the fake rate is not expected to be constant over the entire phase space, the fake factor can  
 902        be divided into bins:

$$f(b) = \frac{N_{\text{nominal}}(b)}{N_{\text{loose}}(b)} \quad (5.7)$$

903     where  $b$  represents the bin number. In this analysis, the fake factor is binned in lepton  $p_T$ .

904     In order to estimate the fake background contribution in a given signal or control region, the  
 905        fake factor is applied to a second control region with a selection identical to the region of interest  
 906        with one of the leptons required to satisfy the loose criteria. The region for which the background  
 907        is estimated contains two nominal leptons and is referred to as *nominal+nominal* ( $NN$ ), and the  
 908        associated control region where the fake factor is applied contains one nominal and one loose lepton  
 909        and is referred to as *nominal+loose* ( $NL$ ). The fake background in a  $NN$  region can then be  
 910        calculated as:

$$N_{NN}^{\text{fake bkg.}} = \sum_b f(b) N_{NL}(b) \quad (5.8)$$

911     Backgrounds containing two prompt leptons can also enter the  $NL$  region if one of the leptons  
 912        passes the nominal selection and the other passes the loose selection. Since the fake factor method  
 913        estimates the fake background by scaling the amount of non-prompt events in the  $NL$  region, if these  
 914        prompt contributions are not removed, they will be included in the scaling and the background  
 915        will be overpredicted. The final estimate of the fake background becomes:

$$N_{NN}^{\text{fake bkg.}} = \sum_b f(b) (N_{NL}(b) - N_{NL}^{\text{prompt}}(b)) \quad (5.9)$$

916     **5.3.4.2 The fake factor with  $p_T^{\text{cone}}$**

917     When a jet produces a non-prompt lepton, that lepton only carries a fraction of the underlying jet's  
 918        total momentum. Due to the isolation cut applied to the nominal leptons, they typically carry a

919 much larger percentage of the underlying jet momentum<sup>9</sup> than the loose leptons (which are allowed  
 920 to fail this criteria).

921 This discrepancy in the underlying jet momentum fraction can cause problems in the calculation  
 922 of the fake factor  $f$ . Consider the case where two separate events have jets of identical momentum,  
 923 but one produces a non-prompt lepton that passes the nominal selection, and the other produces a  
 924 non-prompt lepton that passes the loose selection. The loose lepton on average will have lower  $p_T$   
 925 than the nominal lepton despite both originating from jets with the same momentum. This can be  
 926 seen explicitly when comparing the  $p_T$  of a muon to its associated truth jet:

$$\Delta p_T(\mu, j) = \frac{p_T(j) - p_T(\mu)}{p_T(j) + p_T(\mu)} \quad (5.10)$$

927 Since muons are not included in the jet reconstruction algorithm,  $\Delta p_T$  approximates the momentum  
 928 of the muon compared to the rest of the jet. For muons that carry more than 50% of the jet's  
 929 momentum,  $\Delta p_T$  will be negative and vice-versa. The  $\Delta p_T$  distributions for nominal and loose  
 930 muons in  $t\bar{t}$  MC events is shown Figure 5.14, where a 50 GeV jet on average corresponds to a  
 931 35 GeV nominal muon and a 20 GeV loose muon<sup>10</sup>.

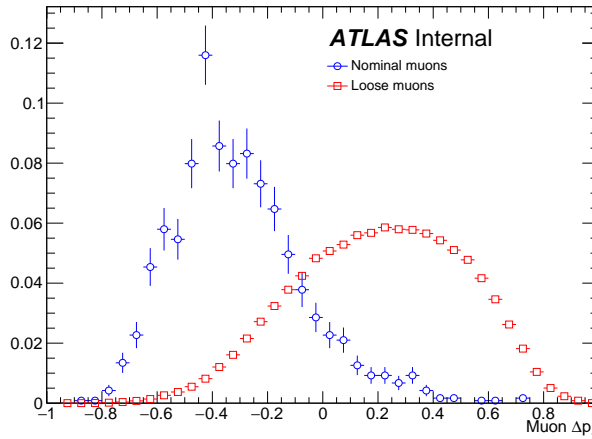


Figure 5.14:  $\Delta p_T$  distributions for nominal (blue) and loose (red) muons in simulated  $t\bar{t}$  events. Each muon has been matched to a truth-level jet. Both distributions are normalized to unit area.

932 Since the default fake factor defined in Equation 5.7 is binned in lepton  $p_T$ , within a given bin,

<sup>9</sup>Since the isolation variables are a measure of detector activity around the lepton, if other nearby particles carried a significant portion of the jet's momentum, the lepton would likely fail this cut.

<sup>10</sup>To better illustrate the point, here the muon is added back into the jet  $p_T$ , and the corresponding muon  $p_T$  is obtained via  $\Delta p_T(\mu, j) = \frac{(p_T(j) - p_T\mu) - p_T(\mu)}{(p_T(j) - p_T\mu) + p_T(\mu)} = \frac{p_T(j) - 2p_T(\mu)}{p_T(j)}$ .

the underlying jet  $p_T$  spectrum can differ substantially between the numerator and the denominator. Additionally, these differences can vary depending on the process producing the non-prompt leptons or on the specific kinematic selections of the signal or control regions where the fake factor is applied.

Fortunately, the majority of the jet momentum not carried by the non-prompt lepton (excluding neutrinos) can be recovered using isolation variables. A track-based isolation is chosen, referred to as  $p_T^{\text{cone}}$ , and it contains the sum of the  $p_T$  of all particle tracks originating from the primary vertex within a cone of  $\Delta R < 0.3$  around the lepton. Thus, the sample of loose leptons in the denominator of the fake factor calculation is binned in  $p_T + p_T^{\text{cone}}$  rather than simply lepton  $p_T$ . Adding the isolation cone greatly reduces the difference in the fraction of the underlying jet momentum carried by the nominal and loose leptons. To check this, a new  $\Delta p_T$  is calculated between a lepton and its matched truth jet, where the truth jet  $p_T$  has been corrected to include all muons within a cone of  $\Delta R < 0.4$ :

$$p_T(j) = p_T(j_{\text{truth}}) + \sum_{\Delta R < 0.4} p_T(\mu_{\text{truth}}) \quad (5.11)$$

The  $\Delta p_T$  distributions comparing  $p_T$  and  $p_T + p_T^{\text{cone}}$  for nominal and loose leptons using the corrected jet  $p_T$  are found in Figure 5.15, and better agreement is seen between the numerator (nominal) and denominator (loose with  $p_T + p_T^{\text{cone}}$ ) distributions.

The numerator remains binned in lepton  $p_T$ , due to the fact that it is meant to mirror the signal region as closely as possible, and the signal lepton selection does not use  $p_T + p_T^{\text{cone}}$ . The impact of this is expected to be negligible due to the  $p_T^{\text{cone}}$  isolation being small for signal leptons, as shown for muons in Figure 5.16. Finally, the fake factor  $f$  becomes:

$$f(b) = \frac{N_{\text{nominal}}(b(p_T))}{N_{\text{loose}}(b(p_T + p_T^{\text{cone}}))} \quad (5.12)$$

#### 5.3.4.3 Application of the fake factor

The fake factor itself is measured from a sample data events passing a dijet selection requiring exactly one lepton (either passing the nominal or loose selections) and at least one jet. The leading jet must also be  $b$ -tagged and approximately back-to-back with the lepton in order to enhance non-prompt lepton contributions while reducing contributions from processes involving  $W$  and  $Z$  bosons.  $W$  boson events are further suppressed by requiring the sum of the  $E_T^{\text{miss}}$  and the transverse mass of the lepton and  $E_T^{\text{miss}}$  to be less than 50 GeV. The full event selection for the dijet region is summarized in Table 5.13.

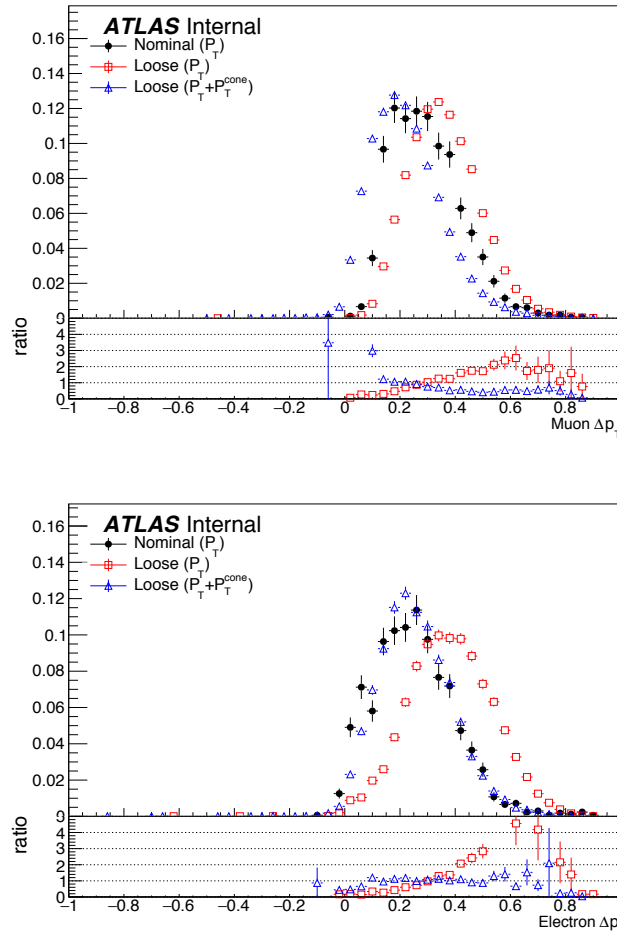


Figure 5.15:  $\Delta p_T$  distributions for muons (top) and electrons (bottom) in simulated  $t\bar{t}$  events. Each lepton has been matched to a truth-level jet, and that truth jet has had its  $p_T$  corrected to include all truth muons within a cone of  $\Delta R < 0.4$ . The nominal leptons are in black.  $\Delta p_T$  is calculated for the loose leptons using  $p_T$  (red) and  $p_T + p_T^{\text{cone}}$  (blue).

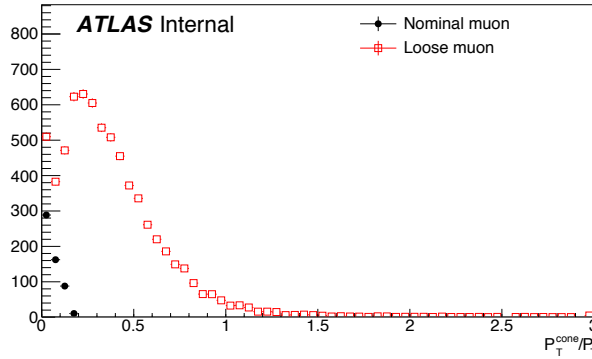


Figure 5.16: Distributions of  $p_T^{\text{cone}}/p_T$  for nominal (black) and loose (red) muons in simulated  $t\bar{t}$  events.

Dijet event selection	
Event preselection	
Exactly one lepton with $p_T > 15$ GeV	
$N_{\text{jet}} > 0$	
Leading jet is $b$ -tagged	
$p_T^{\text{lead. jet}} > 25$ GeV	
$p_T^{\text{lead. jet}} > 30$ GeV if $ \eta_j  > 2.5$	
$ \Delta\phi(l, \text{lead. jet})  > 2.8$	
$m_T(l, E_T^{\text{miss}}) + E_T^{\text{miss}} < 50$ GeV	

Table 5.13: Event selection for the dijet region used for calculating the fake factor. The selected lepton can pass either the nominal (signal) or loose selections. In the case of the nominal leptons, the  $p_T > 27$  GeV requirement is replaced with  $p_T > 15$  GeV.

The numerator sample is constructed from dijet events in which the lepton passes the nominal selection and is binned in the lepton  $p_T$ . Similarly, the denominator sample is made up of the remaining dijet events where the lepton passes the loose selection and is binned in the lepton  $p_T + p_T^{\text{cone}}$ . The nominal and loose leptons pass the signal selection<sup>11</sup> and loose selection, respectively, defined earlier in Table 5.3 for muons and Table 5.4 for electrons. Backgrounds from  $W+\text{jets}$ ,  $Z+\text{jets}$ ,  $t\bar{t}$ , and single top processes are estimated from MC simulations requiring one lepton to be prompt using the truth information; these contributions are subtracted from the dijet data. The fake factor is then calculated using Equation 5.12 for muons and for central and forward electrons separately. The muon fake factor is shown in Figure 5.17, and the two electron fake factors are shown in Figure 5.18. The numerical values of the fake factors, including their systematic uncertainties which

<sup>11</sup>The  $p_T > 27$  GeV cut in the signal lepton selection is dropped in favor of the  $p_T > 15$  GeV requirement in the dijet selection.

970 will be discussed in Section 5.3.4.4, are listed in Table 5.14.

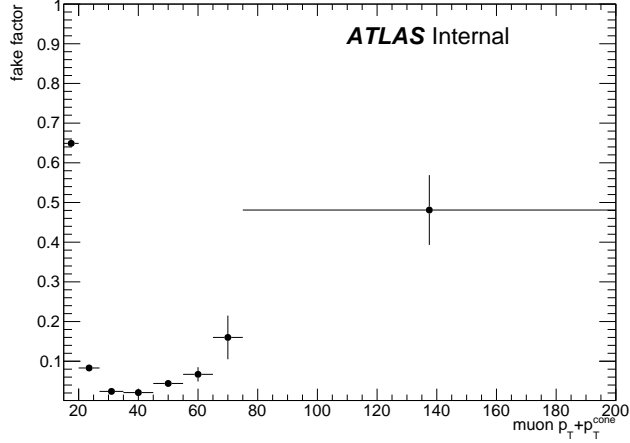


Figure 5.17: The measured fake factor as a function of muon  $p_T + p_T^{\text{cone}}$ . The error bars represent the statistical uncertainty only.

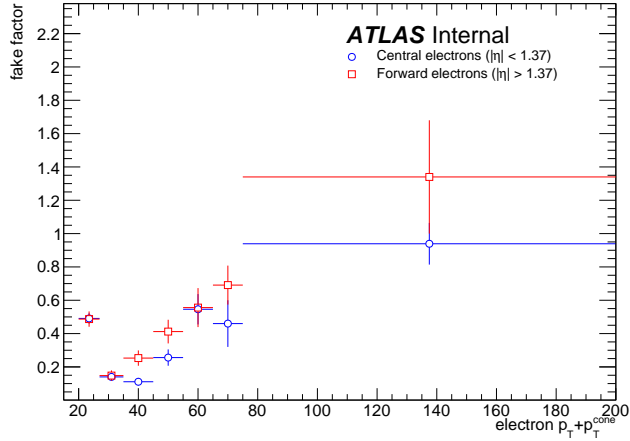


Figure 5.18: The measured fake factor as a function of electron  $p_T + p_T^{\text{cone}}$  in the central ( $|\eta| < 1.37$ , blue) and forward ( $|\eta| > 1.37$ , red) regions of the detector. The error bars represent the statistical uncertainty only.

971 In order to properly account for the denominator being binned in  $p_T + p_T^{\text{cone}}$ , special care needs  
 972 to be taken when estimating the fake background from the  $NL$  regions. For the purposes of the  
 973 fake factor calculation, it is perhaps more intuitive to consider a loose *object* with  $p_T = p_T + p_T^{\text{cone}}$   
 974 instead of simply a loose *lepton*, as the lepton and the underlying jet are treated as a whole with this

method. When the lepton  $p_T$  cuts required by a particular signal or control region are applied to nominal and loose leptons, the cut is applied to the  $p_T$  of the nominal lepton and to the  $p_T + p_T^{\text{cone}}$  of the loose object. Similarly, when looking up the fake factor weight for a given  $NL$  event, the value taken from the bin corresponding to the  $p_T + p_T^{\text{cone}}$  of the loose object. Finally, when applying the weight to the event,  $p_T + p_T^{\text{cone}}$  is assigned as the  $p_T$  of the loose object. Figure 5.19 contains a graphical representation of this procedure.

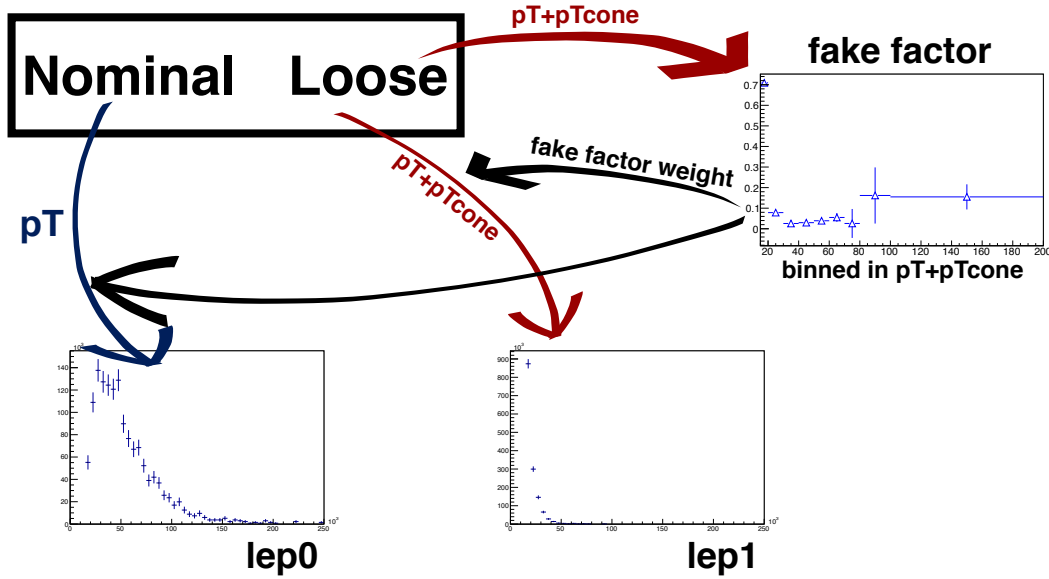


Figure 5.19: Graphical representation of the fake factor application using  $p_T + p_T^{\text{cone}}$ . The value of  $p_T + p_T^{\text{cone}}$  for the loose lepton is used to “look up” the fake factor weight which is then applied to the event. The loose lepton’s  $p_T$  becomes  $p_T + p_T^{\text{cone}}$  for the purpose of the fake background estimation.

Finally, it should be noted that the addition of  $p_T^{\text{cone}}$  to the loose object may cause the loose leptons in the denominator sample to migrate into higher bins. This results in an overall decrease in the number of loose objects in the lower  $p_T + p_T^{\text{cone}}$  bins due to there not being additional leptons at lower  $p_T$  to replace them. Since the fake factor is a ratio of the number of events in a bin, this effect causes the first few bins of the fake factor to increase, as can be seen clearly in Figure 5.17. However, the signal and control regions (and their corresponding  $NL$  regions) contain a  $p_T > 27$  GeV cut that prevents these migrations from negatively impacting the fake estimation.

988 **5.3.4.4 Systematic uncertainties**

989 Four sources of systematic uncertainty are considered: the dijet event selection, the prompt back-  
 990 ground subtraction, the jet flavor composition, and residual dependence on the underlying jet  $p_T$   
 991 spectrum. In order to measure the impact of these systematics, new fake factors are computed  
 992 with each of the systematic variations and the differences from the nominal values are taken as the  
 993 uncertainty.

- 994    1. In order to estimate uncertainties due to the dijet selection, the cut on  $M_T + MET$  is varied  
   995      by  $\pm 5$  GeV,  $\Delta\phi(l, j)$  by  $\pm 0.1$ , and the jet  $p_T$  cut by  $+5$  GeV.
- 996    2. To estimate the systematic uncertainty on the prompt background subtraction, the MC pre-  
   997      dictions in a  $W+jets$  control region is compared to data. The discrepancy between data and  
   998      MC is found to be approximately 10% [17]. Therefore, the prompt background used for the  
   999      subtraction is scaled up and down by  $\pm 10\%$ .
- 1000    3. The difference in the jet flavor composition between the dijet events and the events in the  
   1001       $NL$  regions can affect the accuracy of the fake background estimation. The dijet sample is  
   1002      dominated by light jets, while the  $NL$  regions tend to be dominated by heavy flavor from  $t\bar{t}$ .  
   1003      To account for this, the fake factor is computed with a  $b$ -jet veto.
- 1004    4. To measure any residual dependence on the underlying jet  $p_T$  spectrum, the leading jet  $p_T$   
   1005      distribution is reweighted to match the  $p_T$  spectrum of truth jets that produce fake leptons  
   1006      in MC simulations. This results in an increase in the number of nominal and loose leptons at  
   1007      high momentum [17].

1008 **5.3.4.5 Results of the fake factor**

1009 The fake background contribution in the signal region is estimated by applying the fake factors  
 1010 to the equivalent  $NL$  region using Equation 5.9, where the fake factor used corresponds to the  
 1011 flavor of the loose lepton in the event. As usual, the prompt background is subtracted from the  
 1012  $NL$  events using MC simulation. Charge misidentification is handled using the same method as  
 1013 in Section 5.3.3, with an additional set of charge flip rates calculated for loose leptons. The fake  
 1014 background yields in the signal region are listed in Table 5.15. An overall uncertainty of 50% is  
 1015 assigned to the fake background estimation in  $\mu^\pm\mu^\pm$  events, and between 40% to 90% for  $e^\pm e^\pm$  and  
 1016  $\mu^\pm e^\pm$  events, including both statistical and systematic effects.

fake factor	$p_T[15, 20]$	$p_T[20, 27]$	$p_T[27, 35]$	$p_T[35, 45]$	$p_T[45, 55]$	$p_T[55, 65]$	$p_T[65, 75]$	$p_T[75, 200]$
nominal	$0.649 \pm 0.007$	$0.083 \pm 0.002$	$0.024 \pm 0.002$	$0.021 \pm 0.003$	$0.044 \pm 0.007$	$0.067 \pm 0.018$	$0.160 \pm 0.055$	$0.481 \pm 0.088$
MT+MET	$0.649 \pm 0.007$	$0.082 \pm 0.002$	$0.082 \pm 0.002$	$0.020 \pm 0.003$	$0.045 \pm 0.007$	$0.068 \pm 0.018$	$0.207 \pm 0.062$	$0.523 \pm 0.086$
$\Delta\phi(\ell, j)$	$0.645 \pm 0.008$	$0.083 \pm 0.003$	$0.024 \pm 0.002$	$0.021 \pm 0.004$	$0.045 \pm 0.008$	$0.064 \pm 0.021$	$0.064 \pm 0.058$	$0.438 \pm 0.092$
Jet $p_T$	$0.650 \pm 0.007$	$0.083 \pm 0.002$	$0.024 \pm 0.002$	$0.021 \pm 0.003$	$0.045 \pm 0.007$	$0.069 \pm 0.018$	$0.159 \pm 0.018$	$0.481 \pm 0.088$
$N_{b\text{-jet}} = 0$	$0.724 \pm 0.003$	$0.094 \pm 0.001$	$0.035 \pm 0.001$	$0.025 \pm 0.002$	$0.022 \pm 0.004$	$0.060 \pm 0.015$	$0.026 \pm 0.053$	$0.044 \pm 0.134$
Bkg. subtraction	$0.648 \pm 0.007$	$0.083 \pm 0.002$	$0.024 \pm 0.002$	$0.019 \pm 0.003$	$0.037 \pm 0.007$	$0.044 \pm 0.019$	$0.096 \pm 0.062$	$0.370 \pm 0.082$
Jet $p_T$ Reweighting	$0.649 \pm 0.007$	$0.083 \pm 0.002$	$0.025 \pm 0.002$	$0.022 \pm 0.003$	$0.050 \pm 0.007$	$0.090 \pm 0.017$	$0.224 \pm 0.052$	$0.591 \pm 0.099$
	$0.539 \pm 0.077$	$0.093 \pm 0.007$	$0.025 \pm 0.004$	$0.043 \pm 0.019$	$0.063 \pm 0.014$	$0.085 \pm 0.025$	$0.141 \pm 0.110$	$1.962 \pm 0.492$

(a) Fake factor for muons.

fake factor	$p_T[20, 27]$	$p_T[27, 35]$	$p_T[35, 45]$	$p_T[45, 55]$	$p_T[55, 65]$	$p_T[65, 75]$	$p_T[75, 200]$
nominal	$0.491 \pm 0.031$	$0.140 \pm 0.020$	$0.111 \pm 0.023$	$0.256 \pm 0.049$	$0.546 \pm 0.091$	$0.460 \pm 0.140$	$0.939 \pm 0.125$
MT+MET	$0.493 \pm 0.030$	$0.138 \pm 0.019$	$0.115 \pm 0.022$	$0.261 \pm 0.045$	$0.559 \pm 0.084$	$0.656 \pm 0.091$	$0.802 \pm 0.016$
$\Delta\phi(\ell, j)$	$0.488 \pm 0.032$	$0.137 \pm 0.020$	$0.110 \pm 0.025$	$0.283 \pm 0.053$	$0.503 \pm 0.097$	$0.351 \pm 0.149$	$1.117 \pm 0.255$
Jet $p_T$	$0.489 \pm 0.035$	$0.134 \pm 0.021$	$0.105 \pm 0.025$	$0.224 \pm 0.048$	$0.593 \pm 0.093$	$0.356 \pm 0.144$	$0.928 \pm 0.177$
$N_{b\text{-jet}} = 0$	$0.506 \pm 0.029$	$0.140 \pm 0.018$	$0.111 \pm 0.022$	$0.260 \pm 0.046$	$0.545 \pm 0.084$	$0.546 \pm 0.120$	$0.882 \pm 0.103$
Jet $p_T$	$0.493 \pm 0.032$	$0.146 \pm 0.021$	$0.115 \pm 0.024$	$0.259 \pm 0.049$	$0.550 \pm 0.091$	$0.460 \pm 0.140$	$0.939 \pm 0.125$
$N_{b\text{-jet}} = 0$	$0.387 \pm 0.009$	$0.130 \pm 0.008$	$0.321 \pm 0.012$	$0.473 \pm 0.015$	$0.716 \pm 0.180$	$0.716 \pm 0.180$	$0.716 \pm 0.180$
Bkg. subtraction	$0.488 \pm 0.031$	$0.138 \pm 0.020$	$0.106 \pm 0.023$	$0.248 \pm 0.049$	$0.529 \pm 0.092$	$0.434 \pm 0.143$	$0.888 \pm 0.115$
Jet $p_T$ Reweighting	$0.493 \pm 0.031$	$0.142 \pm 0.020$	$0.115 \pm 0.023$	$0.264 \pm 0.049$	$0.563 \pm 0.090$	$0.485 \pm 0.136$	$0.989 \pm 0.132$
	$0.445 \pm 0.055$	$0.137 \pm 0.037$	$0.065 \pm 0.023$	$0.115 \pm 0.033$	$0.603 \pm 0.047$	$0.104 \pm 0.105$	$0.299 \pm 0.260$

(b) Fake factor for central electrons ( $|\eta| < 1.37$ ).

fake factor	$p_T[20, 27]$	$p_T[27, 35]$	$p_T[35, 45]$	$p_T[45, 55]$	$p_T[55, 65]$	$p_T[65, 75]$	$p_T[75, 200]$
nominal	$0.487 \pm 0.046$	$0.148 \pm 0.031$	$0.253 \pm 0.046$	$0.412 \pm 0.071$	$0.556 \pm 0.117$	$0.691 \pm 0.117$	$1.340 \pm 0.340$
MT+MET	$0.483 \pm 0.045$	$0.152 \pm 0.031$	$0.241 \pm 0.043$	$0.443 \pm 0.070$	$0.565 \pm 0.106$	$0.668 \pm 0.117$	$1.075 \pm 0.189$
$\Delta\phi(\ell, j)$	$0.495 \pm 0.047$	$0.156 \pm 0.033$	$0.271 \pm 0.052$	$0.364 \pm 0.074$	$0.664 \pm 0.107$	$0.749 \pm 0.056$	$0.885 \pm 0.084$
Jet $p_T$	$0.471 \pm 0.051$	$0.158 \pm 0.035$	$0.247 \pm 0.051$	$0.474 \pm 0.085$	$0.283 \pm 0.107$	$0.546 \pm 0.149$	$1.189 \pm 0.266$
$N_{b\text{-jet}} = 0$	$0.478 \pm 0.042$	$0.170 \pm 0.031$	$0.274 \pm 0.046$	$0.389 \pm 0.066$	$0.645 \pm 0.104$	$0.757 \pm 0.102$	$1.319 \pm 0.326$
Jet $p_T$	$0.523 \pm 0.048$	$0.149 \pm 0.033$	$0.235 \pm 0.045$	$0.429 \pm 0.073$	$0.555 \pm 0.117$	$0.691 \pm 0.117$	$1.340 \pm 0.340$
$N_{b\text{-jet}} = 0$	$0.525 \pm 0.011$	$0.234 \pm 0.013$	$0.644 \pm 0.016$	$0.710 \pm 0.014$	$0.274 \pm 0.316$	$0.274 \pm 0.316$	$0.274 \pm 0.316$
Bkg. subtraction	$0.484 \pm 0.046$	$0.146 \pm 0.031$	$0.248 \pm 0.046$	$0.406 \pm 0.071$	$0.545 \pm 0.118$	$0.676 \pm 0.118$	$1.317 \pm 0.337$
Jet $p_T$ Reweighting	$0.489 \pm 0.046$	$0.151 \pm 0.031$	$0.257 \pm 0.046$	$0.419 \pm 0.071$	$0.568 \pm 0.117$	$0.705 \pm 0.115$	$1.363 \pm 0.342$
	$0.328 \pm 0.068$	$0.124 \pm 0.048$	$0.297 \pm 0.100$	$0.234 \pm 0.061$	$0.680 \pm 0.092$	$0.452 \pm 0.138$	$2.385 \pm 1.729$

(c) Fake factor for forward electrons ( $1.37 < |\eta|$ ).Table 5.14: Values of the fake factor in each  $p_T$  bin and for each individual systematic source.

	estimated yield	$f_e$ stat. up	$f_e$ stat. dn	$f_e$ syst. up	$f_e$ syst. dn	$f_\mu$ stat. up	$f_\mu$ stat. dn	$f_\mu$ syst. up	$f_\mu$ syst. dn
$e^\pm e^\pm$	$11.42 \pm 3.13$	—	—	—	—	—	—	—	—
$\mu^\pm \mu^\pm$	$4.82 \pm 0.77$	—	—	—	—	$0.65$	$-0.65$	$3.64$	$-0.61$
$\mu^\pm e^\pm$	$37.08 \pm 5.16$	$4.90$	$-4.90$	$5.59$	$-14.34$	$1.39$	$-1.39$	$16.10$	$-1.98$

Table 5.15: Estimated yields for the fake lepton background. The estimated yield is shown in the first column together with the statistical uncertainty followed by the systematic uncertainties from variations of the the fake factors within their statistical (stat.) and systematic (syst.) uncertainties. The labels  $f_e$  and  $f_\mu$  indicate the fake factors for electrons and muons, respectively.

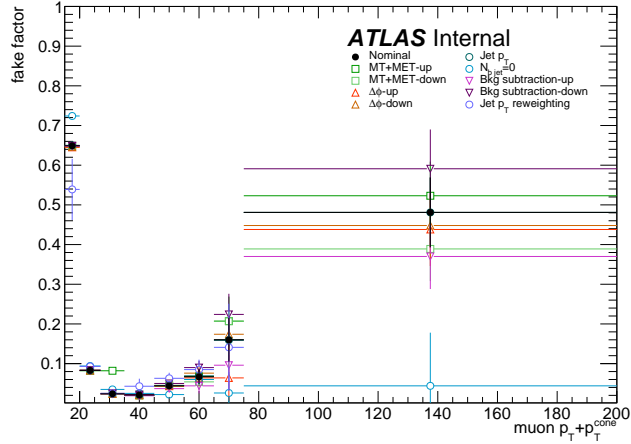


Figure 5.20: Systematic variations in the fake factor as a function of muon  $p_T + p_T^{\text{cone}}$ . The individual fake factors obtained for each systematic variation are displayed with their statistical uncertainties.

#### 1017 5.3.4.6 Validation of the fake factor

1018 The accuracy of the fake factor method is tested in several validation regions, the most sensitive  
 1019 of which is the same-sign top fakes VR (SS top VR), defined in Table 5.16. This region inverts  
 1020 the signal region's  $b$ -jet veto to accept events with exactly one  $b$ -jet. Due to this requirement, the  
 1021 dominant source of events comes from the  $t\bar{t}$  process where a  $b$ -jet fakes an isolated lepton. The  
 1022 distribution of the subleading lepton  $p_T$  in this VR is shown in Figure 5.22 for all lepton flavor  
 1023 combinations. There is good agreement between the data and the prediction, even when only taking  
 1024 into account the statistical uncertainty and not the large systematic uncertainties assigned to the  
 1025 fake estimation.

Same-sign inclusive VR
Exactly 2 same-sign signal leptons
$p_T > 27$ GeV for both leptons
$m_{ll} > 20$ GeV
$ m_{ee} - m_Z  > 15$ GeV ( $e^\pm e^\pm$ -channel only)
$N_{b\text{-jet}} = 1$
$N_{\text{jet}} \geq 2$
Leading jet $p_T > 65$ GeV
Subleading jet $p_T > 35$ GeV

Table 5.16: Selection criteria for the same-sign top fakes validation region.

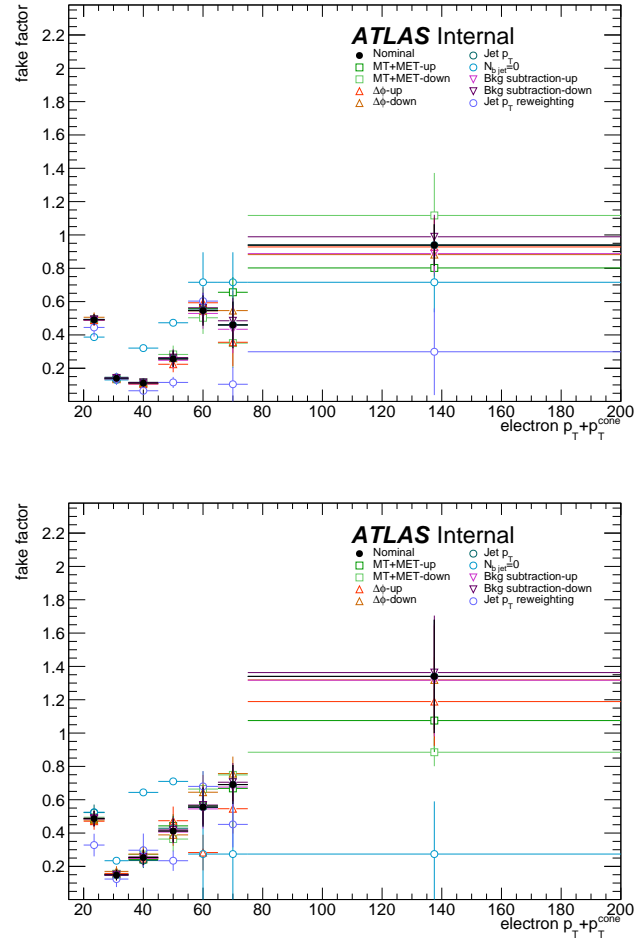


Figure 5.21: Systematic variations in the fake factor as a function of electron  $p_T + p_T^{\text{cone}}$  in the central ( $|\eta| < 1.37$ , top) and forward ( $|\eta| > 1.37$ , bottom) regions of the detector. The individual fake factors obtained for each systematic variation are displayed with their statistical uncertainties.

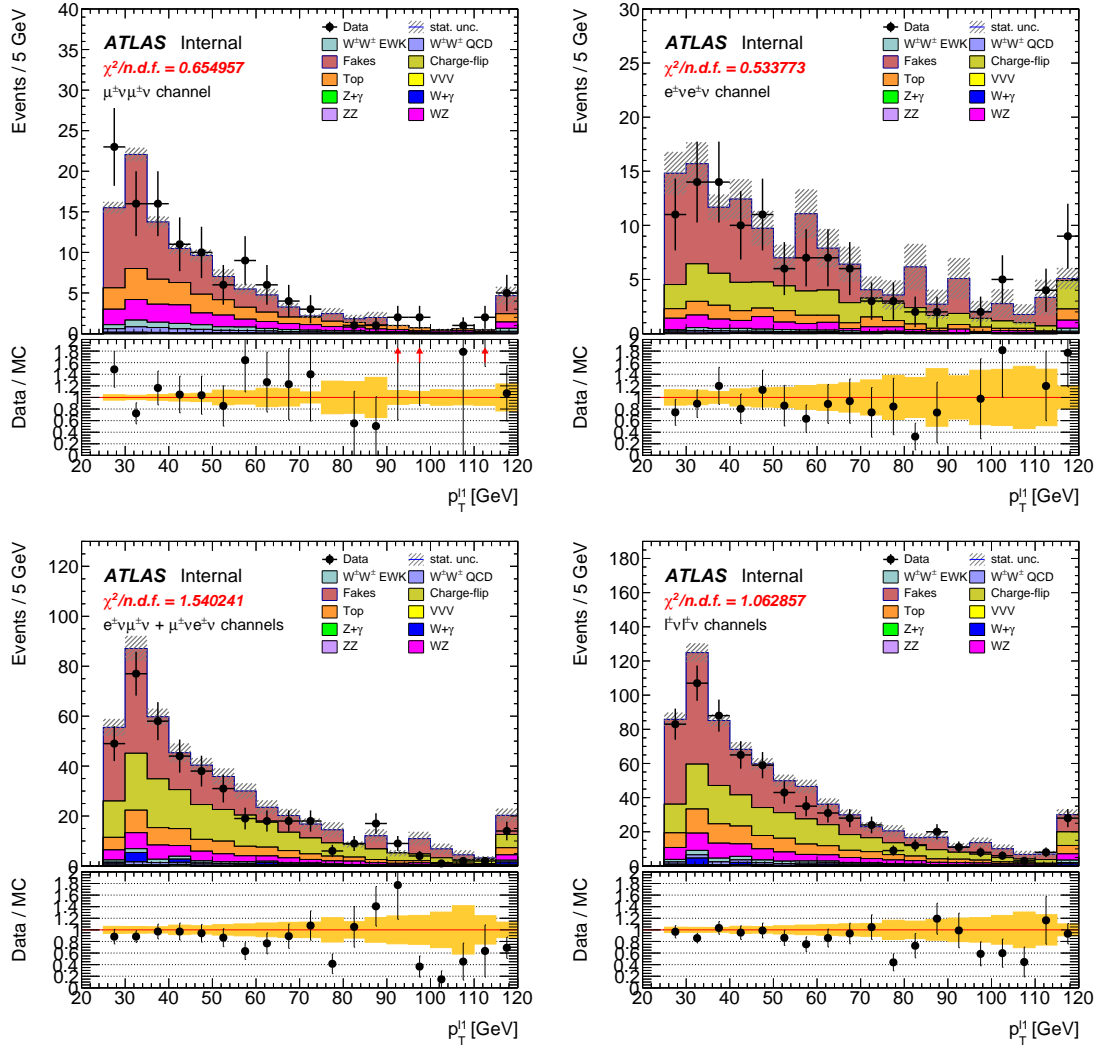


Figure 5.22: Distributions of the subleading lepton  $p_T$  in the same-sign top fakes VR for  $\mu^\pm\mu^\pm$  events (top right),  $e^\pm e^\pm$  events (top left),  $\mu^\pm e^\pm$  events (bottom left), and all events combined (bottom right). All errors are statistical only.

1026 **5.3.5 Reduction of  $WZ$  background using custom overlap removal**

1027 The dominant source of prompt background in this analysis comes from  $WZ$  events where both  
 1028 bosons decay leptonically. Traditionally, the background is dealt with by imposing a veto on any  
 1029 event with a third lepton passing some loose identification criteria (the so-called *trilepton veto*). In  
 1030 the case of this analysis, if one or more leptons (in addition to the two signal leptons) passed the  
 1031 preselection criteria, the event would be rejected. However,  $WZ$  events can still enter the signal  
 1032 region if one of the leptons fails the veto selection or falls outside of the detector’s acceptance.

1033 In order to understand the sources of  $WZ$  events that are not removed by the trilepton veto,  
 1034 a study was performed on truth-level leptons<sup>12</sup> on  $W^\pm W^\pm jj$  and  $WZ$  MC samples. Events with  
 1035 three truth leptons were selected, and each was matched to its reconstruction-level partner by finding  
 1036 the closest  $\Delta R(\text{truth}, \text{reco})$  and  $\Delta p_{\text{T},\text{truth},\text{reco}}$  match. For events surviving the trilepton veto, the  
 1037 two signal leptons were removed, and the remaining leptons represent real leptons that failed to  
 1038 be selected for the veto. Between 40-50% of these leptons fell outside of the eta acceptance of the  
 1039 analysis (see Figure 5.23) and were unrecoverable. The second largest source of leptons failing the  
 1040 preselection was the OR, defined in Section 5.2.1.4. The standard OR procedure appeared to be  
 1041 too aggressive in removing leptons in favor of jets, causing many three lepton events to “lose” their  
 1042 third lepton and pass the trilepton veto. Therefore a *Custom OR* was investigated which would  
 1043 replace the standard OR in the preselection and allow for better  $WZ$  rejection by removing fewer  
 1044 third leptons.

1045 **TODO:** Mention how the extra leptons in the  $W^\pm W^\pm jj$  are background leptons since there are  
 1046 only 2 from the main decay

1047 In order to construct a “custom” OR, a new quantity is defined between a lepton ( $l$ ) and a nearby  
 1048 jet ( $j$ )

$$p_{\text{T},\text{ratio}}(l, j) = \frac{p_{\text{T}l}}{p_{\text{T}j}} \quad (5.13)$$

1049 which, along with  $\Delta R(l, j)$ , will allow for more third leptons to pass the preselection. The idea  
 1050 behind including  $p_{\text{T},\text{ratio}}$  is to be able to preferentially remove background leptons originating from  
 1051 jets (i.e. those that carry a low percentage of the total jet momentum) instead of removing *any*  
 1052 lepton near to jet. The distributions of  $p_{\text{T},\text{ratio}}$  and the associated efficiency curves for muons and  
 1053 electrons can be found in Figures 5.24 and 5.26, respectively, and the distributions for  $\Delta R(\mu, j)$  for

---

<sup>12</sup>Truth particles are the particles produced directly by the MC generator before being passed through the full detector simulation, at which point they are considered *reconstruction-level* (or *reco-level*) particles.

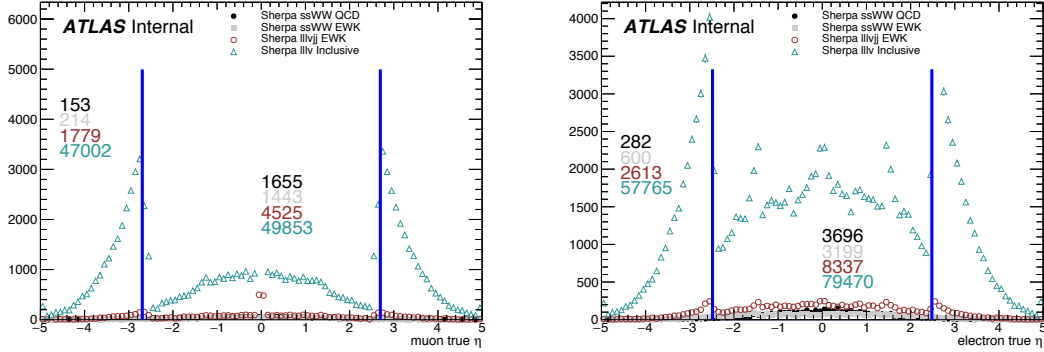


Figure 5.23: Pseudorapidity ( $\eta$ ) distributions of truth muons (top) and electrons (bottom) for Sherpa  $W^\pm W^\pm jj$  and  $WZ$  MC samples. The blue vertical lines represent the allowed  $\eta$  range for each lepton flavor. The numbers correspond to the number of raw MC events that fall within and outside of the allowed  $\eta$  range for each MC sample.

1054 muons can be found in Figure 5.25. Since all electrons have an associated jet in the calorimeters,  
1055 the  $\Delta R(e, j)$  variable is not a good quantity to use for this custom OR.

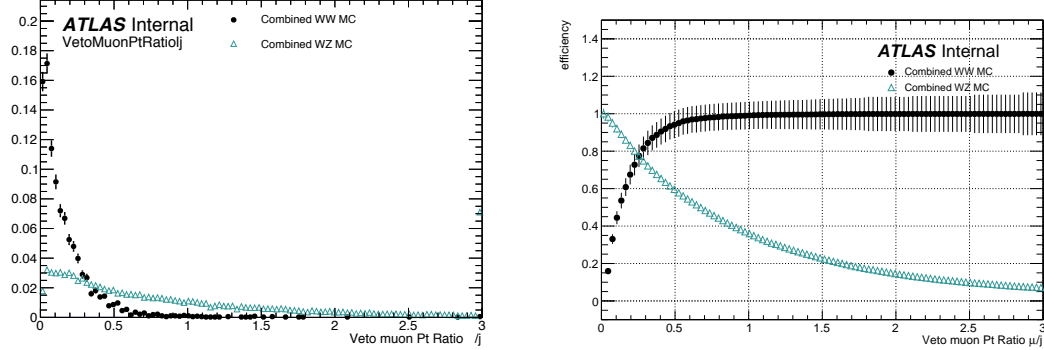


Figure 5.24: Distributions of  $p_{T,\text{ratio}}(\mu, j)$  for EWK and QCD  $W^\pm W^\pm jj$  signal (black) and  $WZ$  background (teal) for truth-matched third muons in events that pass the trilepton veto. Both distributions are normalized to unit area. The associated efficiency curves are on the right where efficiency is defined as the percentage of total events that would pass a cut on  $p_{T,\text{ratio}}(\mu, j)$  at a given value on the  $x$ -axis.

1056 A workingpoint for the Custom OR was chosen by requiring 90% signal retention for muons  
1057 and 90% background rejection for electrons. The cut on electrons was allowed to be much tighter  
1058 because the number of signal events with a third electron is considerably smaller than for muons.  
1059 It should be re-emphasized the signal events that are present in Figures 5.24–5.26 do not represent  
1060 the full set of signal events, but only those with a real third lepton (which must come from some

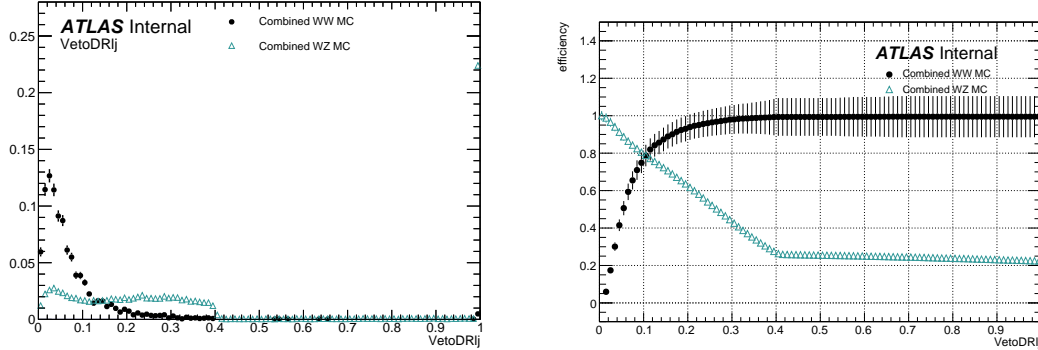


Figure 5.25: Distributions of  $\Delta R(\mu, j)$  for EWK and QCD  $W^\pm W^\pm jj$  signal (black) and  $WZ$  background (teal) for truth-matched third muons in events that pass the trilepton veto. Both distributions are normalized to unit area. The associated efficiency curves are on the right where efficiency is defined as the percentage of total events that would pass a cut on  $\Delta R(\mu, j)$  at a given value on the  $x$ -axis.

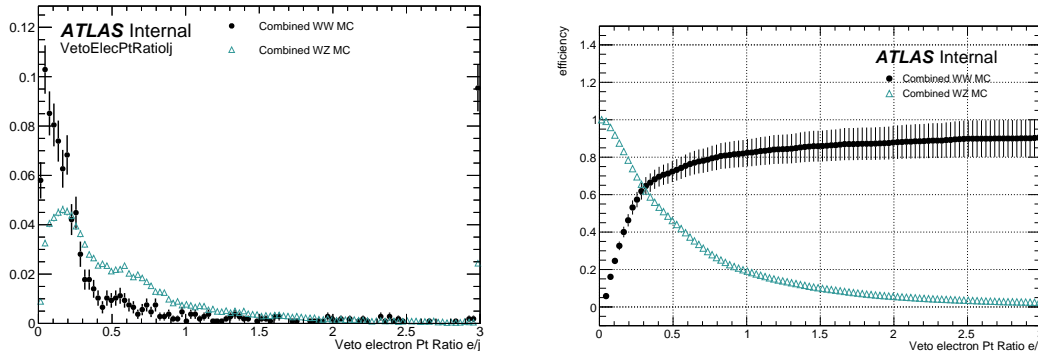


Figure 5.26: Distributions of  $p_{T,\text{ratio}}(e, j)$  for EWK and QCD  $W^\pm W^\pm jj$  signal (black) and  $WZ$  background (teal) for truth-matched third electrons in events that pass the trilepton veto. Both distributions are normalized to unit area. The associated efficiency curves are on the right where efficiency is defined as the percentage of total events that would pass a cut on  $p_{T,\text{ratio}}(e, j)$  at a given value on the  $x$ -axis.

source other than the signal  $W^\pm W^\pm jj$  process). For muons, an or of  $p_{T,\text{ratio}}(\mu, j)$  and  $\Delta R(\mu, j)$  is used to maximize the third lepton acceptance due to correlations between the quantities, as shown in Figure 5.27; for electrons, only a cut on  $p_{T,\text{ratio}}(e, j)$  is used. The Custom OR workingpoint is outlined in Table 5.17.

Custom OR Definition	
Muons	$p_{T,\text{ratio}}(\mu, j) > 0.40$ or $\Delta R(\mu, j) > 0.15$
Electrons	$p_{T,\text{ratio}}(e, j) > 0.18$

Table 5.17: Custom OR definition. Leptons must pass this selection in order to be counted for the trilepton veto.

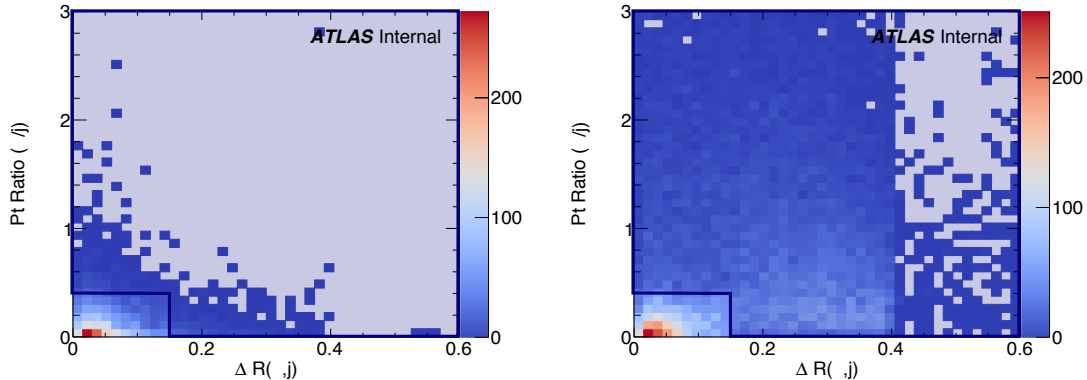


Figure 5.27: Two-dimensional plots of  $p_{T,\text{ratio}}(\mu, j)$  vs  $\Delta R(\mu, j)$  for truth-matched third muons in events that pass the trilepton veto for EWK and QCD  $W^\pm W^\pm jj$  signal (left) and  $WZ$  background (right). The blue overlay indicates the area in which the third leptons will pass the custom OR and result in the event failing the trilepton veto.

Tests of the performance of the Custom OR yield promising results, with approximately 20% reduction in  $WZ$  background compared to less than 2% signal loss in the signal region. Unfortunately, due to differences between the primary analysis framework and the one used for testing, in practice the gains in  $WZ$  rejection are not nearly as substantial, and ultimately the Custom OR is not included in the final analysis. However, it is still a potentially useful tool for improving background rejection via lepton number vetoes in analyses with overly aggressive OR procedures.

#### 5.4 Cross section measurement

The  $W^\pm W^\pm jj$  EWK cross section is extracted from the signal region using a maximum-likelihood fit applied simultaneously to four  $m_{jj}$  bins in the signal region as well as to the low- $m_{jj}$  and  $WZ$

control regions. For the fit and cross section extraction, the signal region is defined as in Table 5.8 with the dijet invariant mass requirement raised to  $m_{jj} > 500$  GeV. The low- $m_{jj}$  region is defined to mirror the signal region exactly with the dijet invariant mass inverted to  $200 < m_{jj} < 500$  GeV, and the  $WZ$  control region is defined previously in Section 5.3.1.

The signal and low- $m_{jj}$  regions are split into six channels based on the flavor and charge of the dilepton pair:  $\mu^+\mu^+$ ,  $\mu^-\mu^-$ ,  $\mu^+e^+$ ,  $\mu^-e^-$ ,  $e^+e^+$ , and  $e^-e^-$ . This split by charge increases the sensitivity of the measurement due to the  $W^+/W^-$  charge asymmetry at hadron colliders favoring the production of  $W^+$  bosons [52]. Since the signal events contain two  $W$  bosons, the signal strength compared to charge-symmetric backgrounds is much greater in the  $++$  channels for both charges combined. The  $WZ$  control region is included in the fit as a single bin ( $l^\pm l^\pm l^\pm$ ).

The maximum likelihood fit and cross section extractions are outlined in Sections 5.4.1 and 5.4.3, respectively. The results of the cross section measurement and of the analysis as a whole are presented in Section 5.6.

#### 5.4.1 Maximum likelihood fit

**TODO:** This section is very similar to what is written in the support note... May need to put some work into flushing it out so it's not so close to copy-paste The number of predicted signal events in each channel  $c$  and  $m_{jj}$  bin  $b$  can be calculated from the SM predicted signal cross section  $\sigma_{\text{theo}}^{\text{tot}}$ , the total integrated luminosity  $\mathcal{L}$ , the signal acceptance  $\mathcal{A}$ , and the efficiency corrections  $\mathcal{C}(\theta)$ , where  $\theta$  represents the set of nuisance parameters that parameterize the effects of each systematic uncertainty on the signal and background expectations. The acceptance and efficiency corrections will be covered in more detail in Section 5.4.2.

$$N_{cb}^{\text{sig}}(\theta) = \sigma_{\text{theo}}^{\text{tot}} \mathcal{A}_b \mathcal{C}_b(\theta) \mathcal{L} \quad (5.14)$$

A signal strength parameter  $\mu$  is defined as the ratio of the measured cross section to the SM predicted cross section. The expected number of events in a given channel and bin can then be expressed as the sum of the estimated background ( $N_{cb}^{\text{bkg}}(\theta)$ ) and the number of predicted signal events scaled by  $\mu$ :

$$\begin{aligned} N_{cb}^{\text{exp}}(\theta) &= \mu N_{cb}^{\text{sig}}(\theta) + N_{cb}^{\text{bkg}}(\theta) \\ &= \mu \sigma_{\text{theo}}^{\text{tot}} \mathcal{A}_b \mathcal{C}_b(\theta) \mathcal{L} + N_{cb}^{\text{bkg}}(\theta) \end{aligned} \quad (5.15)$$

The nuisance parameters are constrained by Gaussian probability distribution functions, and the normalization of the  $WZ$  background mentioned in Section 5.3.1 is included in the fit as a free

1101 parameter. The expected yields for signal and background processes are adjusted by the set of  
 1102 nuisance parameters within the constraints of the systematic uncertainties. The yields after the fit  
 1103 correspond to the value that best matches the observed data.

1104 The number of events per channel and bin after the fit can be written as a sum of the predicted  
 1105 event yields for each sample  $s$ :

$$\nu_{cb}(\phi, \theta, \gamma_{cb}) = \gamma_{cb} \sum_s [\eta_{cs}(\theta) \phi_{cs}(\theta) \lambda] h_{cbs}(\theta) \quad (5.16)$$

1106 In this equation, the fitted number of events in a given channel and bin is obtained by weighting  
 1107 the histogram of predicted yields  $h_{cbs}$  by the product of a given luminosity  $\lambda$  and any normalization  
 1108 factors  $\phi_{cs}$  that may be given for each channel and sample. The input histogram and the normal-  
 1109 ization factors may depend on the nuisance parameters  $\theta$  taking into account sources of systematic  
 1110 uncertainty. Uncertainties on the normalization factors  $\eta_{cs}(\theta)$  are also included. Finally, bin-by-bin  
 1111 scale factors  $\gamma_{cb}$  are included to parameterize the statistical uncertainties of the MC predictions.

1112 The binned likelihood function is given by a product of Gaussian functions for the luminosity  
 1113 and for the background uncertainties and a product of Poisson functions for the number of observed  
 1114 events in each bin and channel:

$$L(\mu|\theta) = \mathcal{G}(\mathcal{L}|\theta_{\mathcal{L}}, \sigma_{\mathcal{L}}) \cdot \prod_c \prod_b \mathcal{P}(N_{cb}^{\text{meas.}} | \nu_{cb}(\mu)) \prod_p \mathcal{G}(\theta_p^0 | \theta_p) \quad (5.17)$$

1115 where  $\mathcal{G}$  and  $\mathcal{P}$  are the Gaussian and Poisson functions, respectively. As before,  $\mathcal{L}$  represents the  
 1116 integrated luminosity with uncertainty  $\sigma_{\mathcal{L}}$  and associated nuisance parameter  $\theta_{\mathcal{L}}$ . The number of  
 1117 measured events in a given bin and channel is represented by  $N_{cb}^{\text{meas.}}$ , and  $\nu_{cb}(\mu)$  is the predicted  
 1118 number of events defined in Equation 5.16 expressed as a function of the signal strength  $\mu$ . Finally,  
 1119 the set of nuisance parameters  $\theta$  and any auxiliary measurements used to constrain them  $\theta^0$  are  
 1120 multiplied for each parameter  $p$ .

1121 The profile likelihood ratio is defined as

$$q_{\mu} = -2 \ln \frac{L(\mu, \hat{\theta}_{\mu})}{L(\hat{\mu}, \hat{\theta})} \quad (5.18)$$

1122 with  $\hat{\mu}$  and  $\hat{\theta}$  as the unconditional maximum likelihood estimates and  $\hat{\theta}$  as the conditional maximum  
 1123 likelihood estimate for a given value of  $\mu$ . The fitted signal strength  $\hat{\mu}$  is obtained by maximizing  
 1124 the likelihood function with respect to all parameters. The compatibility of the observed data  
 1125 with the background-only hypothesis can then be calculated by setting  $\mu = 0$ . Observation of the  
 1126  $W^{\pm}W^{\pm}jj$  EWK process is claimed if the data is found to be inconsistent with the background-only  
 1127 hypothesis by more than  $5\sigma$ .

1128 **5.4.2 Definition of the fiducial volume**

1129 Before extracting the cross section, it is necessary to define the fiducial volume, or the phase space  
 1130 of measureable events. It is a subset of the total phase space defined by selection requirements  
 1131 designed to mirror those applied in the analysis as closely as possible. The selection criteria for the  
 1132 fiducial volume are listed in Table 5.18.

Fiducial region selection	
Lepton selection	Two prompt leptons ( $e, \mu$ ) $p_T > 27$ GeV and $ \eta  < 2.5$ for both leptons Both leptons with the same electric charge Dilepton invariant mass $m_{ll} > 20$ GeV Dilepton separation $\Delta R(ll) > 0.3$
Missing transverse energy	Two neutrino system with $p_T^{\nu\nu} > 30$ GeV
Jet selection	At least two jets Leading jet $p_T > 65$ GeV Subleading jet $p_T > 35$ GeV Leading and subleading jet $ \eta  < 4.5$ Jet-lepton separation $\Delta R(l, j) > 0.3$ Dijet invariant mass $m_{jj} > 500$ GeV Dijet separation $\Delta y_{jj} > 2.0$

Table 5.18: Definition of the fiducial volume.

1133 In MC simulations, the total phase space is generated, providing the total theoretical cross section  
 1134  $\sigma_{\text{theo}}^{\text{tot}}$  and the total number of signal events  $\mathcal{N}_{\text{sig}}^{\text{tot}}$ <sup>13</sup>. After applying the fiducial selection at truth  
 1135 level, the total number of signal events in the fiducial region  $\mathcal{N}_{\text{sig}}^{\text{fid}}$  is obtained. An acceptance factor  
 1136  $\mathcal{A}$  is used to represent the efficiency of events falling in the fiducial region at truth level:

$$\mathcal{A} = \frac{\mathcal{N}_{\text{sig}}^{\text{fid}}}{\mathcal{N}_{\text{sig}}^{\text{tot}}} \quad (5.19)$$

1137 A correction factor  $\mathcal{C}$  is also necessary to translate from the truth level fiducial volume to the  
 1138 reconstruction level signal region and is defined in terms of the number of reconstruction level MC  
 1139 events in the signal region  $N_{\text{sig}, \text{MC}}^{\text{SR}}$ :

$$\mathcal{C} = \frac{N_{\text{sig}, \text{MC}}^{\text{SR}}}{\mathcal{N}_{\text{sig}}^{\text{fid}}} \quad (5.20)$$

1140 Since the fit is binned in  $m_{jj}$ , the acceptance and efficiency correction factors need to be as well.  
 1141 Therefore,  $\mathcal{A}_i$  and  $\mathcal{C}_{ij}$  are written in terms of truth  $m_{jj}$  bins  $i$  and reconstruction  $m_{jj}$  bins  $j$ . A  
 1142 graphical representation of these regions and the use of the acceptance and correction factors can  
 1143 be seen in Figure 5.28.

<sup>13</sup>For the purpose of clarity, the number of events at truth level is represented by a script  $\mathcal{N}$ , and the number of events at reconstruction level uses a regular  $N$ .

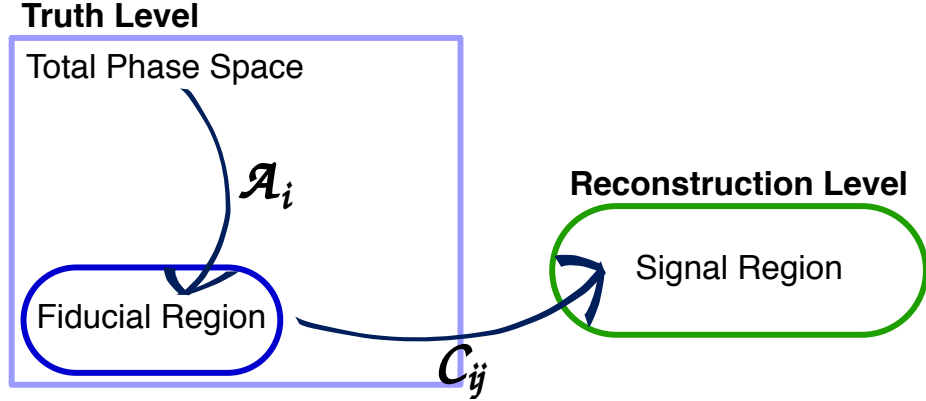


Figure 5.28: Visual representation of the different kinematic regions relevant to the cross section measurement. The acceptance factor  $\mathcal{A}$  converts from the truth level total phase space to the truth level fiducial region, and the efficiency correction  $\mathcal{C}$  translates the fiducial region in to the reconstruction level signal region.

#### 1144 5.4.3 Cross section extraction

1145 The  $W^\pm W^\pm jj$  EWK fiducial cross section is measured using the signal strength parameter  $\mu$  that is  
 1146 determined by the maximum likelihood fit. This parameter is dependent on the nuisance parameters  
 1147  $\theta$  and can be written explicitly in terms of the measured and theoretical cross sections as:

$$\mu(\theta) = \frac{\sigma_{\text{meas}}^{\text{SR}}}{\sigma_{\text{theo}}^{\text{SR}}} \quad (5.21)$$

1148 In the simple case with only one bin, the equation for the total number of expected events in the  
 1149 signal region first introduced in Equation 5.15 can be written as:

$$N_{\text{exp}}^{\text{SR}}(\theta) = \mu(\theta) \cdot \sigma_{\text{theo}}^{\text{tot}} \cdot \mathcal{L} \cdot \mathcal{A} \cdot \mathcal{C}(\theta) + N_{\text{bkg}}^{\text{SR}}(\theta) \quad (5.22)$$

1150 with the non-binned versions of  $\mathcal{A}$  and  $\mathcal{C}$  defined in Equations 5.19 and 5.20, respectively.

1151 If the measured fiducial cross section is written as:

$$\sigma_{\text{meas}}^{\text{fid}} = \mu \cdot \mathcal{A} \cdot \sigma_{\text{theo}}^{\text{tot}} \quad (5.23)$$

1152 then Equation 5.22 can be rearranged to read:

$$\sigma_{\text{meas}}^{\text{fid}} = \frac{N_{\text{exp}}^{\text{SR}}(\theta) - N_{\text{bkg}}^{\text{SR}}(\theta)}{\mathcal{L} \cdot \mathcal{C}(\theta)} \quad (5.24)$$

1153 The measured fiducial cross section can finally be rewritten in terms of  $\hat{\mu}$ , which is the best estimator  
 1154 of the signal strength as extracted from the fit:

$$\begin{aligned} \sigma_{\text{meas}}^{\text{fid}} &= \hat{\mu}(\theta) \cdot \sigma_{\text{theo}}^{\text{tot}} \cdot \mathcal{A} \\ &= \hat{\mu}(\theta) \cdot \sigma_{\text{theo}}^{\text{fid}} \end{aligned} \quad (5.25)$$

1155 In practice, however, the cross section is not extracted from a single bin, and Equation 5.22  
 1156 becomes for a single channel in truth and reconstruction level  $m_{jj}$  bins  $i$  and  $j$ , respectively:

$$N_{\text{exp}}^{\text{SR}}(\theta) = \mu(\theta) \cdot \sigma_{\text{theo}}^{\text{tot}} \cdot \mathcal{L} \cdot \sum_i \mathcal{A}_i \cdot \sum_j \mathcal{C}_{ij} + \sum_j N_{\text{bkg},j}^{\text{SR}}(\theta) \quad (5.26)$$

1157 where now the binned versions of  $\mathcal{A}_i$  and  $\mathcal{C}_{ij}$  are used. This equation can be extended to include all  
 1158 the analysis channels by increasing the number of bins  $i$  and  $j$ . Additionally, it can be shown that  
 1159 Equation 5.25 holds for this more complex case as well [17], provided care is taken to ensure that  
 1160 all the uncertainties are handled properly.

## 1161 5.5 Summary of uncertainties

1162 Systematic uncertainties enter the final fit as nuisance parameters which can impact the estimated  
 1163 signal and background yields and the shapes of the  $m_{jj}$  distributions. These uncertainties can arise  
 1164 from the experimental methods or from the theoretical calculations used in the analysis. This section  
 1165 summarizes the systematic uncertainties; the experimental uncertainties are detailed in Section 5.5.1,  
 1166 and the theoretical uncertainties are covered in Section 5.5.2. The impacts of the systematic uncer-  
 1167 tainties on the final cross section measurement are summarized in Table 5.19.

Source	Impact [%]
Reconstruction	$\pm 4.0$
Electrons	$\pm 0.5$
Muons	$\pm 1.2$
Jets and $E_{\text{T}}^{\text{miss}}$	$\pm 2.8$
$b$ -tagging	$\pm 2.0$
Pileup	$\pm 1.5$
Background	$\pm 5.0$
Misid. leptons	$\pm 3.9$
Charge misrec.	$\pm 0.3$
$WZ$	$\pm 1.3$
$W^\pm W^\pm jj$ QCD	$\pm 2.8$
Other	$\pm 0.8$
Signal	$\pm 3.6$
Interference	$\pm 1.0$
EW Corrections	$\pm 1.3$
Shower, Scale, PDF & $\alpha_s$	$\pm 3.2$
Total	$\pm 7.4$

Table 5.19: Impact of various systematic effects on the fiducial cross section measurement. The impact of a given source of uncertainty is computed by performing the fit with the corresponding nuisance parameter varied up or down by one standard deviation from its nominal value.

---

1168   **5.5.1 Experimental uncertainties**

1169   Experimental uncertainties include detector effects as well as uncertainties on the background es-  
1170   timation methods. Sources of systematic uncertainty on the measurement of physics objects are  
1171   listed in Table 5.20, grouped by the relevant object type. For backgrounds estimated from MC  
1172   simulations, variations in these sources of uncertainty are propagated through the analysis to obtain  
1173   the corresponding uncertainties on the event yields. Additional experimental uncertainties include  
1174   the integrated luminosity, the photon conversion rate from Section 5.3.2, and the data driven charge  
1175   misidentification and fake lepton background estimations from Sections 5.3.3 and 5.3.4.5, respec-  
1176   tively.

1177   The largest sources of experimental uncertainty on the MC estimations come from the jet-related  
1178   uncertainties and the  $b$ -tagging efficiency, while the largest uncertainty on the background estimation  
1179   comes from the fake factor. The effects of the uncertainties on the  $W^\pm W^\pm jj$  EWK signal and the  
1180   dominant MC estimated background,  $WZ$ , are listed in Tables 5.21 and 5.22, respectively. Since  
1181   the overall contributions from other processes estimated with MC are small, the uncertainties on  
1182   these backgrounds have a lesser impact on the final measurement; these tables can be found in  
1183   Appendix B.1.

Experimental uncertainties	
Electrons	Energy resolution
	Energy scale
	Identification efficiency
	Isolation efficiency
	Reconstruction efficiency
	Trigger efficiency
Muons	Energy scale
	Identification efficiency
	Inner detector track resolution
	Muon spectrometer resolution
	Trigger efficiency
$E_T^{\text{miss}}$	Resolution
	Scale
Jets	Energy resolution
	Energy scale
	JVT cut efficiency
	$b$ -tagging efficiency
Jets from pileup	

Table 5.20: List of sources of experimental uncertainties on the reconstruction of physics objects.

$W^\pm W^\pm jj$ EWK	$e^\pm e^\pm$ % Yield	$\mu^\pm e^\pm$ % Yield	$\mu^\pm \mu^\pm$ % Yield
Jet-related Uncertainties	2.28	2.22	2.28
b-tagging efficiency	1.81	1.76	1.74
Pile-up	0.48	0.97	2.42
Trigger efficiency	0.02	0.08	0.47
Lepton reconstruction/ID	1.45	1.14	1.83
MET reconstruction	0.26	0.17	0.21

Table 5.21: Impact of experimental uncertainties for the  $W^\pm W^\pm jj$  EWK processes in all channels.

$WZ$	$e^\pm e^\pm$ % Yield	$\mu^\pm e^\pm$ % Yield	$\mu^\pm \mu^\pm$ % Yield
Jet-related Uncertainties	9.58	5.03	8.45
b-tagging efficiency	2.49	2.23	2.40
Pile-up	2.99	3.49	3.33
Trigger efficiency	0.03	0.09	0.43
Lepton reconstruction/ID	1.52	1.24	3.07
MET reconstruction	0.93	0.79	1.63

Table 5.22: Impact of experimental uncertainties for the  $WZ$  process in all channels.

### 1184 5.5.2 Theoretical uncertainties

1185 It is also necessary to consider uncertainties on the theoretical predictions in the fiducial region. They  
 1186 include the choice of PDF set, the value of the strong coupling constant  $\alpha_s$ , the renormalization  
 1187 scale  $\mu_R$ , the factorization scale  $\mu_F$ , and the parton showering. The size of these uncertainties are  
 1188 measured by generating new samples with variations in a chosen parameters and comparing them  
 1189 to samples using the nominal choice of the parameter. Internal variations on the PDF sets or using  
 1190 a different set entirely results in a relative uncertainty of up to 2.25% on the nominal sample. The  
 1191 impact from varying  $\alpha_s$  is very small, on the order of < 0.01%. The factorization and renormalization  
 1192 scales are independently varied between 0.5-2.0 from their nominal values of 1.0. This results in  
 1193 relative uncertainties on the prediction of up to 15%. Finally, varying the parameters in the parton  
 1194 showering results in up to 8% uncertainty.

#### 1195 5.5.2.1 Uncertainties from EWK-QCD interference

1196 As mentioned in Section 5.0.1,  $W^\pm W^\pm jj$  production consists of both EWK processes. The two  
 1197 production modes cannot be naively separated due to cross terms in the matrix element calculation.  
 1198 These cross terms are referred to as *interference* terms. Since the  $W^\pm W^\pm jj$  EWK production is  
 1199 the focus of the analysis, and the signal region is designed to preferentially select those events, it is  
 1200 important to measure the size of the EWK-QCD interference contributions.

1201     The interference effects are estimated using the `MadGraph` MC generator, as it has a feature that  
 1202     allows direct modelling of the interference term. This allows four samples to be generated:

- 1203     1. Inclusive: All available diagrams are used in the matrix element calculation  
 1204     2. EWK only: Only EWK diagrams ( $\mathcal{O}(\alpha_{\text{EWK}}) = 4$ ) are used  
 1205     3. QCD only: Only QCD diagrams ( $\mathcal{O}(\alpha_s) = 2 \otimes \mathcal{O}(\alpha_{\text{EWK}}) = 2$ ) are used  
 1206     4. Interference: Only the interference terms are used

1207     A minimal set of generator level cuts, listed in Table 5.23, is applied in order to avoid biasing the  
 1208     sample towards either production mode. The cross sections for each of the four channels can be  
 1209     found in Table 5.24. The size of the interference is found to be approximately 6% of the total cross  
 1210     section and is taken as a systematic uncertainty.

Generator level cuts
$\Delta\eta_{jj} < 10$
Jet $p_{\text{T}} > 20$ GeV
$M_{jj} > 10$ GeV

Table 5.23: The set of generator level cuts used for generating the interference samples with `MadGraph`.

Sample	$\sigma$ (fb)
Inclusive	$3.646 \pm 0.0012$
EWK only	$2.132 \pm 0.0005$
QCD only	$1.371 \pm 0.0008$
Interference	$0.227 \pm 0.0002$

Table 5.24: Cross sections for each different  $W^\pm W^\pm jj$  production mode (inclusive, EWK only, QCD only, and interference only) generated using `MadGraph`. The cross sections are calculated using a minimal set of generator level cuts from events where the  $W$  decays to a muon.

## 1211     5.6 Results

1212     After running the full analysis chain, the event yields in the signal region, low- $m_{jj}$  control region,  
 1213     and  $WZ$  control region as well as associated nuisance parameters representing the uncertainties are  
 1214     passed to the maximum likelihood fit. From this fit, the normalization factor for the  $WZ$  control  
 1215     region  $\mu_{WZ}$  and the signal strength parameter in the signal region  $\mu_{\text{obs}}$  are determined, and the  
 1216     predicted yields in each input bin have been shifted according to the process detailed in Section 5.4.1.

1217 The  $WZ$  normalization factor is measured to be:

$$\mu_{WZ} = 0.88^{+0.07}_{-0.07}(\text{stat})^{+0.31}_{-0.21}(\text{theory})^{+0.22}_{-0.11}(\text{sys}) \quad (5.27)$$

1218 and is constrained primarily by the number of data events in the  $WZ$  control region. The observed  
 1219 signal strength of  $W^\pm W^\pm jj$  EWK production, defined in Equation 5.21, is extracted from the fit  
 1220 and measured with respect to the prediction of the **SHERPA v2.2.2** MC generator:

$$\mu_{\text{obs}} = 1.45^{+0.25}_{-0.24}(\text{stat})^{+0.06}_{-0.08}(\text{theory})^{+0.27}_{-0.22}(\text{sys}) \quad (5.28)$$

1221 This corresponds to a rejection of the background-only hypothesis with a significance of  $6.9\sigma$ .

1222 The observed number of data events are compared to the predicted signal and background yields  
 1223 in the signal region in Table 5.25 before applying the fit and in Table 5.26 after the fit. The  $m_{jj}$   
 1224 distributions for data and prediction are shown in Figure 5.29 after the fit, and the fitted event  
 1225 yields in the low- $m_{jj}$  and  $WZ$  control regions are shown in Figure 5.30. Additional distributions  
 1226 can be found in Appendix B.

	$e^+e^+$	$e^-e^-$	$\mu^+e^+$	$\mu^\pm e^\pm m$	$\mu^+\mu^+$	$\mu^-\mu^-$	combined
$WZ$	$1.9 \pm 0.6$	$1.3 \pm 0.4$	$14 \pm 4$	$8.9 \pm 2.6$	$5.5 \pm 1.6$	$3.6 \pm 1.1$	$35 \pm 10$
Non-prompt	$4.1 \pm 2.3$	$2.3 \pm 1.7$	$9 \pm 5$	$6 \pm 4$	$0.57 \pm 0.15$	$0.67 \pm 0.25$	$23 \pm 10$
$e/\gamma$ conversions	$1.74 \pm 0.29$	$1.8 \pm 0.4$	$6.1 \pm 1.6$	$3.7 \pm 0.8$	—	—	$13.4 \pm 2.5$
Other prompt	$0.17 \pm 0.05$	$0.14 \pm 0.04$	$0.90 \pm 0.19$	$0.60 \pm 0.14$	$0.36 \pm 0.10$	$0.19 \pm 0.05$	$2.4 \pm 0.5$
$W^\pm W^\pm jj$ QCD	$0.38 \pm 0.13$	$0.16 \pm 0.05$	$3.0 \pm 1.0$	$1.2 \pm 0.4$	$1.8 \pm 0.6$	$0.76 \pm 0.25$	$7.3 \pm 2.5$
Expected background	$8.2 \pm 2.4$	$5.7 \pm 1.8$	$33 \pm 7$	$21 \pm 5$	$8.2 \pm 1.8$	$5.3 \pm 1.2$	$81 \pm 14$
$W^\pm W^\pm jj$ EWK	$3.8 \pm 0.6$	$1.49 \pm 0.22$	$16.5 \pm 2.5$	$6.5 \pm 1.0$	$9.1 \pm 1.4$	$3.5 \pm 0.5$	$41 \pm 6$
Data	10	4	44	28	25	11	122

Table 5.25: Table of the data and prediction event yields in the signal region before the fit. Numbers are shown for the six lepton flavor and charge channels and for all channels combined. Here the  $WZ$  background yields are normalized to the data in the  $WZ$  control region. The background estimations from the fake factor are included in the “Non-prompt” category, and backgrounds from  $V\gamma$  production and electron charge misidentification are combined in the “ $e/\gamma$  conversions” category. Finally,  $ZZ$ ,  $VVV$ , and  $t\bar{t}V$  backgrounds are combined in the “Other prompt” category.

1227 The last ingredient necessary to measure the  $W^\pm W^\pm jj$  EWK cross section is the theory predicted  
 1228 cross section in the fiducial region defined in Table 5.18. **SHERPA v2.2.2** is used for the calculation,  
 1229 and the cross section in the total generator phase space is  $40.81 \pm 0.05$  fb, and the fiducial cross section  
 1230 is  $2.01 \pm 0.02$  fb. This corresponds to an acceptance factor of  $\mathcal{A} = 0.0493 \pm 0.0002$ . Uncertainties on  
 1231 the simulation are estimated using variations of the scale, parton shower, and PDF set. The final  
 1232 prediction used in the cross section measurement including uncertainties from Section 5.5.2 is:

$$\sigma_{\text{SHERPA}}^{\text{fid}} = 2.01 \pm 0.02(\text{stat})^{+0.29}_{-0.23}(\text{scale})^{+0.16}_{-0.02}(\text{parton shower})^{+0.05}_{-0.03}(\text{PDF}) \text{ fb} \quad (5.29)$$

	$e^+e^+$	$e^-e^-$	$\mu^+e^+$	$\mu^\pm e^\pm m$	$\mu^+\mu^+$	$\mu^-\mu^-$	combined
$WZ$	$1.49 \pm 0.30$	$1.10 \pm 0.26$	$11.7 \pm 1.7$	$8.0 \pm 1.3$	$5.0 \pm 0.6$	$3.5 \pm 0.6$	$31 \pm 4$
Non-prompt	$2.2 \pm 1.3$	$1.2 \pm 0.7$	$5.7 \pm 2.8$	$4.5 \pm 1.8$	$0.57 \pm 0.06$	$0.65 \pm 0.14$	$15 \pm 6$
$e/\gamma$ conversions	$1.6 \pm 0.4$	$1.6 \pm 0.5$	$6.3 \pm 1.6$	$4.3 \pm 1.1$	—	—	$13.8 \pm 2.9$
Other prompt	$0.16 \pm 0.04$	$0.14 \pm 0.04$	$0.90 \pm 0.19$	$0.63 \pm 0.13$	$0.39 \pm 0.09$	$0.22 \pm 0.05$	$2.4 \pm 0.5$
$W^\pm W^\pm jj$ QCD	$0.35 \pm 0.13$	$0.15 \pm 0.05$	$2.9 \pm 1.0$	$1.2 \pm 0.4$	$1.8 \pm 0.6$	$0.76 \pm 0.25$	$7.2 \pm 2.4$
Expected background	$5.8 \pm 1.5$	$4.1 \pm 1.1$	$27 \pm 4$	$18.7 \pm 2.6$	$7.7 \pm 0.8$	$5.1 \pm 0.6$	$69 \pm 7$
$W^\pm W^\pm jj$ EWK	$5.6 \pm 1.0$	$2.2 \pm 0.4$	$24 \pm 5$	$9.4 \pm 1.8$	$13.5 \pm 2.5$	$5.2 \pm 1.0$	$60 \pm 11$
Data	10	4	44	28	25	11	122

Table 5.26: Table of the data and prediction event yields in the signal region after the fit. Numbers are shown for the six lepton flavor and charge channels and for all channels combined. The background estimations from the fake factor are included in the “Non-prompt” category, and backgrounds from  $V\gamma$  production and electron charge misidentification are combined in the “ $e/\gamma$  conversions” category. Finally,  $ZZ$ ,  $VVV$ , and  $t\bar{t}V$  backgrounds are combined in the “Other prompt” category.

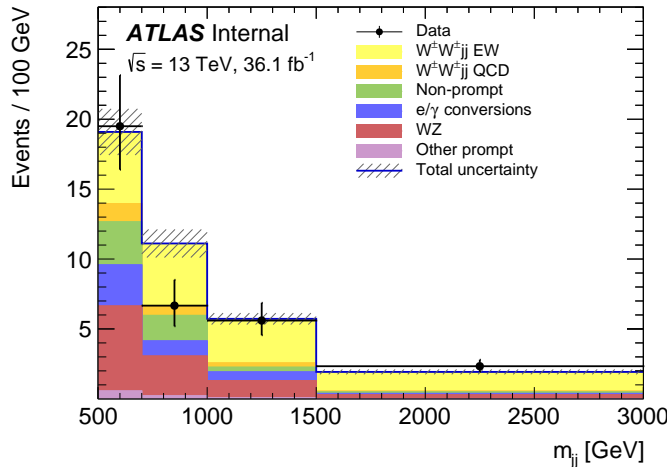


Figure 5.29: The dijet invariant mass  $m_{jj}$  distributions for data and predicted signal and background in the signal region after the fit. The shaded band represents the statistical and systematic uncertainties added in quadrature. Note that the bins have been scaled such that they represent the number of events per  $100 \text{ GeV}$  in  $m_{jj}$ . The background estimations from the fake factor are included in the “Non-prompt” category, and backgrounds from  $V\gamma$  production and electron charge misidentification are combined in the “ $e/\gamma$  conversions” category. Finally,  $ZZ$ ,  $VVV$ , and  $t\bar{t}V$  backgrounds are combined in the “Other prompt” category.

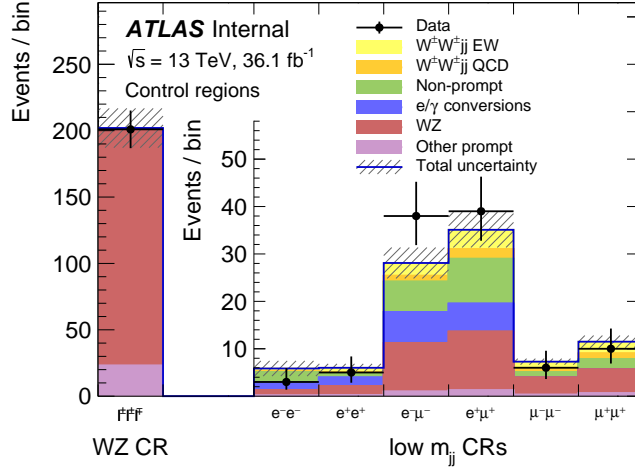


Figure 5.30: The event yields for data and predicted signal and background in the  $WZ$  and low- $m_{jj}$  control regions after the fit. The shaded band represents the statistical and systematic uncertainties added in quadrature. The background estimations from the fake factor are included in the “Non-prompt” category, and backgrounds from  $V\gamma$  production and electron charge misidentification are combined in the “ $e/\gamma$  conversions” category. Finally,  $ZZ$ ,  $VVV$ , and  $t\bar{t}V$  backgrounds are combined in the “Other prompt” category.

1233 Combining this **SHERPA** prediction with the measured signal strength  $\mu_{\text{obs}}$  from Equation 5.28,  
 1234 the measured fiducial cross section  $\sigma_{\text{meas}}^{\text{fid}}$  can be calculated using Equation 5.25:

$$\sigma_{\text{meas}}^{\text{fid}} = 2.91_{-0.47}^{+0.51}(\text{stat})_{-0.16}^{+0.12}(\text{theory})_{-0.23}^{+0.24}(\text{sys})_{-0.06}^{+0.08}(\text{luminosity}) \text{ fb} \quad (5.30)$$

1235 A plot comparing the measured fiducial cross section to two theoretical calculations is shown in  
 1236 Figure 5.31. The measured value is compared to the **SHERPA v2.2.2** prediction used to calculate  
 1237  $\mu_{\text{obs}}$  as well as to **POWHEG-BOX v2**. As mentioned in Section 5.1.1, this **POWHEG** sample does not  
 1238 include the resonant triboson diagrams and is only used here for a visual comparison.

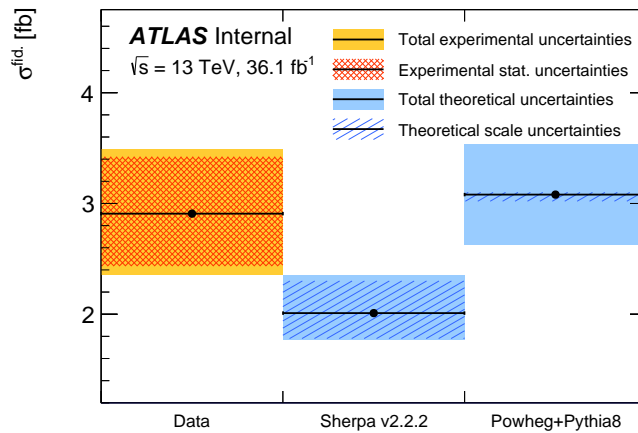


Figure 5.31: Comparison of the measured  $W^\pm W^\pm jj$  EWK fiducial cross section with theoretical calculations from **SHERPA v2.2.2** and **POWHEG-BOX v2**. The light orange band represents the total experimental uncertainty on the measured value, and the dark orange hashed band is the statistical uncertainty. For the simulations, the light blue band represents the total theoretical uncertainty, and the dark blue hashed band are the scale uncertainties. The theory predictions do not include the interference between the EWK and QCD production.

## CHAPTER 6

---

# Prospects for same-sign $WW$ at the High Luminosity LHC

---

1242 On December 3, 2018, Run 2 of the LHC officially ended, and the collider was shut down to begin  
 1243 the first of two scheduled extended maintenance periods [53]. During these two long shutdowns,  
 1244 the Phase-I and Phase-II upgrades of the LHC and ATLAS will occur in order to prepare for the  
 1245 High-Luminosity LHC (HL-LHC) which is scheduled to begin operation in 2026 [54].

1246 The HL-LHC is planned to run at a center-of-mass energy of  $\sqrt{s} = 14$  TeV with an instantaneous  
 1247 luminosity of  $\mathcal{L} = 5 \times 10^{34}$  cm $^{-2}$ s $^{-1}$  with up to 200 collisions per beam-crossing. Over the course  
 1248 of operation, the HL-LHC is expected to collect a total integrated luminosity of  $\mathcal{L} = 3000$  fb $^{-1}$  by  
 1249 2035 [55]. **TODO: Compare to current LHC numbers?**

1250 These run conditions will be much harsher than what ATLAS has experienced so far, and there  
 1251 are several upgrades planned for the detector to operate in the high luminosity environment. Most  
 1252 notably, the entire ID will be replaced with an all-silicon tracker which will extend the coverage from  
 1253  $|\eta| \leq 2.7$  up to  $|\eta| \leq 4.0$ . This will allow for reconstruction of charged particle tracks which can  
 1254 in turn be matched to clusters in the calorimeters for electron identification or forward jet tagging  
 1255 [56].

1256 The upgraded detector, the higher beam energy, and the increased volume of data to be collected  
 1257 provides the opportunity to measure rarer processes with a much higher precision than what was  
 1258 possible in Run 1. Same-sign  $W^\pm W^\pm jj$  production, is one such process. With greater statistics,  
 1259 the accuracy of the cross section measurement can be improved over the 13 TeV analysis detailed in  
 1260 Chapter 5, and it also will allow for more detailed physics studies, such as measuring the polarization  
 1261 of the  $W$  bosons. A measurement of the longitudinal polarization of the scattered  $W$  bosons has

1262 not yet been possible, but it remains of great interest due to its sensitivity to electroweak symmetry  
 1263 breaking [57]. The analysis detailed in this chapter is based off of the 2018 ATLAS HL-LHC  
 1264  $W^\pm W^\pm jj$  prospects study [58] which is itself an extension of the 2017 ATLAS study [59]. **TODO:**  
 1265 mention CMS's study + yellow report?

### 1266 6.0.1 Analysis Overview

1267 The experimental signature of interest is identical to the 13 TeV analysis: two prompt leptons (either  
 1268 electrons or muons) with the same charge, missing transverse energy, and two high energy, forward  
 1269 jets. These jets are again required to have a large angular separation and a high combined invariant  
 1270 mass to preferentially select EWK- over QCD-produced  $W^\pm W^\pm jj$  events.

1271 Background processes are again similar to the 13 TeV analysis and are summarized again here.  
 1272 The dominant source of prompt background from  $WZ+jets$  events where both bosons decay lepton-  
 1273 ically. If the lepton from the  $Z$ -decay with opposite charge from the  $W$  falls outside of the detector  
 1274 acceptance or is not identified, the remainder could appear to be a  $W^\pm W^\pm jj$  signal event. To a  
 1275 lesser extent,  $ZZ+jets$  events can enter the signal region in much the same way provided two lep-  
 1276 tons are “lost”. Other prompt sources include  $t\bar{t}+V$  and multiple parton interactions, however  
 1277 these processes do not contribute much. These prompt backgrounds are expected to contribute  
 1278 less than in Run 2 with the addition of forward tracking in the upgraded ATLAS detector. Jets  
 1279 mis-reconstructed as leptons or leptons from hadronic decays (such as  $t\bar{t}$  and  $W+jets$  production)  
 1280 comprise the non-prompt lepton background. Lastly, events with two prompt, opposite-charge elec-  
 1281 trons can appear as a same-sign event provided one of the electrons is mis-reconstructed as the  
 1282 wrong charge.

1283 In this analysis, the EWK production of  $W^\pm W^\pm jj$  is studied in the context of the planned  
 1284 HL-LHC run conditions and upgraded ATLAS detector. An optimized event selection (referred to  
 1285 as the *optimized selection*) is also explored in an effort to gain increased signal significance over  
 1286 the *default selection*. The cross section of the inclusive EWK production is measured for both the  
 1287 default and optimized selections, and the extraction of the longitudinal scattering significance is  
 1288 measured with the optimized selection.

## 1289 6.1 Theoretical motivation

1290 The theoretical motivation for studying the ssWW process—and VBS in general—is detailed in Sec-  
 1291 tion 5.0.1. Since it is specifically the scattering of *longitudinally polarized* vector bosons that violates

1292 unitarity without a SM Higgs boson, a direct measurement of this cross section will be very useful  
 1293 for understanding how the Higgs unitarizes the process [57].

### 1294 6.1.1 Experimental sensitivity to longitudinal polarization

1295 **TODO:** mention that since there are so many polarization possibilities, a large integrated luminosity  
 1296 is needed to measure just one of them individually There are three possible polarization states for  
 1297 a massive vector boson: two transverse (+ or -) and one longitudinal (0). Therefore, in a system  
 1298 with two  $W$  bosons, the overall polarization can be purely longitudinal (00), purely transverse (++,  
 1299 --, and +-), or mixed (+0 and -0). The three combinations will be referred to as  $LL$ ,  $TT$ , and  
 1300  $LT$  respectively.

1301 In order extract the longitudinal scattering component, it is necessary to find variables that  
 1302 distinguish the  $LL$  from the  $TT$  and  $LT$ . Several were studied, and those with the best discriminating  
 1303 power between the polarizations are the leading and subleading lepton  $p_T$  as well as the azimuthal  
 1304 separation ( $|\Delta\phi_{jj}|$ ) of the two VBS jets. The  $LL$  events prefer lower  $p_T$  for both signal leptons  
 1305 (see Figure 6.1), which motivates keeping cuts on these quantities as low as possible in the event  
 1306 selection. In the case of  $|\Delta\phi_{jj}|$ , the  $LL$  events generally had a larger dijet separation (see Figure 6.2),  
 1307 and this variable is used in a binned likelihood fit to extract the longitudinal scattering significance.

## 1308 6.2 Monte Carlo samples

1309 As no real HL-LHC data will be available for many years, all signal and background processes  
 1310 are modeled using MC simulations generated at  $\sqrt{s} = 14$  TeV, with the event yields scaled to the  
 1311 anticipated HL-LHC integrated luminosity of  $\mathcal{L} = 3000 \text{ fb}^{-1}$ . The MC samples used in the analysis  
 1312 are generated at particle-level and have not been run through the typical full simulation of the  
 1313 ATLAS detector. Instead, smearing functions derived from a **GEANT4** simulation of the upgraded  
 1314 ATLAS detector are used to estimate detector effects such as momentum resolution. In addition,  
 1315 pileup events are fully simulated. The MC samples used in this analysis are summarized in Table 6.1.

1316 The signal sample consists of both VBS and non-VBS electroweak (EWK)  $W^\pm W^\pm jj$  production,  
 1317 and it is simulated with the **Madgraph5\_aMC@NLO** generator using the NNPDF3.0 PDF set and in-  
 1318 terfaced with **PYTHIA v8** [60] for hadronization and parton showering. To study the longitudinal  
 1319 polarization more directly, two additional **Madgraph5\_aMC@NLO**  $W^\pm W^\pm jj$  samples are used: one  
 1320 containing only the longitudinal contribution (LL) and a second containing the transverse (TT) and  
 1321 mixed (LT) contributions.

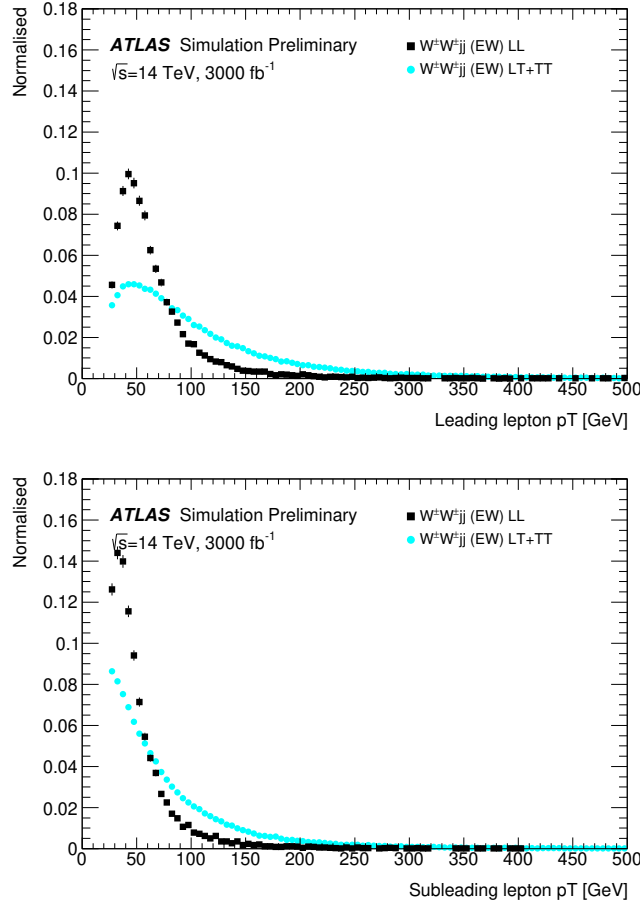


Figure 6.1: Comparison of the leading (top) and subleading (bottom) lepton  $p_T$  distributions for purely longitudinal (LL, black) and mixed polarization (LT+TT, cyan)  $W^\pm W^\pm jj$  events.

1322 There are many other processes that can produce the same final state as the  $W^\pm W^\pm jj$  and  
 1323 must also be accounted for using MC simulations.  $WZ$  events are generated using **SHERPA v2.2.0**,  
 1324 which includes up to one parton at NLO in the strong coupling constant and up to three addi-  
 1325 tional partons at LO. Both EWK and QCD production are included in these samples.  $ZZ$  and  
 1326 triboson  $VVV$  ( $V = W, Z$ ) events are generated using **SHERPA v2.2.2** with up to two additional  
 1327 partons in the final state. For the triboson backgrounds, the bosons can decay leptonically or  
 1328 hadronically.  $W+jets$  backgrounds are generated for electron, muon, and tau final states at LO  
 1329 with **Madgraph5\_aMC@NLO** and the **NNPDF3.0** set with showering from **PYTHIA v8**.  $Z+jets$  events are  
 1330 produced using **POWHEG-BOX v2** and the **CT10** PDF set interfaced with **PYTHIA v8**. Finally,  $t\bar{t}$  and  
 1331 single-top events are generated using **POWHEG-BOX** with showering from **PYTHIA v6**.

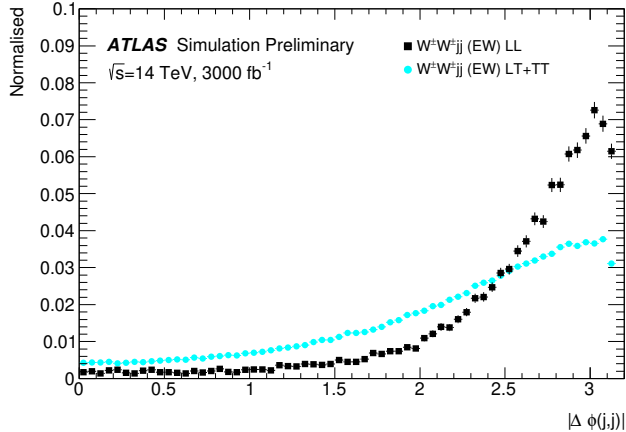


Figure 6.2: Comparison of the azimuthal dijet separation ( $|\Delta\phi_{jj}|$ ) for purely longitudinal (LL, black) and mixed polarization (LT+TT, cyan)  $W^{\pm}W^{\pm}jj$  events.

Process	Generator	Comments
$W^{\pm}W^{\pm}jj$ (EWK)	Madgraph5_aMC@NLO	Signal sample
$W^{\pm}W^{\pm}jj$ (QCD)	Madgraph5_aMC@NLO	
$W^{\pm}W^{\pm}jj$ (LL)	Madgraph5_aMC@NLO	Pure longitudinal polarization sample
$W^{\pm}W^{\pm}jj$ (TT+LT)	Madgraph5_aMC@NLO	Mixed and transverse polarization sample
Diboson	SHERPA v2.2.0	$WZ$ events
	SHERPA v2.2.2	$ZZ$ events
Triboson	SHERPA v2.2.2	
$W+jets$	Madgraph5_aMC@NLO	
$Z+jets$	POWHEG-BOX v2	
$t\bar{t}$	POWHEG-BOX	
Single top	POWHEG-BOS	

Table 6.1: Summary of MC samples used in the analysis.

### 1332 6.3 Background estimations

1333 In this analysis, all background contributions are estimated using MC simulations. Backgrounds such  
 1334 as electron charge misidentification and fake electrons from jets (which are traditionally estimated  
 1335 using data-driven techniques) are estimated using a set of parameterization functions applied to the  
 1336 MC. These functions calculate the probability that an electron is assigned the wrong charge or a  
 1337 jet is mis-reconstructed as an electron parameterized by the  $p_T$  and  $\eta$  of the electron or jet. The  
 1338 probabilities are derived from studies on expected electron performance with the upgraded ATLAS  
 1339 detector [61].

1340 Processes involving two  $W$  and  $Z$  bosons are grouped together as *diboson* backgrounds, with the

exception of  $W^\pm W^\pm jj$  events produced via QCD interactions, which are kept separate. Similarly, all backgrounds with three vector bosons are combined and labeled as *triboson*. Any  $W+jets$  or top events that pass selection and do not contain a fake electron, as well as any  $Z+jets$  events without an electron identified as having its charge misidentified are combined as *other non-prompt* backgrounds.

### 6.3.1 Truth-based isolation

To properly calculate particle isolation, it requires information from several detector subsystems including tracking and calorimeter responses. Since the MC samples used in this analysis have not been run through a full detector simulation, it is not possible to construct the canonical isolation variables used in analyses. At truth-level, this is generally not a serious concern as  $p_T$  signal leptons tend to be well isolated to begin with. However, isolation is one of the most powerful tools for rejecting leptons from non-prompt sources such as top events, which are produced in association with additional nearby particles from  $b$  and  $c$  quark decays. In this analysis, with the absence of any sort of isolation requirement, contributions from top backgrounds (including single top,  $t\bar{t}$  and  $t\bar{t} + V$ ) are more than an order of magnitude higher than expected.

As a result, it is necessary to find one or more quantities that are comparable to the isolation information that is available in fully-simulated samples. Analogues to track- and calorimeter-based isolation variables are constructed by summing the momentum and energy, respectively, of stable truth particles with  $p_T > 1$  GeV within a specified radius of each signal lepton. For the track-based isolation, only charged truth particles are used; both charged and neutral particles (excluding neutrinos) are included for the calorimeter-based isolation. Ultimately, a set of isolation cuts are chosen that are similar to those recommended by ATLAS for Run 2 analyses. The truth-based isolation requirements are listed in Table 6.2.

	Electron Isolation	Muon Isolation
Track-based isolation cone size	$\Delta R < 0.2$	$\Delta R < 0.3$
Track-based isolation requirement	$\sum p_T/p_T^e < 0.06$	$\sum p_T/p_T^\mu < 0.04$
Calorimeter-based isolation cone size	$\Delta R < 0.2$	$\Delta R < 0.2$
Calorimeter-based isolation requirement	$\sum E_T/p_T^e < 0.06$	$\sum E_T/p_T^\mu < 0.15$

Table 6.2: Truth-based isolation requirements for electrons and muons.

The truth-based isolation requirement reduces the top background by over 99%, and the percentage of the total background consisting of top events is reduced from 83% to 2%. Additional details on the truth-based isolation studies are presented in Appendix A.

---

1366 **6.4 Object and event selection**

1367 **6.4.1 Object selection**

1368 Electrons and muons are preselected to have  $p_T > 7$  and  $6$  GeV, respectively, and  $|\eta| \leq 4.0$ . The  
 1369 likelihood of a given lepton to pass the trigger and identification requirements is estimated by  
 1370 calculating an efficiency dependent on the  $p_T$  and  $\eta$  of the lepton. The leptons are also required to  
 1371 pass the isolation criteria detailed in Table 6.2. Jets that have been tagged as a fake electron by the  
 1372 functions described in Section 6.3 are treated as electrons for the purpose of the object selection and  
 1373 are subject to the same criteria. In order to be considered a signal lepton, an additional requirement  
 1374 of  $p_T > 25$  GeV is applied on top of the preselection. The two highest  $p_T$  leptons passing this  
 1375 selection are chosen to be the leading and subleading signal leptons.

1376 Jets are clustered using the anti- $k_t$  algorithm [44] from final-state particles within a radius of  
 1377  $\Delta R = 0.4$  (excluding muons and neutrinos). Jets are required to have  $p_T > 30$  GeV and lie within  
 1378  $|\eta| < 4.5$ , with an additional cut of  $p_T > 70$  GeV for jets above  $|\eta| \geq 3.8$  in order to suppress jets  
 1379 from pileup interactions. Jets overlapping with a preselected electron within  $\Delta R(e, j) < 0.05$  are  
 1380 removed in order to prevent double counting. The two highest  $p_T$  jets are defined as the leading  
 1381 and subleading *tag jets*.

1382 **6.4.2 Event selection**

1383 The default event selection is summarized in Table 6.3 and described here. Exactly two signal  
 1384 leptons are required with the same electric charge and separated from each other by  $\Delta R(l l) > 0.3$ .  
 1385 In order to suppress contributions from Drell-Yan backgrounds, the two signal leptons must have  
 1386 an invariant mass  $m_{ll}$  greater than  $20$  GeV. Additionally, if both signal leptons are electrons, their  
 1387 mass must be at least  $10$  GeV from the  $Z$ -boson mass in order to reduce background from  $Z$ -boson  
 1388 decays<sup>14</sup>. The event is required to have at least  $40$  GeV of missing transverse energy ( $E_T^{\text{miss}}$ ) to  
 1389 account for the two neutrinos from the  $W$  decays. Events with additional preselected leptons are  
 1390 vetoed, which greatly reduces  $WZ$  and  $ZZ$  backgrounds.

1391 Each event must have at least two jets, and both tag jets are required to not overlap with the  
 1392 signal leptons, and there is a veto on events with one or more  $b$ -jets. In order to preferentially select  
 1393 EWK production, the tag jets are also required to have a large separation between them and a large

---

<sup>14</sup>The electron charge misidentification rate in the upgraded ATLAS detector is estimated to be high enough that contributions from  $Z \rightarrow ee$  backgrounds are non-negligible.

<sup>1394</sup> invariant mass. Finally, a cut on the lepton centrality<sup>15</sup>,  $\zeta$ , defined in Equation 6.1 enhances the  
<sup>1395</sup> EWK  $W^\pm W^\pm jj$  signal.

$$\zeta = \min[\min(\eta_{\ell 1}, \eta_{\ell 2}) - \min(\eta_{j 1}, \eta_{j 2}), \max(\eta_{j 1}, \eta_{j 2}) - \max(\eta_{\ell 1}, \eta_{\ell 2})] \quad (6.1)$$

Selection requirement	Selection value
Lepton kinematics	$p_T > 25 \text{ GeV}$ $ \eta  \leq 4.0$
Jet kinematics	$p_T > 30 \text{ GeV}$ for $ \eta  \leq 4.5$ $p_T > 70 \text{ GeV}$ for $ \eta  > 3.8$
Dilepton charge	Exactly two signal leptons with same charge
Dilepton separation	$\Delta R_{l,l} \geq 0.3$
Dilepton mass	$m_{ll} > 20 \text{ GeV}$
$Z$ boson veto	$ m_{ee} - m_Z  > 10 \text{ GeV}$ ( $ee$ -channel only)
$E_T^{\text{miss}}$	$E_T^{\text{miss}} > 40 \text{ GeV}$
Jet selection	At least two jets with $\Delta R_{l,j} > 0.3$
$b$ jet veto	$N_{b\text{-jet}} = 0$
Dijet separation	$\Delta \eta_{jj} > 2.5$
Trilepton veto	No additional preselected leptons
Dijet mass	$m_{jj} > 500 \text{ GeV}$
Lepton-jet centrality	$\zeta > 0$

Table 6.3: Summary of the signal event selection.

## <sup>1396</sup> 6.5 Selection optimization

<sup>1397</sup> An upgraded detector along with an increase in center of mass energy and integrated luminosity  
<sup>1398</sup> provides an opportunity to study whether the event selection can be optimized to improve the signal  
<sup>1399</sup> to background ratio.

### <sup>1400</sup> 6.5.1 Random grid search algorithm

<sup>1401</sup> The chosen method for optimizing the event selection is a cut-based algorithm known as the Random  
<sup>1402</sup> Grid Search (RGS) [62]. Consider a simple case of two variables  $x$  and  $y$  chosen to differentiate signal  
<sup>1403</sup> from background. In order to be considered a signal event, a given event would be required to pass  
<sup>1404</sup> a set of selection criteria, called a *cut point*:  $c = \{x > x_c, y > y_c\}$ . A simple method to choose the  
<sup>1405</sup> optimal cut point (i.e. the “best” values of the cuts  $x_c$  and  $y_c$ ) would be to construct an  $n \times m$

---

<sup>15</sup> $\zeta$  is a measurement of whether the two signal leptons lie between the two tagging jets in  $\eta$ , as is preferred by the VBS topology.

1406 rectangular grid in  $x$  and  $y$  consisting of points  $(x_0, y_0), (x_1, y_1), \dots, (x_n, y_m)$ , as in Figure 6.3. One  
 1407 can then choose a cut point  $c_k = \{x > x_i, y > y_j\}$  that maximizes the signal significance as measured  
 1408 by a chosen metric. This would be considered a *rectangular grid search*.

1409 While effective in principle, a rectangular grid search comes with two major drawbacks:

- 1410 1. The algorithm scales exponentially as the number of variables to be optimized increases, as  
 1411 this is effectively increasing the dimensionality of the grid. In the simple case of a square grid  
 1412 with  $N$  bins per variable  $v$ , the number of cut points to be evaluated grows as  $N^v$ .
- 1413 2. Signal and background samples are rarely evenly distributed over the entire grid, resulting  
 1414 in many cut points being sub-optimal and evaluating them would be a waste of computing  
 1415 resources.

1416 To combat these limitations, the RGS algorithm constructs a grid of cut points directly from  
 1417 the signal sample itself. In the two-dimensional example, this means that the variables  $x_i$  and  $y_j$   
 1418 making up the cut point  $c_k = \{x > x_i, y > y_j\}$  take their values directly from a given signal event.  
 1419 This has the benefit of creating a *random grid* of cut points that is biased towards regions of high  
 1420 signal concentration by construction. This reduces the need for exponentially increasing numbers of  
 1421 cut points while ensuring that computing resources are not wasted in regions with few to no signal  
 1422 events. An example of the the two-dimensional random grid is shown in Figure 6.4.

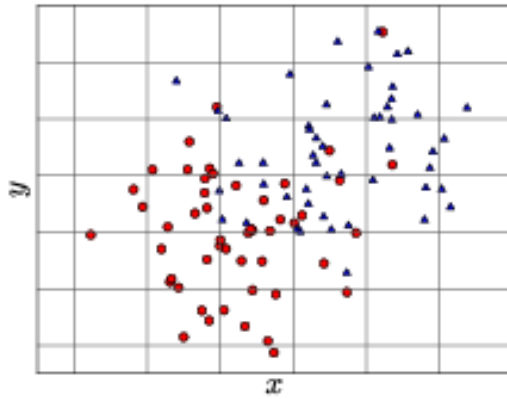


Figure 6.3: A visual representation of a rectangular grid search algorithm. The signal events are the blue triangles, and the red circles are the background events. **TODO: replace with own figure**

1423 Once the random grid of cut points is constructed, the optimal cut point can be chosen using any  
 1424 number of metrics, such as signal to background ratio. For the purpose of the  $W^\pm W^\pm jj$  upgrade

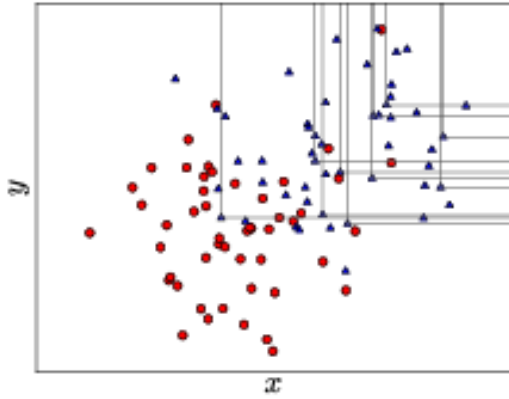


Figure 6.4: A visual representation of a random grid search algorithm. The signal events are the blue triangles, and the red circles are the background events. **TODO: replace with own figure**

study, the optimal cut point is chosen to be the one that maximizes the signal significance  $Z$  as defined in Equation 6.2 [63].

$$Z = \sqrt{2 \left[ (s + b) \ln \left( \frac{s + b}{b_0} \right) + b_0 - s - b \right] + \frac{(b - b_0)^2}{\sigma_b^2}} \quad (6.2)$$

where  $s$  and  $b$  are the number of signal and background events, respectively,  $\sigma_b$  is the total uncertainty on the background, and  $b_0$  is defined as:

$$b_0 = \frac{1}{2} \left( b - \sigma_b^2 + \sqrt{(b - \sigma_b^2)^2 + 4(s + b)\sigma_b^2} \right) \quad (6.3)$$

In the case where the background is known precisely (i.e.  $\sigma_b = 0$ ), Equation 6.2 simplifies to

$$Z = \sqrt{2 \left( b \left[ (1 + s/b) \ln(1 + s/b) - s/b \right] \right)} \quad (6.4)$$

which further reduces to the familiar  $Z = s/\sqrt{b}$  for the case when  $s \ll b$ .

### 6.5.2 Inputs to the optimization

In order to train the RGS, signal and background samples are prepared from events passing the event selection outlined in Table 6.3 up through the  $b$ -jet veto. The signal sample is chosen to be the longitudinally polarized  $W^\pm W^\pm jj$  EWK events, and the transverse and mixed polarizations are treated as background along with  $W^\pm W^\pm jj$  events from QCD interactions and the traditional backgrounds listed in Section 6.3. Splitting the inclusive  $W^\pm W^\pm jj$  EWK events by polarization

<sup>1437</sup> allows the optimization to favor the longitudinally polarized events as much as possible, even though  
<sup>1438</sup> they both contribute to the EWK signal.

<sup>1439</sup> The following variables are chosen for optimization:

- <sup>1440</sup> • Leading lepton  $p_T$
- <sup>1441</sup> • Dilepton invariant mass ( $m_{ll}$ )
- <sup>1442</sup> • Leading and subleading jet  $p_T$
- <sup>1443</sup> • Dijet invariant mass ( $m_{jj}$ )
- <sup>1444</sup> • Lepton-jet centrality ( $\zeta$ )

<sup>1445</sup> Subleading lepton  $p_T$  is omitted as it is desirable to keep the cut value as low as possible due to  
<sup>1446</sup> its sensitivity to the longitudinal polarization (as discussed in Section 6.1.1). Additionally, the dijet  
<sup>1447</sup> separation  $\Delta\eta_{jj}$  was included in the optimization originally, however it was dropped from the list due  
<sup>1448</sup> to the cut value being motivated by differences between EWK and QCD produced  $W^\pm W^\pm jj$  events.

<sup>1449</sup> Two additional constraints were imposed when selecting the optimal cut point:

- <sup>1450</sup> 1. At least 1000 signal events must survive in order to prevent the optimization from being too  
<sup>1451</sup> aggressive and unnecessarily reducing signal statistics.
- <sup>1452</sup> 2. The dijet invariant mass may only vary within a 50 GeV range of the default value (from  
<sup>1453</sup> 450 – 550 GeV) due to the cut being physically motivated by the VBS event topology (see  
<sup>1454</sup> Section 5.0.2).

<sup>1455</sup> Lastly, the signal significance is calculated without taking into account the uncertainty of the  
<sup>1456</sup> background using Equation 6.4. This is due to the fact that the statistical uncertainties of the fake  
<sup>1457</sup> electron and charge misidentification backgrounds are quite large, owing to poor MC statistics in a  
<sup>1458</sup> few of the samples. If Equation 6.2 were used instead, the optimization will cut unreasonably hard  
<sup>1459</sup> against these backgrounds. Since Monte Carlo statistics is not expected to be a limiting factor when  
<sup>1460</sup> this analysis is performed at the HL-LHC, it is more realistic to simply ignore these large statistical  
<sup>1461</sup> uncertainties for the purpose of the optimization.

### <sup>1462</sup> 6.5.3 Results of the optimization

<sup>1463</sup> Ultimately, the random grid is constructed from over 38,000 LL-polarized  $W^\pm W^\pm jj$  events in the  
<sup>1464</sup> six variables listed above. After applying the constraints, the optimal cut point reduces the total

background from 9900 to 2310 while reducing the signal from 3489 to 2958. This corresponds to an increase in signal significance from  $Z = 33.26$  to  $Z = 52.63$  as calculated by Equation 6.4. The updates to the event selection are listed in Table 6.4.

The large reduction in the background is primarily a result of the increase in the leading and subleading jet  $p_T$  from 30 GeV to 90 GeV and 45 GeV, respectively. As can be seen in Figure 6.7, this increase removes a significant portion of the backgrounds from jets faking electrons and charge mis-ID. Additionally, the loosening of the lepton-jet centrality cut  $\zeta$  allows more signal events to survive the event selection (see Figure 6.9). Other changes to the event selection are minor and do not individually have a large impact on the signal or background yields.

The full event yields after optimization as well as the cross section measurement are detailed alongside those using the default selection in Section 6.6.

**TODO:** It's a bit awkward to reference the results of the default/optimized before they're properly presented. Maybe move the sections around? not sure...

Selection requirement	Selection value
Lepton kinematics	$p_T > 28$ GeV (leading lepton only)
Jet kinematics	$p_T > 90$ GeV (leading jet) $p_T > 45$ GeV (subleading jet)
Dilepton mass	$m_{ll} > 28$ GeV
Dijet mass	$m_{jj} > 520$ GeV
Lepton-jet centrality	$\zeta > -0.5$

Table 6.4: Updates to the  $W^\pm W^\pm jj$  event selection criteria after optimization. Cuts not listed remain unchanged from the default selection in Table 6.3.

## 6.6 Results

### 6.6.1 Event yields

After applying the full event selection, the analysis is broken down into four channels based off of the flavor of the signal leptons:  $\mu\mu$ ,  $ee$ ,  $\mu e$ , and  $e\mu$ . The full signal and background event yields are shown in Table 6.5 for each channel separately and combined using the default event selection. 3489 EWK  $W^\pm W^\pm jj$  events are expected compared to 9900 background events. The dominant sources of background are jets faking electrons followed by charge misidentification and diboson processes. Triboson events, QCD  $W^\pm W^\pm jj$ , and other non-prompt sources make up approximately 5% of the total background combined.

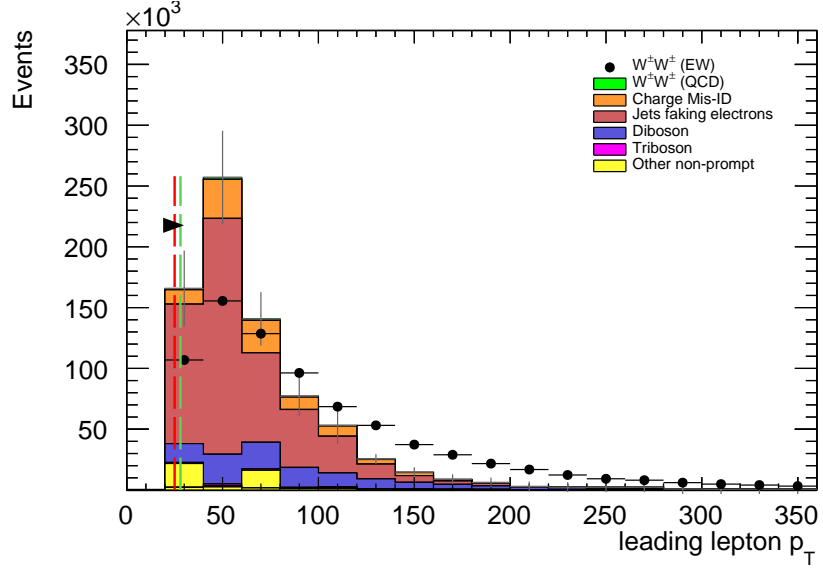


Figure 6.5: Leading lepton  $p_T$  distribution. The default and optimized cuts are represented by the red and green dashed lines, respectively. The  $W^\pm W^\pm jj$  signal (black points) is normalized to the same area as the sum of the backgrounds (colored histogram). **TODO: Move to appendix or omit**

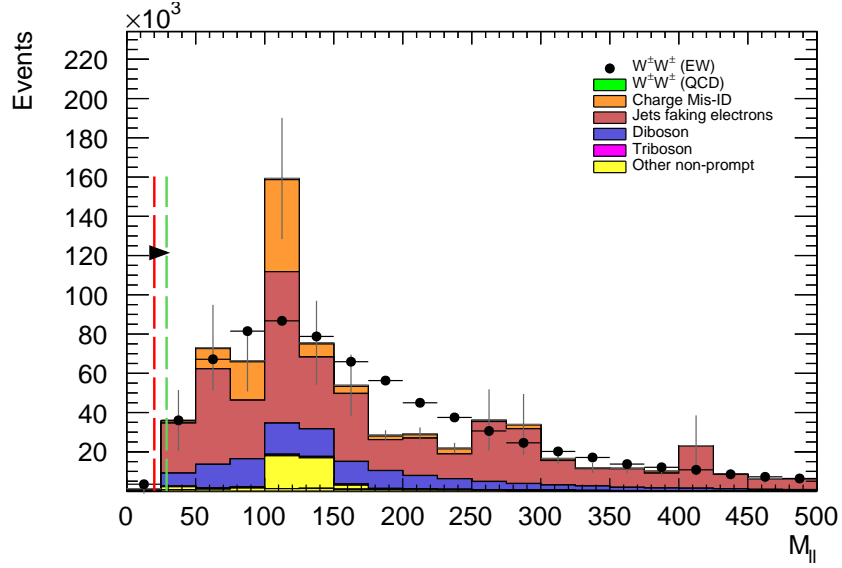


Figure 6.6: Dilepton invariant mass distribution. The default and optimized cuts are represented by the red and green dashed lines, respectively. The  $W^\pm W^\pm jj$  signal (black points) is normalized to the same area as the sum of the backgrounds (colored histogram). **TODO: Move to appendix or omit**

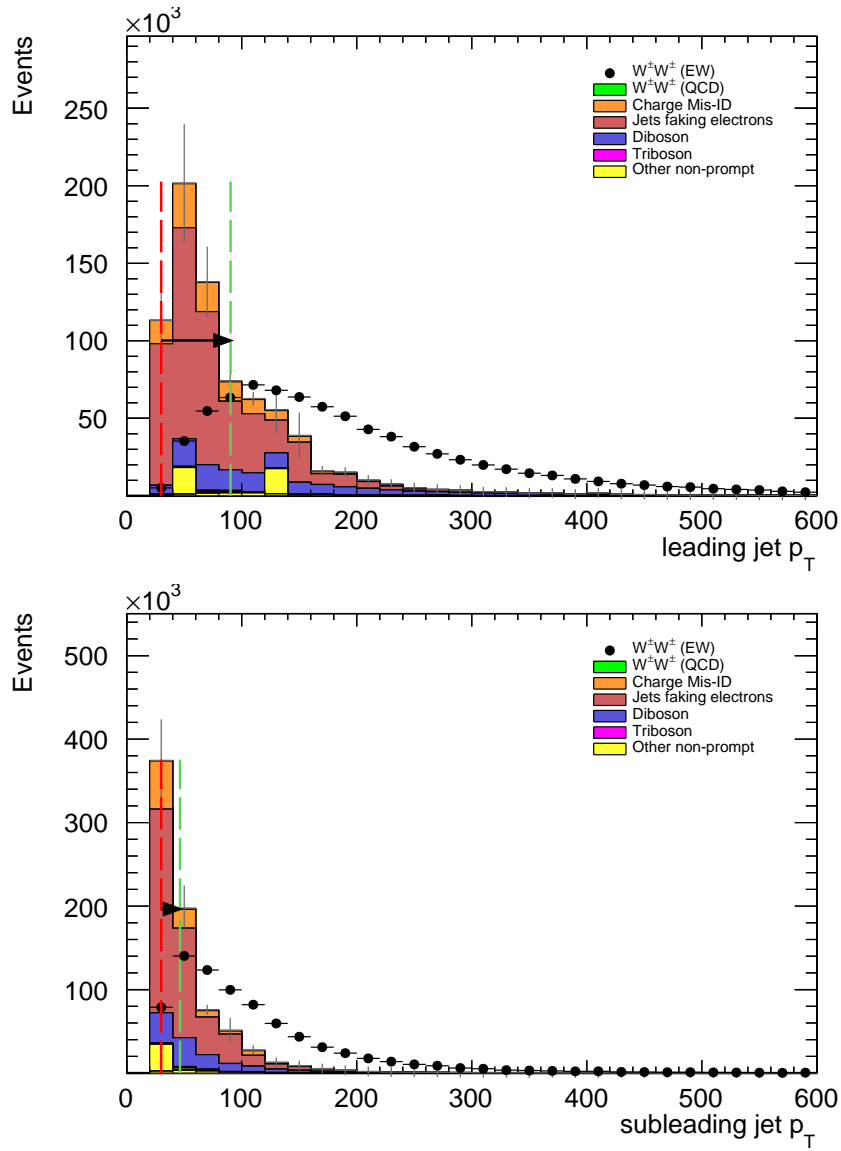


Figure 6.7: Leading (top) and subleading (bottom) jet  $p_T$  distributions. The default and optimized cuts are represented by the red and green dashed lines, respectively. The  $W^\pm W^\pm jj$  EWK signal (black points) is normalized to the same area as the sum of the backgrounds (colored histogram).

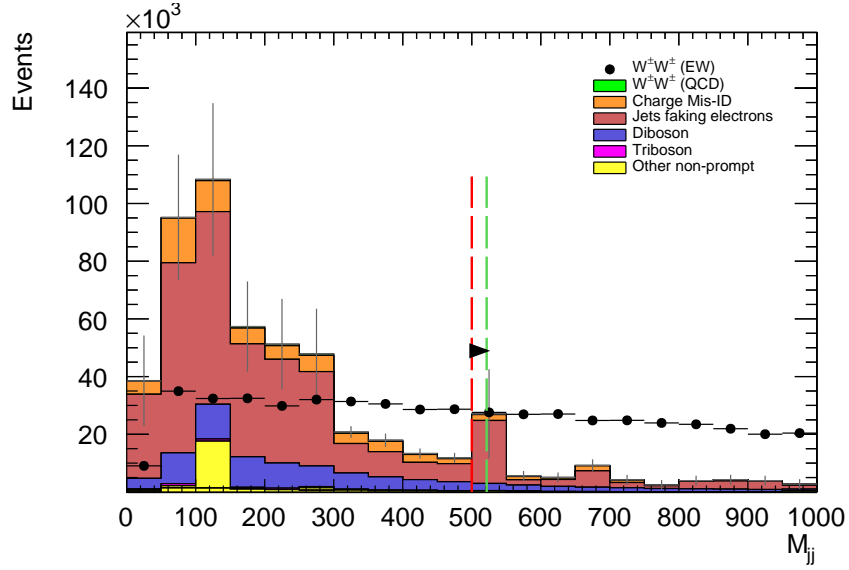


Figure 6.8: Dijet invariant mass distribution. The default and optimized cuts are represented by the red and green dashed lines, respectively. The  $W^\pm W^\pm jj$  EWK signal (black points) is normalized to the same area as the sum of the backgrounds (colored histogram). **TODO:** Move to appendix or omit

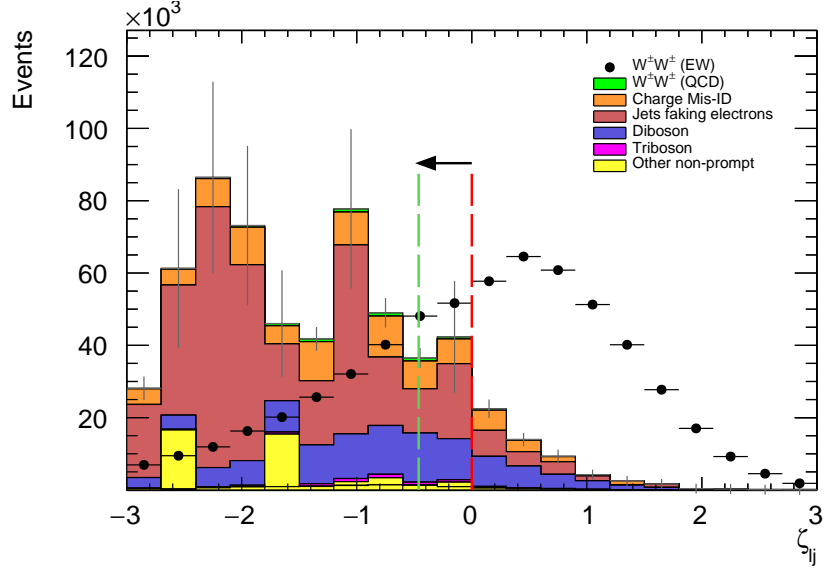


Figure 6.9: Lepton-jet centrality distribution. The default and optimized cuts are represented by the red and green dashed lines, respectively. The  $W^\pm W^\pm jj$  EWK signal (black points) is normalized to the same area as the sum of the backgrounds (colored histogram).

	All channels	$\mu\mu$	$ee$	$\mu e$	$e\mu$
$W^\pm W^\pm jj$ (QCD)	206.4	91.1	22.8	38.4	54.1
Charge Misidentification	2300	0.0	2100	90	160
Jets faking electrons	5000	0.0	3400	1200	340
$WZ + ZZ$	2040	500	438	423	680
Tribosons	115	47	15.4	21.6	31.2
Other non-prompt	210	110	20	60	27
Total Background	9900	750	6000	1900	1290
Signal $W^\pm W^\pm jj$ (EWK)	3489	1435	432	679	944

Table 6.5: Signal and background event yields using the default event selection for an integrated luminosity of  $\mathcal{L} = 3000 \text{ fb}^{-1}$ . Events containing a fake or charge-flipped electron are removed from their respective sources and combined into a single entry each.

1487     The event yields for the optimized selection detailed in Section 6.5.3 are listed in Table 6.6. After  
 1488 optimization, 2958 signal events and just 2310 background events are expected. Diboson events are  
 1489 now the primary source of background, as the optimization greatly reduces the fake and charge  
 1490 misidentification backgrounds. As discussed earlier, the increase in the leading and subleading jet  
 1491  $p_T$  cuts as well as the loosening of the centrality cut are most responsible for the changes in the  
 1492 signal and background yields; distributions of these quantities using the default and the optimized  
 1493 event selections can be found in Figures 6.10, 6.11, and 6.12, respectively.

	All channels	$\mu\mu$	$ee$	$\mu e$	$e\mu$
$W^\pm W^\pm jj$ (QCD)	168.7	74.6	19.7	32.2	42.2
Charge Misidentification	200	0.0	11	30	160
Jets faking electrons	460	0.0	130	260	70
$WZ + ZZ$	1286	322	289	271	404
Tribosons	76	30.1	9.6	15.1	21.6
Other non-prompt	120	29	16.6	50	19
Total Background	2310	455	480	660	710
Signal $W^\pm W^\pm jj$ (EWK)	2958	1228	380	589	761

Table 6.6: Signal and background event yields using the optimized event selection for an integrated luminosity of  $\mathcal{L} = 3000 \text{ fb}^{-1}$ . Events containing a fake or charge-flipped electron are removed from their respective sources and combined into a single entry each.

1494     It is important to note, however, that the MC sample used to estimate  $Z + \text{jets}$  events suffers from  
 1495 poor statistics which results in large per-event weights once scaled to  $\mathcal{L} = 3000 \text{ fb}^{-1}$ . This sample  
 1496 contributes heavily to the fake and charge misidentification backgrounds, and a handful of these  
 1497 events being cut out by the optimization contributes has a large effect on the dramatic reduction  
 1498 of these backgrounds. As a result, these particular optimized results are likely overly optimistic.  
 1499 However, given proper MC statistics, it is still expected that the optimization will outperform the

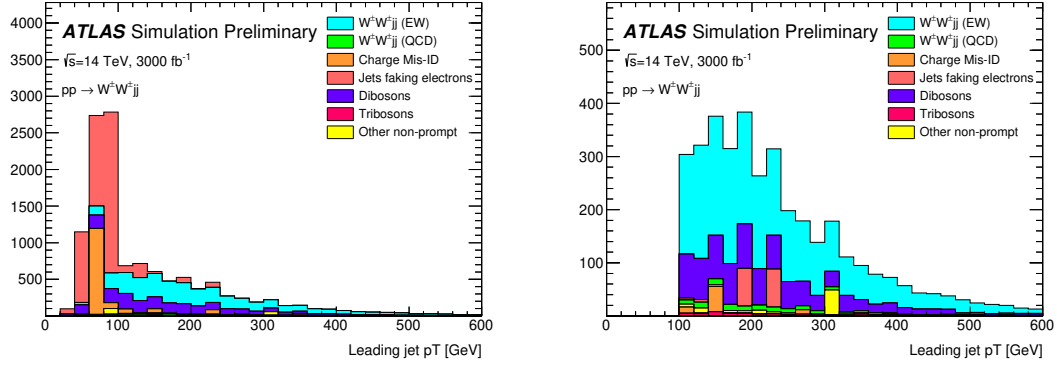


Figure 6.10:  $p_T$  distributions for the leading jet using the default (left) and optimized (right) event selections for all channels combined.

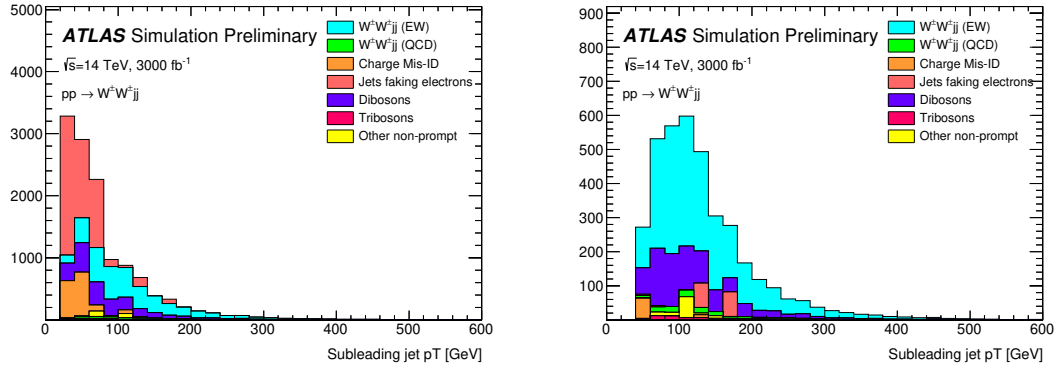


Figure 6.11:  $p_T$  distributions for the subleading jet using the default (left) and optimized (right) event selections for all channels combined.

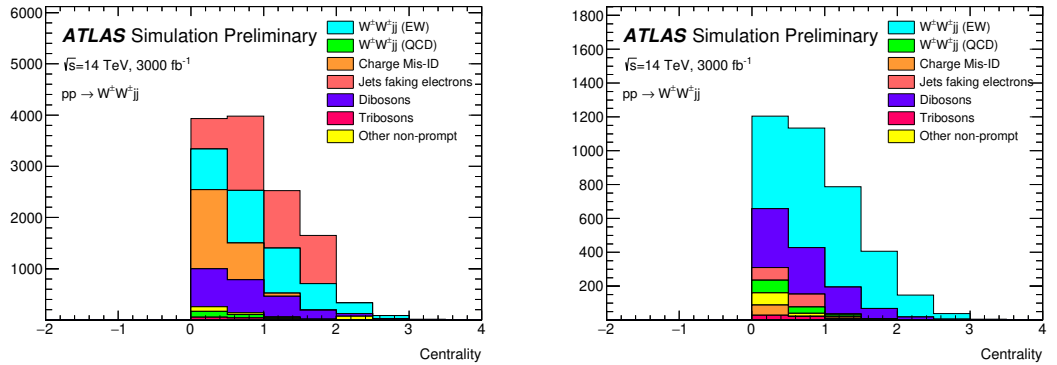


Figure 6.12:  $p_T$  distributions for lepton-jet centrality  $\zeta$  using the default (left) and optimized (right) event selections for all channels combined.

1500 default selection.

### 1501 6.6.2 Uncertainties

1502 TODO: Ask for details on how some of these uncertainties were calculated – specifically the fakes and  
 1503 charge mis-ID The uncertainties considered for the analysis are summarized in Table 6.7. Values for  
 1504 experimental systematics on the trigger efficiency, lepton and jet reconstruction, and flavor tagging  
 1505 are taken directly from the 13 TeV analysis [1]. The rate uncertainties for the background processes  
 1506 are halved from the 13 TeV values.

Source	Uncertainty (%)
$W^\pm W^\pm jj$ (EWK)	3
Luminosity	1
Trigger efficiency	0.5
Lepton reconstruction and identification	1.8
Jets	2.3
Flavor tagging	1.8
Jets faking electrons	20
Charge misidentification	25
$W^\pm W^\pm jj$ (QCD)	20
Top	15
Diboson	10
Triboson	15

Table 6.7: Summary of estimated experimental and rate uncertainties.

### 1507 6.6.3 Cross section measurement

1508 The cross section is calculated using the same method as in the 13 TeV analysis, detailed in Chap-  
 1509 ter 5. TODO: update from chapter reference to subsection reference (once it's written)... Once  
 1510 again, each of the four lepton flavor channels is further split by charge (i.e.  $\mu\mu \rightarrow \mu^+\mu^+ + \mu^-\mu^-$ ),  
 1511 as this increases the sensitivity of the analysis. Each channel's  $m_{jj}$  distribution is combined in a  
 1512 profile likelihood fit to extract the EWK  $W^\pm W^\pm jj$  production cross section. The expected cross  
 1513 section calculated using the default event selection is:

$$\sigma_{W^\pm W^\pm jj}^{\text{expected}} = 16.89 \pm 0.36 \text{ (stat)} \pm 0.53 \text{ (theory)} \pm 0.84 \text{ (syst)} \text{ fb} \quad (6.5)$$

1514 The expected cross section calculated using the optimized event selection is:

$$\sigma_{W^\pm W^\pm jj}^{\text{expected}} = 16.94 \pm 0.36 \text{ (stat)} \pm 0.53 \text{ (theory)} \pm 0.78 \text{ (syst)} \text{ fb} \quad (6.6)$$

1515 The optimized selection should not change the measured value of the cross section, and indeed both  
 1516 are consistent with within uncertainties. The systematic uncertainty is reduced by approximately 7%  
 1517 with the optimized selection. Projections of the total uncertainty on the cross section as a function  
 1518 of integrated luminosity made by [TODO: how was this made?](#) is shown in Figure 6.13. As the  
 1519 integrated luminosity increases past  $\mathcal{L} > 3000 \text{ fb}^{-1}$ , the statistical uncertainty reduces faster than  
 1520 the systematic uncertainties. However, the total uncertainty is expected to reduce by less than a  
 1521 percent with increased luminosity past the planned 3000  $\text{fb}^{-1}$ .

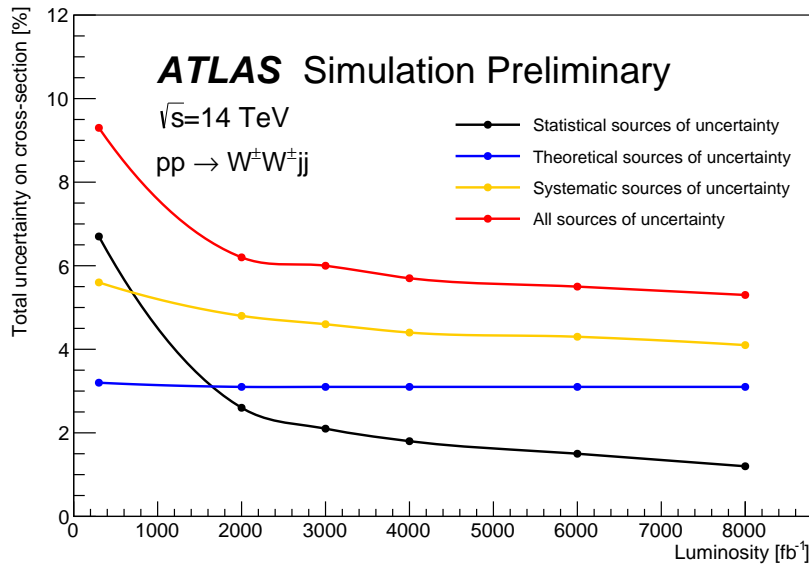


Figure 6.13: Projections of the statistical (black), theoretical (blue), systematic (yellow), and total (red) uncertainties on the measured cross section as a function of integrated luminosity using the optimized event selection.

#### 1522 6.6.4 Longitudinal scattering significance

1523 [TODO: get some details on how this was all done...](#) The longitudinal scattering significance is  
 1524 extracted from the  $|\Delta\phi_{jj}|$  distribution using a simultaneous binned likelihood fit. In order to increase  
 1525 sensitivity, the  $|\Delta\phi_{jj}|$  distribution was split into two bins in  $m_{jj}$ , and an additional cut on the  
 1526 pseudorapidity of the subleading lepton was applied ( $|\eta| < 2.5$ ) to reduce background from fake and  
 1527 charge misidentification. The  $|\Delta\phi_{jj}|$  distributions used in the fit are shown in Figure 6.14. Due to  
 1528 limited statistics, the four lepton flavor channels were not split by charge. The expected significance

1529 of the  $W_L^\pm W_L^\pm jj$  process is  $1.8\sigma$  with a precision of 47% on the measurement. Projections of the  
1530 expected significance as a function of integrated luminosity is shown in Figure 6.15.

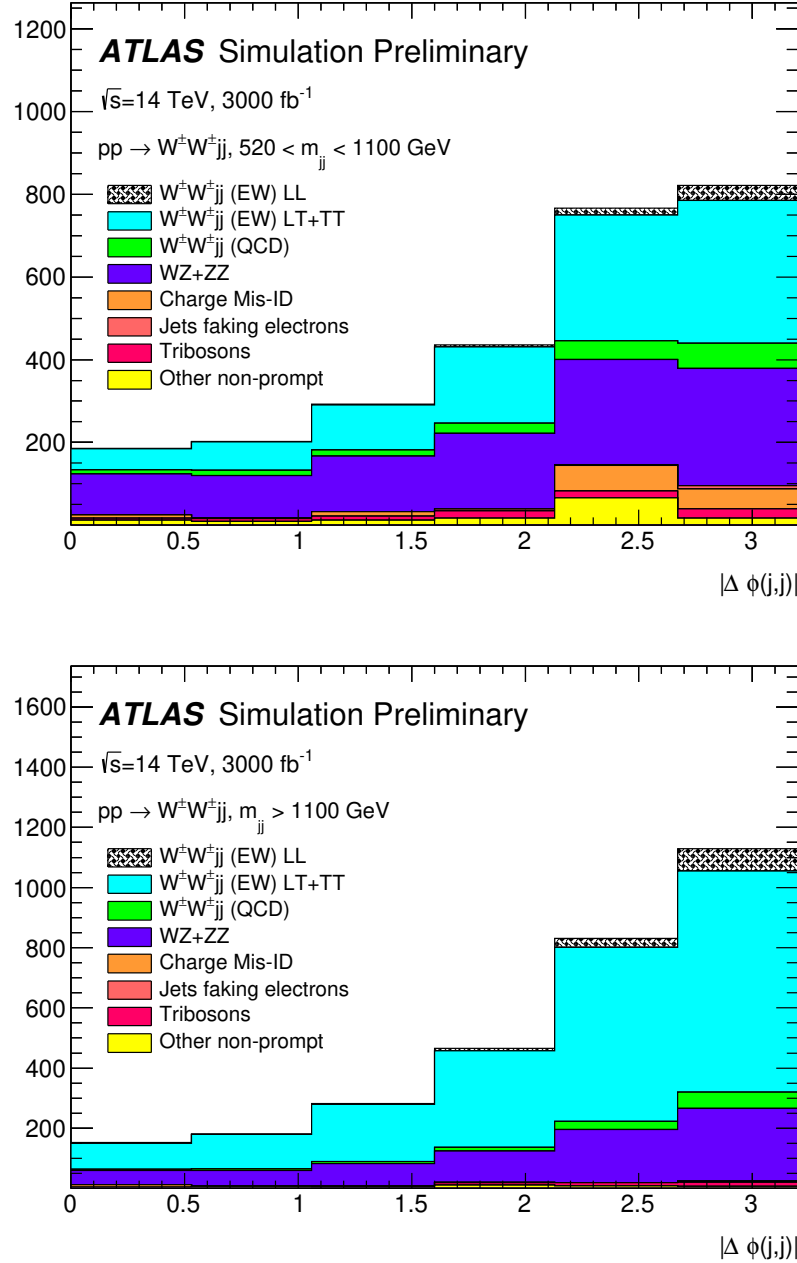


Figure 6.14: Dijet azimuthal separation ( $|\Delta\phi_{jj}|$ ) for the low  $m_{jj}$  region ( $520 < m_{jj} < 1100 \text{ GeV}$ , top) and the high  $m_{jj}$  region ( $m_{jj} > 1100 \text{ GeV}$ , bottom). The purely longitudinal (LL, gray) is plotted separately from the mixed and transverse (LT+TT, cyan) polarizations.

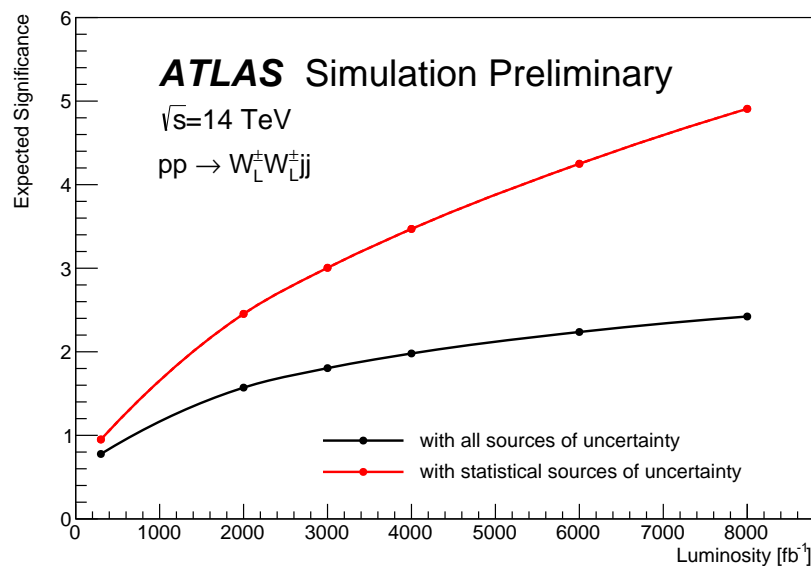


Figure 6.15: Projections of the expected longitudinal scattering significance as a function of integrated luminosity when considering all sources of uncertainties (black) or only statistical uncertainties (red).

1531

## CHAPTER 7

---

1532

## Conclusion

---

1533 Here's where you wrap it up.

1534 **Looking Ahead**

1535

1536 Here's an example of how to have an "informal subsection".

## APPENDIX A

### Additional material on truth isolation

yields by type	all channels	$\mu\mu$	$ee$	$\mu e$	$e\mu$
signal	4011	1583.2	531.7	793.1	1103.1
ww qcd	252.6	105.8	30.4	48	68.4
charge flip	2528.4	0.0	2075.4	255.1	197.8
fakes	7135.4	0.0	4675.1	1904.3	555.9
diboson	2370.4	581.2	491.8	517.9	779.6
triboson	125.5	49.1	17.8	24.6	34.1
top	90150.5	26618	15301.6	25277.9	22953.1
z+jets	241.2	0.0	0.0	0.0	241.2
w+jets	31.4	3.9	7.6	13.2	6.7
total bkg	102803.9	27354	22592	28027.8	24830.1
signal	4011	1583.2	531.7	793.1	1103.1

Table A.1: Event yields prior to applying any form of truth-based isolation criteria.

yields by type	all channels	$\mu\mu$	$ee$	$\mu e$	$e\mu$
signal	3470.5	1427.3	428.8	675.8	938.7
ww qcd	205.8	90.8	22.7	38.3	54
charge flip	2398.3	0.0	2104.6	95.8	197.9
fakes	4309.7	0.0	3390.6	750.8	168.3
diboson	1552.4	311.3	355.6	346.8	538.7
triboson	115	46.8	15.4	21.6	31.2
top	156.9	42.3	14.8	76.6	23.3
z+jets	0.0	0.0	0.0	0.0	0.0
w+jets	0.3	0.0	0.0	0.3	0.0
total bkg	8738.1	491.3	5903.7	1329.8	1013.4
signal	3470.5	1427.3	428.8	675.8	938.7

Table A.2: Event yields after applying a test version of the truth-based isolation.

TODO: Add tables for tight vs loose working point, information on the necessity of TRUTH1++

1540

## APPENDIX B

1541

1542

# Additional material on $W^\pm W^\pm jj$ measurement at $\sqrt{s} = 13$ TeV

### 1543 B.1 Impact of experimental uncertainty on MC background estimations

$W^\pm W^\pm jj$ QCD	$ee$ % Yield	$e\mu$ % Yield	$\mu\mu$ % Yield
Jet-related Uncertainties	3.41	3.04	2.85
b-tagging efficiency	2.56	2.48	2.48
Pile-up	4.99	0.45	0.33
Trigger efficiency	0.02	0.08	0.41
Lepton reconstruction/ID	1.62	1.19	1.89
MET reconstruction	0.41	0.22	0.34

Table B.1: Experimental systematics uncertainties for the  $W^\pm W^\pm jj$  QCD processes in all channels.

Triboson	$ee$ % Yield	$e\mu$ % Yield	$\mu\mu$ % Yield
Jet-related Uncertainties	13.09	13.39	16.85
b-tagging efficiency	2.96	3.77	4.95
Pile-up	19.37	24.66	6.87
Trigger efficiency	0.02	0.07	0.47
Lepton reconstruction/ID	1.66	1.27	2.48
MET reconstruction	0.00	0.46	0.00

Table B.2: Experimental systematics uncertainties for triboson process in all channels.

1544

plots go here

$t\bar{t}V$	$ee$ % Yield	$e\mu$ % Yield	$\mu\mu$ % Yield
Jet-related Uncertainties	17.65	11.97	14.27
b-tagging efficiency	15.02	9.04	13.83
Pile-up	8.73	10.69	4.18
Trigger efficiency	0.03	0.08	0.39
Lepton reconstruction/ID	2.57	3.27	2.66
MET reconstruction	1.75	4.16	1.62

Table B.3: Experimental systematics uncertainties for  $t\bar{t}V$  processes in all channels.

$W\gamma$	$ee$ % Yield	$e\mu$ % Yield	$\mu\mu$ % Yield
Jet-related Uncertainties	7.05	33.36	—
b-tagging efficiency	1.97	2.94	—
Pile-up	4.11	14.17	—
Trigger efficiency	0.01	0.14	—
Lepton reconstruction/ID	1.40	1.13	—
MET reconstruction	0.00	0.00	—

Table B.4: Experimental systematics uncertainties for the  $W\gamma$  process in all channels.

$Z\gamma$	$ee$ % Yield	$e\mu$ % Yield	$\mu\mu$ % Yield
Jet-related Uncertainties	16.22	370.44	—
b-tagging efficiency	1.08	3.10	—
Pile-up	12.57	11.51	—
Trigger efficiency	0.02	0.07	—
Lepton reconstruction/ID	1.26	22.01	—
MET reconstruction	0.00	0.00	—

Table B.5: Experimental systematics uncertainties for the  $Z\gamma$  process in all channels.

$ZZ$	$ee$ % Yield	$e\mu$ % Yield	$\mu\mu$ % Yield
Jet-related Uncertainties	15.71	15.76	35.18
b-tagging efficiency	2.23	2.35	2.89
Pile-up	1.22	3.20	4.58
Trigger efficiency	0.03	0.10	0.36
Lepton reconstruction/ID	3.59	3.10	5.70
MET reconstruction	4.84	3.26	3.24

Table B.6: Experimental systematics uncertainties for the  $ZZ$  process in all channels.

---

## Bibliography

---

- 1546 [1] ATLAS Collaboration Collaboration, *Observation of electroweak production of a same-sign W*  
 1547 *boson pair in association with two jets in pp collisions at  $\sqrt{s} = 13$  TeV with the ATLAS*  
 1548 *detector*, Tech. Rep. ATLAS-CONF-2018-030, CERN, Geneva, Jul, 2018.  
 1549 <https://cds.cern.ch/record/2629411>. (document), 5, 5.8, 6.6.2
- 1550 [2] S. L. Glashow, *The Renormalizability of Vector Meson Interactions*, Nucl. Phys. **10** (1959)  
 1551 **107–117**. 2.2
- 1552 [3] A. Salam and J. C. Ward, *Weak and Electromagnetic Interactions*, Nuovo Cimento **11** (1959)  
 1553 **568–577**. 2.2
- 1554 [4] L. R. Evans and P. Bryant, *LHC Machine*, JINST **3** (2008) S08001.  
 1555 <https://cds.cern.ch/record/1129806>. This report is an abridged version of the LHC  
 1556 Design Report (CERN-2004-003). 3.1
- 1557 [5] ATLAS Collaboration, *The ATLAS Experiment at the CERN Large Hadron Collider*, JINST  
 1558 **3** (2008) S08003. 3.1
- 1559 [6] ATLAS Collaboration, *ATLAS inner detector: Technical Design Report, Vol. 1*. CERN,  
 1560 Geneva, 1997. <https://cds.cern.ch/record/331063>. 4
- 1561 [7] P. F. kesson, T. Atkinson, M. J. Costa, M. Elsing, S. Fleischmann, A. N. Gaponenko,  
 1562 W. Liebig, E. Moyse, A. Salzburger, and M. Siebel, *ATLAS Tracking Event Data Model*,  
 1563 Tech. Rep. ATL-SOFT-PUB-2006-004. ATL-COM-SOFT-2006-005.  
 1564 CERN-ATL-COM-SOFT-2006-005, CERN, Geneva, Jul, 2006.  
 1565 <https://cds.cern.ch/record/973401>. 4.1
- 1566 [8] P. Brckman, A. Hicheur, and S. J. Haywood, *Global chi2 approach to the Alignment of the*  
 1567 *ATLAS Silicon Tracking Detectors*, Tech. Rep. ATL-INDET-PUB-2005-002.  
 1568 ATL-COM-INDET-2005-004. CERN-ATL-INDET-PUB-2005-002, CERN, Geneva, 2005.  
 1569 <https://cds.cern.ch/record/835270>. 4.1, 4.1
- 1570 [9] ATLAS Collaboration Collaboration, *Alignment of the ATLAS Inner Detector Tracking*  
 1571 *System with 2010 LHC proton-proton collisions at  $\sqrt{s} = 7$  TeV*, Tech. Rep.  
 1572 ATLAS-CONF-2011-012, CERN, Geneva, Mar, 2011.  
 1573 <https://cds.cern.ch/record/1334582>. 4.1

- 1574 [10] R. Hrtel and S. Bethke, *Iterative local Chi<sup>2</sup> alignment approach for the ATLAS SCT detector*,  
 1575 Nov, 2005. <http://cds.cern.ch/record/1511044>. Presented 28 Nov 2005. 4.1
- 1576 [11] ATLAS Collaboration Collaboration, P. Brckman de Renstrom, *Alignment strategy for the  
 1577 Inner Detector of ATLAS*, . <https://cds.cern.ch/record/1047114>. 4.1
- 1578 [12] *Alignment of the ATLAS Inner Detector and its Performance in 2012*, Tech. Rep.  
 1579 ATLAS-CONF-2014-047, CERN, Geneva, Jul, 2014.  
 1580 <https://cds.cern.ch/record/1741021>. 4.1
- 1581 [13] J. Alison and I. J. Kroll, *The Road to Discovery: Detector Alignment, Electron Identification,  
 1582 Particle Misidentification, WW Physics, and the Discovery of the Higgs Boson*, Dec, 2015.  
 1583 <https://cds.cern.ch/record/1536507>. Presented 08 Nov 2012. 4
- 1584 [14] ATLAS Collaboration, ATLAS Collaboration, *Evidence for Electroweak Production  
 1585 of  $W^\pm W^\pm jj$  in  $pp$  Collisions at  $\sqrt{s} = 8$  TeV with the ATLAS Detector*, *Phys. Rev. Lett.* **113**  
 1586 (2014) no. 14, 141803, arXiv:1405.6241 [hep-ex]. 5
- 1587 [15] CMS Collaboration, V. Khachatryan et al., *Study of vector boson scattering and search for  
 1588 new physics in events with two same-sign leptons and two jets*, *Phys. Rev. Lett.* **114** (2015)  
 1589 no. 5, 051801, arXiv:1410.6315 [hep-ex]. 5
- 1590 [16] CMS Collaboration, CMS Collaboration, *Observation of electroweak production of same-sign  
 1591 W boson pairs in the two jet and two same-sign lepton final state in proton-proton collisions  
 1592 at  $\sqrt{s} = 13$  TeV*, arXiv:1709.05822 [hep-ex]. 5
- 1593 [17] C. Bittrich, W. K. Di Clemente, E. M. Duffield, C. Geng, G. Gonella, J. Guo, B. Heinemann,  
 1594 T. Herrmann, F. Iltzsche Speiser, M. Kobel, K. Koeneke, J. I. Kroll, S. Li, J. Liu, Y. Liu, J. A.  
 1595 Manjarres Ramos, G. Azuelos, C. A. Lee, M. Mittal, C. Mwewa, R. Ospanov, S. Pagan Griso,  
 1596 K. J. Potamianos, M. Shapiro, P. Sommer, S. Todt, Y. Wu, W. Xu, S. Yacoob, H. Yang,  
 1597 L. Zhang, Z. Zhao, B. Zhou, J. Zhu, and M.-A. Pleier, *Support note for measurement of  
 1598 electroweak  $W^\pm W^\pm jj$  production at  $\sqrt{s} = 13$  TeV*, Tech. Rep. ATL-COM-PHYS-2018-252,  
 1599 CERN, Geneva, Mar, 2018. <https://cds.cern.ch/record/2309552>. 5, 5.3.3, 2, 4, 5.4.3
- 1600 [18] B. W. Lee, C. Quigg, and H. B. Thacker, *The Strength of Weak Interactions at Very  
 1601 High-Energies and the Higgs Boson Mass*, *Phys. Rev. Lett.* **38** (1977) 883–885. 5.0.1
- 1602 [19] S. D. Rindani, *Strong gauge boson scattering at the LHC*, in *Physics at the Large Hadron  
 1603 Collider*, A. Datta, B. Mukhopadhyaya, A. Raychaudhuri, A. K. Gupta, C. L. Khetrapal,  
 1604 T. Padmanabhan, and M. Vijayan, eds., pp. 145–155. 2009. arXiv:0910.5068 [hep-ph]. 5.0.1
- 1605 [20] A. Alboteanu, W. Kilian, and J. Reuter, *Resonances and Unitarity in Weak Boson Scattering  
 1606 at the LHC*, *JHEP* **11** (2008) 010, arXiv:0806.4145 [hep-ph]. 5.0.1, 5.1
- 1607 [21] ATLAS Collaboration, *Observation of a new particle in the search for the Standard Model  
 1608 Higgs boson with the ATLAS detector at the LHC*, *Phys. Lett. B* **716** (2012) 1,  
 1609 arXiv:1207.7214 [hep-ex]. 5.0.1
- 1610 [22] CMS Collaboration, *Observation of a new boson at a mass of 125 GeV with the CMS  
 1611 experiment at the LHC*, *Phys. Lett. B* **716** (2012) 30, arXiv:1207.7235 [hep-ex]. 5.0.1
- 1612 [23] J. M. Campbell and R. K. Ellis, *Higgs Constraints from Vector Boson Fusion and Scattering*,  
 1613 *JHEP* **04** (2015) 030, arXiv:1502.02990 [hep-ph]. 5.0.1, 5.0.2

- 1614 [24] M. SZleper, *The Higgs boson and the physics of WW scattering before and after Higgs*  
 1615 *discovery*, arXiv:1412.8367 [hep-ph]. 5.0.1
- 1616 [25] E. Accomando, A. Ballestrero, A. Belhouari, and E. Maina, *Isolating Vector Boson Scattering*  
 1617 *at the LHC: Gauge cancellations and the Equivalent Vector Boson Approximation vs complete*  
 1618 *calculations*, Phys. Rev. **D74** (2006) 073010, arXiv:hep-ph/0608019 [hep-ph]. 5.0.1
- 1619 [26] P. Anger, B. Axen, T. Dai, C. Gumpert, C. Hasterok, B. Heinemann, M. Hurwitz, N. Ilic,  
 1620 M. Kobel, J. Liu, L. Liu, J. Metcalfe, S. Pagan Griso, B. Zhou, S. Hou, M.-A. Pleier,  
 1621 U. Schnoor, J. Searcy, F. Socher, A. Sood, A. Vest, L. Xu, and J. Zhu, *Same Sign  $W^\pm W^\pm$*   
 1622 *Production and Limits on Anomalous Quartic Gauge Couplings*, Tech. Rep.  
 1623 ATL-COM-PHYS-2013-990, CERN, Geneva, Jul, 2013.  
 1624 <https://cds.cern.ch/record/1561731>. Internal note for approved paper STDM-2013-06  
 1625 <https://atlas.web.cern.ch/Atlas/GROUPS/PHYSICS/PAPERS/STDM-2013-06/>. 5.0.2, 5.1,  
 1626 5.7
- 1627 [27] J. Almond, L. Bianchini, C. Blocker, J. Klinger, A. Maslennikov, M. Owen, K. Skovpen,  
 1628 Y. Tikhonov, and U. Yang, *Search for heavy neutrino,  $W_R$  and  $Z_R$  gauge bosons in events*  
 1629 *with two high- $P_T$  leptons and jets with the ATLAS detector in pp collisions at  $\sqrt{s} = 8$  TeV*,  
 1630 Tech. Rep. ATL-COM-PHYS-2013-810, CERN, Geneva, Jun, 2013.  
 1631 <https://cds.cern.ch/record/1555805>. This is the supporting note for EXOT-2012-24,  
 1632 which is now published as JHEP07 (2015) 162. 5.0.3
- 1633 [28] ATLAS Collaboration, M. Aaboud et al., *Luminosity determination in pp collisions at  $\sqrt{s} = 8$  TeV using the ATLAS detector at the LHC*, Eur. Phys. J. **C76** (2016) no. 12, 653,  
 1634 arXiv:1608.03953 [hep-ex]. 5.1
- 1635 [29] G. Avoni et al., *The new LUCID-2 detector for luminosity measurement and monitoring in*  
 1637 *ATLAS*, JINST **13** (2018) no. 07, P07017. 5.1
- 1638 [30] ATLAS Collaboration, G. Aad et al., *The ATLAS Simulation Infrastructure*, Eur. Phys. J.  
 1639 **C70** (2010) 823–874, arXiv:1005.4568 [physics.ins-det]. 5.1.1
- 1640 [31] S. Agostinelli et al., *GEANT4 - a simulation toolkit*, Nucl. Instrum. Meth. **A506** (2003)  
 1641 250–303. 5.1.1
- 1642 [32] T. Sjostrand, S. Mrenna, and P. Skands, *A Brief Introduction to PYTHIA 8.1*, Comput.  
 1643 Phys. Commun. **178** (2008) 852–867, arXiv:0710.3820 [hep-ph]. 5.1.1
- 1644 [33] T. Gleisberg et al., *Event generation with SHERPA 1.1*, JHEP **02** (2009) 007,  
 1645 arXiv:0811.4622 [hep-ph]. 5.1.1
- 1646 [34] S. Schumann and F. Krauss, *A parton shower algorithm based on Catani-Seymour dipole*  
 1647 *factorization*, JHEP **03** (2008) 038, arXiv:0709.1027 [hep-ph]. 5.1.1
- 1648 [35] S. Höche, F. Krauss, S. Schumann, and F. Siegert, *QCD matrix elements and truncated*  
 1649 *showers*, JHEP **05** (2009) 053, arXiv:0903.1219 [hep-ph]. 5.1.1
- 1650 [36] R. D. Ball et al., *Parton distributions for the LHC Run II*, JHEP **04** (2015) 040,  
 1651 arXiv:1410.8849 [hep-ph]. 5.1.1
- 1652 [37] S. Alioli, P. Nason, C. Oleari, and E. Re, *A general framework for implementing NLO*  
 1653 *calculations in shower Monte Carlo programs: the POWHEG BOX*, JHEP **06** (2010) 043,  
 1654 arXiv:1002.2581 [hep-ph]. 5.1.1

- 1655 [38] A. Ballestrero et al., *Precise predictions for same-sign W-boson scattering at the LHC*, Eur.  
 1656 Phys. J. **C78** (2018) no. 8, 671, arXiv:1803.07943 [hep-ph]. 5.1.1
- 1657 [39] J. Alwall, R. Frederix, S. Frixione, V. Hirschi, F. Maltoni, O. Mattelaer, H. S. Shao,  
 1658 T. Stelzer, P. Torrielli, and M. Zaro, *The automated computation of tree-level and*  
 1659 *next-to-leading order differential cross sections, and their matching to parton shower*  
 1660 *simulations*, JHEP **07** (2014) 079, arXiv:1405.0301 [hep-ph]. 5.1.1
- 1661 [40] H.-L. Lai, M. Guzzi, J. Huston, Z. Li, P. M. Nadolsky, J. Pumplin, and C. P. Yuan, *New*  
 1662 *parton distributions for collider physics*, Phys. Rev. D **82** (2010) 074024, arXiv:1007.2241  
 1663 [hep-ph]. 5.1.1
- 1664 [41] T. Sjostrand, S. Mrenna, and P. Skands, *PYTHIA 6.4 physics and manual*, JHEP **05** (2006)  
 1665 026, arXiv:0603175 [hep-ph]. 5.1.1
- 1666 [42] ATLAS Collaboration, G. Aad et al., *Muon reconstruction performance of the ATLAS*  
 1667 *detector in protonproton collision data at  $\sqrt{s} = 13$  TeV*, Eur. Phys. J. **C76** (2016) no. 5, 292,  
 1668 arXiv:1603.05598 [hep-ex]. 5.2.1.1, 8
- 1669 [43] ATLAS Collaboration Collaboration, *Electron efficiency measurements with the ATLAS*  
 1670 *detector using the 2015 LHC proton-proton collision data*, Tech. Rep.  
 1671 ATLAS-CONF-2016-024, CERN, Geneva, Jun, 2016.  
 1672 <https://cds.cern.ch/record/2157687>. 5.2.1.2
- 1673 [44] M. Cacciari, G. P. Salam, G. Soyez, *The anti- $k_t$  jet clustering algorithm*, JHEP **04** (2008) 063,  
 1674 arXiv:0802.1189 [hep-ph]. 5.2.1.3, 6.4.1
- 1675 [45] ATLAS Collaboration, M. Aaboud et al., *Jet energy scale measurements and their systematic*  
 1676 *uncertainties in proton-proton collisions at  $\sqrt{s} = 13$  TeV with the ATLAS detector*, Phys.  
 1677 Rev. D **96** (2017) no. 7, 072002, arXiv:1703.09665 [hep-ex]. 5.2.1.3
- 1678 [46] *Tagging and suppression of pileup jets with the ATLAS detector*, Tech. Rep.  
 1679 ATLAS-CONF-2014-018, CERN, Geneva, May, 2014.  
 1680 <http://cds.cern.ch/record/1700870>. 5.2.1.3
- 1681 [47] D. Adams, C. Anastopoulos, A. Andreadza, M. Aoki, L. Asquith, M. Begel, F. Bernlochner,  
 1682 U. Blumenschein, A. Bocci, S. Cheatham, W. Davey, P.-A. Delsart, P.-O. DeViveiros,  
 1683 A. Dewhurst, D. Duschinger, F. Filthaut, P. Francavilla, F. Garberson, S. Head, A. Henrichs,  
 1684 A. Hoecker, M. Kagan, B. Kersevan, T. Khoo, B. Lenzi, D. Lopez Mateos, B. Malaescu,  
 1685 Z. Marshall, T. Martin, C. Meyer, A. Morley, W. Murray, M. zur Nedden, R. Nicolaidou,  
 1686 S. Pagan Griso, G. Pasztor, P. Petroff, C. Pizio, R. Polifka, X. Poveda, R. Reece, F. Ruehr,  
 1687 F. Salvatore, R. Sandstroem, T. Scanlon, D. Scheirich, S. Schramm, A. Schwartzman,  
 1688 K. Suruliz, M. Sutton, E. Thompson, M. Tripiana, A. Tuna, S. Viel, M. Vincter, I. Vivarelli,  
 1689 M. Wielers, A. Wildauer, and Z. Zinonos, *Recommendations of the Physics Objects and*  
 1690 *Analysis Harmonisation Study Groups 2014*, Tech. Rep. ATL-PHYS-INT-2014-018, CERN,  
 1691 Geneva, Jul, 2014. <https://cds.cern.ch/record/1743654>. 5.2.1.4
- 1692 [48] ATLAS Collaboration, M. Aaboud et al., *Measurement of the cross-section for producing a W*  
 1693 *boson in association with a single top quark in pp collisions at  $\sqrt{s} = 13$  TeV with ATLAS*,  
 1694 JHEP **01** (2018) 063, arXiv:1612.07231 [hep-ex]. 5.2.1.4

- 1695 [49] ATLAS Collaboration, M. Aaboud et al., *Performance of missing transverse momentum*  
 1696 *reconstruction with the ATLAS detector using proton-proton collisions at  $\sqrt{s} = 13$  TeV*, *Eur.*  
 1697 *Phys. J.* **C78** (2018) no. 11, 903, [arXiv:1802.08168](https://arxiv.org/abs/1802.08168) [hep-ex]. 5.2.2
- 1698 [50] ATLAS Collaboration, M. Aaboud et al., *Measurements of b-jet tagging efficiency with the*  
 1699 *ATLAS detector using  $t\bar{t}$  events at  $\sqrt{s} = 13$  TeV*, *JHEP* **08** (2018) 089, [arXiv:1805.01845](https://arxiv.org/abs/1805.01845)  
 1700 [hep-ex]. 5.2.2
- 1701 [51] J.-F. Arguin, J. Claude, G. Gonella, B. P. Kersevan, and K tech. rep. 5.3.3
- 1702 [52] C.-H. Kom and W. J. Stirling, *Charge asymmetry in  $W + \text{jets}$  production at the LHC*, *Eur.*  
 1703 *Phys. J.* **C69** (2010) 67–73, [arXiv:1004.3404](https://arxiv.org/abs/1004.3404) [hep-ph]. 5.4
- 1704 [53] R. Steerenberg, *LHC Report: Another run is over and LS2 has just begun...*,  
 1705 [https://home.cern/news/news/accelerators/](https://home.cern/news/news/accelerators/lhc-report-another-run-over-and-ls2-has-just-begun)  
 1706 [lhc-report-another-run-over-and-ls2-has-just-begun](https://home.cern/news/news/accelerators/lhc-report-another-run-over-and-ls2-has-just-begun), 2018. Accessed: 2018-12-14. 6
- 1707 [54] *Letter of Intent for the Phase-I Upgrade of the ATLAS Experiment*, Tech. Rep.  
 1708 CERN-LHCC-2011-012. LHCC-I-020, CERN, Geneva, Nov, 2011.  
 1709 [http://cds.cern.ch/record/1402470](https://cds.cern.ch/record/1402470). 6
- 1710 [55] G. Apollinari, I. Bjar Alonso, O. Brning, M. Lamont, and L. Rossi, *High-Luminosity Large*  
 1711 *Hadron Collider (HL-LHC): Preliminary Design Report*. CERN Yellow Reports: Monographs.  
 1712 CERN, Geneva, 2015. <https://cds.cern.ch/record/2116337>. 6
- 1713 [56] ATLAS Collaboration Collaboration, ATLAS Collaboration, *ATLAS Phase-II Upgrade*  
 1714 *Scoping Document*, Cern-lhcc-2015-020, Geneva, Sep, 2015.  
 1715 [http://cds.cern.ch/record/2055248](https://cds.cern.ch/record/2055248). 6
- 1716 [57] D. Espriu and B. Yencho, *Longitudinal WW scattering in light of the “Higgs boson”*  
 1717 *discovery*, *Phys. Rev. D* **87** (2013) 055017, [arXiv:1212.4158](https://arxiv.org/abs/1212.4158) [hep-ph]. 6, 6.1
- 1718 [58] ATLAS Collaboration Collaboration, *Prospects for the measurement of the  $W^\pm W^\pm$  scattering*  
 1719 *cross section and extraction of the longitudinal scattering component in pp collisions at the*  
 1720 *High-Luminosity LHC with the ATLAS experiment*, Tech. Rep. ATL-PHYS-PUB-2018-052,  
 1721 CERN, Geneva, Dec, 2018. [http://cds.cern.ch/record/2652447](https://cds.cern.ch/record/2652447). 6
- 1722 [59] ATLAS Collaboration Collaboration, *Studies on the impact of an extended Inner Detector*  
 1723 *tracker and a forward muon tagger on  $W^\pm W^\pm$  scattering in pp collisions at the*  
 1724 *High-Luminosity LHC with the ATLAS experiment*, Tech. Rep. ATL-PHYS-PUB-2017-023,  
 1725 CERN, Geneva, Dec, 2017. <https://cds.cern.ch/record/2298958>. 6
- 1726 [60] T. Sjöstrand, S. Ask, J. R. Christiansen, R. Corke, N. Desai, P. Ilten, S. Mrenna, S. Prestel,  
 1727 C. O. Rasmussen, and P. Z. Skands, *An Introduction to PYTHIA 8.2*, *Comput. Phys.*  
 1728 *Commun.* **191** (2015) 159–177, [arXiv:1410.3012](https://arxiv.org/abs/1410.3012) [hep-ph]. 6.2
- 1729 [61] ATLAS Collaboration Collaboration, *Expected performance for an upgraded ATLAS detector*  
 1730 *at High-Luminosity LHC*, Tech. Rep. ATL-PHYS-PUB-2016-026, CERN, Geneva, Oct, 2016.  
 1731 [http://cds.cern.ch/record/2223839](https://cds.cern.ch/record/2223839). 6.3
- 1732 [62] P. C. Bhat, H. B. Prosper, S. Sekmen, and C. Stewart, *Optimizing Event Selection with the*  
 1733 *Random Grid Search*, *Comput. Phys. Commun.* **228** (2018) 245–257, [arXiv:1706.09907](https://arxiv.org/abs/1706.09907)  
 1734 [hep-ph]. 6.5.1

- 1735 [63] G. Cowan, K. Cranmer, E. Gross, and O. Vitells, *Asymptotic formulae for likelihood-based*  
1736 *tests of new physics*, *Eur. Phys. J.* **C71** (2011) 1554, arXiv:1007.1727 [physics.data-an].  
1737 [Erratum: Eur. Phys. J.C73,2501(2013)]. **6.5.1**